UNIVERSIDADE FEDERAL DE MINAS GERAIS

Escola de Engenharia

Programa de Pós-Graduação em Engenharia Metalúrgica, Materiais e de Minas

Jéssica Dornelas Silva

DEVELOPMENT OF Ti-Ni-BASED ALLOYS FOR SOLID-STATE REFRIGERATION

Belo Horizonte

2023

Jéssica Dornelas Silva

Development of Ti-Ni-based Alloys for Solid-State Refrigeration

Tese apresentada ao Programa de Pós-Graduação em Engenharia Metalúrgica, Materiais e de Minas da Escola de Engenharia da Universidade Federal de Minas Gerais, como requisito parcial para obtenção do título de Doutor em Engenharia Metalúrgica, Materiais e de Minas.

Área de Concentração: Metalurgia Física.

Orientador: Prof. Vicente Tadeu Lopes Buono.

Coorientadores: Prof. Leandro de Arruda Santos

Prof. Dilson Silva dos Santos

Belo Horizonte

2023

Silva, Jéssica Dornelas.
S586d Development of Ti-Ni-based alloys for solid-state refrigeration [recurso eletrônico] / Jéssica Dornelas Silva. – 2023.
1 recurso online (168 f.: il., color.): pdf.

Orientador: Vicente Tadeu Lopes Buono.
Coorientadores: Leandro de Arruda Santos, Dilson Silva dos Santos.

Tese (doutorado) - Universidade Federal de Minas Gerais, Escola de Engenharia.

Anexos: f. 162-168.

Bibliografia: f. 142-161.
Exigências do sistema: Adobe Acrobat Reader.

1. Engenharia metalúrgica - Teses. 2. Metalurgia física - Teses. 3. Ligas - Teses. 4. Efeito da memória de forma - Teses. 5. Refrigeradores - Teses. I. Buono, Vicente Tadeu Lopes. II. Santos, Leandro de Arruda. III. Santos, Dilson Silva dos. IV. Universidade Federal de Minas Gerais. Escola de Engenharia.
V. Título.

CDU: 669(043)

Ficha catalográfica elaborada pela Bibliotecária Roseli Alves de Oliveira CRB/6 2121
Biblioteca Prof. Mário Werneck, Escola de Engenharia da UFMG

UNIVERSIDADE FEDERAL DE MINAS GERAIS
ESCOLA DE ENGENHARIA
Programa de Pós-Graduação em Engenharia Metalúrgica, Materiais e de Minas

A tese intitulada **"Desenvolvimento de Ligas Baseadas em Ti-Ni para Aplicações como Refrigeradores do Estado Sólido"**, área de concentração: Metalurgia Física, apresentada pela candidata **Jéssica Dornelas Silva**, para obtenção do grau de Doutora em Engenharia Metalúrgica, Materiais e de Minas, foi aprovada pela comissão examinadora constituída pelos seguintes membros:

Dr. Vicente Tadeu Lopes Buono
Orientador (UFMG)

Dr. Leandro de Arruda Santos
Coorientador (UFMG)

Dr. Dilson Silva dos Santos
(UFRJ)

Dra. Berenice Mendonça Gonzalez
(UFMG)

Dr. Dagoberto Brandão Santos
(UFMG)

Dr. Carlos José de Araújo
(UFCG)

Dr. Walter José Botta Filho
(UFSCar)

Coordenador do Programa de Pós-Graduação em Engenharia Metalúrgica, Materiais e de Minas/UFMG

Belo Horizonte, 16 de junho de 2023

AGRADECIMENTOS

Aos meus pais, Neide e João Pedro, que me deram meu primeiro microscópio (da Barbie) e, desde sempre, me apoiam e me proporcionam todas as oportunidades no alcance deles. Ao meu irmão, Pedro, meu companheiro mais fiel, por todas as vezes que ele me escutou, me acolheu e me confortou.

Ao Vicente, por me permitir trilhar meu próprio caminho, me guiando em cada passo. Por me permitir definir meu projeto de doutorado e abraçar ele junto comigo. Por sofrer comigo e comemorar cada acerto. Por todas as reuniões noturnas e em finais de semana. Por ser uma das melhores pessoas, orientador e pesquisador que eu tive o privilégio de conhecer. Por ser o meu maior aliado nessa jornada.

Ao Leandro, por todas as vezes que ele me acalmou, me centrou e me protegeu (dos outros e de mim mesma). Por ser tão inabalável e assertivo. Por tomar decisões que eu não queria tomar, tomar conta de embates que eu tinha medo de ter e ver soluções quando eu não consegui ver.

Ao Dilson, por não medir esforços para me ajudar, sempre acreditando que vai dar tudo certo. Pelos questionamentos, ensinamentos e toda a paciência. Por notar quando eu me abalo e não me deixar cair. Por sempre tentar me elevar e por acreditar tanto em mim. Por ter segurado minha mão e ter me trazido novas oportunidades.

À professora Berenice, por ser sempre tão acessível e carinhosa comigo. Por toda clareza nas explicações. Por ter me ensinado uma nova forma de estudar quando eu achava que já sabia qual era o jeito certo. Por ser uma inspiração para mim. Ao professor Dagoberto, por sempre me acudir com meus "feijõezinhos". Pela presença e apoio constantes no laboratório. Aos professores Carlos José e Walter Botta, por toda disponibilidade ao aceitar compor a banca e contribuições para este trabalho. Aos professores Pedro, Witor e Eric, por disponibilizar seus laboratórios e equipamentos. Mais do que isso, por tantas conversas de corredor e pelas contribuições que talvez eles nem saibam que deram.

À Natália, Pedro, Suzanny e Paula, pelos conselhos, pela parceria dentro e fora do laboratório, por ouvirem meus desabafos e por me entenderem tão bem. À Gisele, Carol e Mariana, por me acompanharem, confiarem em mim e aguentarem todos os meus humores e demandas. Aos companheiros da UFMG, Guilherme, Carol, Samuel, Maria, Davi, Rafael e Anderson, por compartilhar comigo os desafios de tempos pandêmicos, por toda ajuda para resolver problemas

e por tornarem meus dias mais leves. À Patrícia, pela maestria em conduzir análises (e em me acalmar). Aos colegas da PROPMEC/UFRJ, Sara, Rafael, Rodrigo, Mariana A., Durval, Débora, Francisco, Roni, Léozinho e Fábio, pelo acolhimento.

À Simone e Claudino, à minha tia Olga, ao Rogério e à Nara, ao meu tio Divino, por sempre acreditarem em mim. À Luiza, Júlia, Ricardo, Glenda e Camila, por serem minha família estendida. À Ana, Amanda e Madruga, por se manterem tão perto mesmo a quilômetros de distância. À Isa e Bia, por sempre torcerem por mim. Ao Felipe e ao Túlio, por todo cuidado e carinho. À Jaqueline, Glaucia, Larissa, Gabriela, Sílvia, Bárbara, Luísa, Jordana, Túlio, Débora e Mariana, por sempre me acompanharem de perto. Ao Ítalo e à Simone, por não saírem do meu lado. À Bete, Gil, William, Tágila, Humberto e Matheus, por todos os anos em que eles foram uma parte tão importante da minha vida. À Bianca, Manu, Gui, Isabella e Lis, por alegrarem meus dias, mesmo que em vídeos e fotos. À Flávia, por me ensinar a ter momentos de paz no meio do caos.

À CAPES, CNPq e FAPEMIG, pelo apoio financeiro. À UFMG e ao PPGEM por todo suporte e infraestrutura.

RESUMO

Ligas com memória de forma são materiais atrativos no desenvolvimento de elementos elastocalóricos como alternativa de refrigeração sustentável. Graças à ocorrência de uma transformação martensítica induzida, efeitos calóricos significativos podem ser obtidos pela aplicação de carregamento mecânico nestas ligas no estado superelástico. Entretanto, o uso das tradicionais ligas binárias TiNi tem sua aplicação limitada por uma resistência à fadiga insatisfatória. Uma alternativa para obter ligas potenciais consiste no estudo de ligas de baixa histerese mecânica, uma vez que essa propriedade pode ser relacionada a um baixo acúmulo de danos durante ciclos superelásticos. A adição de certas quantidades de Cu no lugar de Ni resulta em ligas ternárias amplamente conhecidas por apresentar baixa histerese mecânica. Um quarto elemento de liga pode ser adicionado para otimizar as propriedades dessas ligas. Neste contexto, este estudo tem como objetivo desenvolver e caracterizar ligas no sistema Ti-Ni-Cu-Nb, visando a obtenção de uma liga promissora para aplicação como material elastocalórico. Depois de um estudo termodinâmico baseado no método de cálculo de diagramas de fases, ligas $Ti_{52-x}Ni_{38}Cu_{10}Nb_{x,\ x = 4, 6, 8 \text{ e } 10\%at}$ foram selecionadas para obtenção de frações significativas da fase TiNi com a precipitação de β-Nb. Estas ligas foram sintetizadas e o efeito do Nb na estabilidade de fases e sequência de solidificação foi discutido. As microestruturas como-fundidas consistem em uma matriz de TiNi, eutético TiNi/β-Nb e Ti_2Ni. A formação de Ti_2Ni foi associada ao processo solidificação devido ao enriquecimento de Ti no líquido enquanto a do eutético foi atribuída ao enriquecimento de Nb e empobrecimento de Ni. A evolução microestrutural durante diferentes rotas de processamento foi avaliada e a estabilidade das fases metaestáveis foi observada. Limitações durante laminação a quente foram atribuídas ao coalescimento e fusão parcial do Ti_2Ni. Como alternativa para se obter uma microestrutura homogênea e refinada, o procedimento de re-fusão seguida de solidificação por sucção à vácuo foi acessada. Nesta condição, uma entalpia de transformação relevante e a convergência de ciclos superelásticos foram obtidas. A liga Ti-Ni-Cu-Nb produzida se mostrou tratável termicamente após processamento termomecânico adequado, possibilitando o ajuste das propriedades funcionais.

PALAVRAS-CHAVE: Ligas com memória de forma; superelasticidade; desenvolvimento de liga; refrigeração no estado sólido.

ABSTRACT

Shape memory alloys are attractive materials in the development of elastocaloric components for sustainable solid-state refrigeration. Due to the occurrence of an induced martensitic transformation, significant caloric effects can be achieved simply by mechanically loading and unloading these alloys in the superelastic state. However, the use of traditional binary TiNi alloys is limited by unsatisfactory functional and structural fatigue resistance. An alternative to achieve potential candidates consists of exploring low mechanical-hysteresis alloys, since this property can be related to low damage accumulation during cycling. The addition of certain amounts of Cu in substitution for Ni is well-known to lower the hysteresis of binary TiNi. The optimization of Ti-Ni-Cu ternary alloys for elastocaloric means, in its turn, can be accomplished by adding a fourth component. In this context, this study aims to develop and evaluate alloys in the Ti-Ni-Cu-Nb system for use as elastocaloric materials for solid-state refrigeration. After thermodynamic evaluation using CALPHAD, $Ti_{52-x}Ni_{38}Cu_{10}Nb_x$ alloys were selected with varying Nb contents of 4, 6, 8 and 10 at% for obtaining significant fractions of the TiNi phase and β-Nb precipitation. These alloys were synthesized and the effect of Nb in the phase stability and solidification sequence was examined. The microstructure consisted of a TiNi matrix phase, β-Nb/TiNi eutectic and Ti_2Ni precipitates. The formation of Ti-rich particles was discussed to occur during solidification due to a Ti enrichment in the liquid while the eutectic constituent presence was attributed to Nb enrichment and Ni depletion. The microstructural evolution at different rolling procedures was assessed, and a high stability of the metastable phases was observed. Hot rolling limitations were related to partial melting and coalescence of Ti_2Ni phase. As an alternative processing technique, re-melting of as-cast alloys followed by fast-cooling suction-cast process was tested, resulting in a refined phase distribution and uniform reversible martensitic transformation. In this condition, relevant transformation enthalpy and early convergence of superelastic cycles were achieved. The suction-cast Ti-Ni-Cu-Nb alloy is heat-treatable after proper thermomechanical processing, making room for tailoring functional properties.

KEYWORDS: Shape memory alloys; superelasticity; alloy development; solid-state refrigeration.

LIST OF FIGURES

LIST OF TABLES

LIST OF SYMBOLS AND ABREVIATIONS

AC – As-cast

BSE – Backscattered Electron

BSEI – Backscattered Electron Image

CALPHAD - Calculation of Phase Diagrams

CC – Conventional casting

CFCs – Chlorofluorocarbons

COP – Coefficient of Performance

CR – Cold-rolled

DSC – Differential Scanning Calorimetry

EDS – Energy-Dispersive X-ray Spectroscopy

GWP – Global Warming Potential

HFCs – Hydrofluorocarbons

HR – Hot-rolled

HVAC – Heating, Ventilation, and Air-Conditioning

MT – Martensitic Transformation

SC – Suction casting

SE – Superelasticity

SEM – Scanning Electron Microscopy

SIM – Stress-Induced Martensite

SMA – Shape Memory Alloy

SME – Shape Memory Effect

XRD – X-ray Diffraction

TABLE OF CONTENTS

1. INTRODUCTION

The development of alternative refrigeration methods has received attention in the past few years as an effort to minimize environmental impacts related to the release of chlorofluorocarbons (CFCs) and hydrofluorocarbons (HFCs) gases associated with traditional vapor-compression systems. Among different alternatives, solid-state refrigeration methods are based on the use of a solid material as a refrigerant, coupled with an environmentally harmless fluid for heat-transferring.

For that means, the refrigerant material must exhibit a large caloric effect in the solid-state, observed as it releases or absorbs heat when subjected to an external field. This is an intrinsic property related to a structural transition induced by appropriate stimuli, which can be magnetic, electric, hydrostatic, or elastic. The magneto-, electro-, baro- and elastocaloric effects are defined according to the respective applied external field to achieve the desired heat exchange. In this context, the elastocaloric effect can be defined as an adiabatic temperature change or an isothermal entropy change that occurs when the material is loaded or unloaded. This effect is intimately related to the enthalpy variation during a stress-induced transformation.

Due to the easy control and the large caloric effects that can be achieved, the elastocaloric-based refrigeration method has been identified by the U.S. Energy Department as the alternative with the highest potential amongst the different proposed cooling technologies. Besides the high efficiency and energy-saving potential, this method could also be used in applications that are not suppressed by the current vapor-compression technology, such as microsystems, high voltage circuits, and cooling of human tissues during a clinical procedure. However, despite the relevant studies and current development of devices design, an ideal material for commercial application has not yet been achieved.

Shape memory alloys (SMAs) are materials that undergo a thermoelastic martensitic transformation (MT), characterized by a reversive behavior between a high-temperature austenitic phase and a low-temperature martensitic phase. Because the direct martensitic transformation is exothermic and the reverse transformation is endothermic, these alloys have a great potential to be used for caloric means and have been vastly explored in the last few years. As elastocaloric materials, they should be assessed in the superelastic (SE) state. In this case, they are loaded in the austenitic phase and a stress-induced martensitic transformation

(SIMT) takes place, releasing heat. During unloading, the occurrence of the reverse transformation to austenite is accompanied by shape recovery and heat absorption.

To be used as a solid-state refrigerant, the SMA should present high MT's latent heat, leading to a large caloric effect. Furthermore, high material efficiency, measured by the coefficient of performance (COP), is required. This parameter is obtained as the quotient of the heat absorbed during the reverse MT over the work required to induce it. Because these components will be subjected to continuous loading and unloading, good structural and functional fatigue resistances are necessary.

Despite their large caloric effects, the vastly explored binary TiNi alloys present a relatively low COP and unsatisfactory fatigue life. These drawbacks are due to the high transformation work and the cyclic damage accumulation, both associated with the high mechanical hysteresis during SE cycle. As follows, an alternative lies in the development and use of low hysteresis SMAs. The addition of some amounts of Cu in substitution for Ni in binary NiTi is well-known to result in a significant decrease in the transformation hysteresis. As a result, studies have shown that, indeed, great thermal stability and fatigue resistance can be obtained in TiNiCu ternary alloys and in TiNiCu-based quaternary alloys.

In this context, TiNiCuCo and TiNiCuV alloys have been identified as good candidates for elastocaloric use, with good thermal, functional, and structural stability, and, hence, potentially high fatigue resistance. More recently, the addition of Nb has been noted to significantly increase TiNiCu alloy's thermal stability. However, this quaternary system has not been vastly explored. Considering the similarities of Co, V, and Nb in alloying additions as well as the relative lower cost and toxicity of Nb, this work will consist of developing, synthesizing, and characterizing SMAs in the Ti-Ni-Cu-Nb system. This is a promising system for obtaining good transformation stability while attaining relevant transformation enthalpy. The aim is to explore the phase stability, thermomechanical processing challenges and prospects of the developed alloys.

1.1. Introdução

O desenvolvimento de métodos alternativos de refrigeração tem recebido atenção nos últimos anos em uma busca pela minimização dos impactos ambientais relacionados à liberação de gases HFCs e CFCs associados aos sistemas de refrigeração tradicionais. Dentre os diversos métodos alternativos, refrigeradores no estado sólido baseiam-se no uso de um material sólido como meio refrigerante acoplado a um fluído não-nocivo ao meio ambiente para transferência de calor.

Para isso, o material utilizado como meio refrigerante deve apresentar um efeito calórico grande no estado sólido, observado como uma liberação ou absorção de calor resultante da aplicação de um campo externo. Trata-se de uma propriedade intrínseca do material relacionada a transformações estruturais induzidas pela aplicação de um estímulo adequado, que pode ser um campo magnético, elétrico, hidrostático ou elástico. Assim, os efeitos magnetocalórico, eletrocalórico, barocalórico e elastocalórico são definidos, respectivamente, de acordo com o campo externo aplicado. O efeito elastocalórico é visto como uma mudança adiabática da temperatura, ou uma mudança isotérmica da entropia, que ocorre durante a aplicação ou retirada de um carregamento mecânico do material, estando intimamente ligado à variação de entalpia durante uma transformação de fases induzida por tensão.

Graças à facilidade de controle e aos grandes efeitos calóricos que podem ser obtidos, o efeito elastocalórico foi identificado como a tecnologia alternativa de refrigeração de maior potencial em relatório do Departamento de Energia dos Estados Unidos. Além da alta eficiência e economia de energia potenciais, refrigeradores no estado sólido baseados em materiais elastocalóricos têm ainda a possibilidade de serem utilizados em aplicações que não são supridas pelos sistemas tradicionais de compressão de gases. Como exemplos destas aplicações, pode-se citar o uso em microssistemas, circuitos de alta potência e resfriamento de tecidos humanos durante um procedimento cirúrgico. Entretanto, apesar de resultados iniciais promissores e do avanço no design de dispositivos, um material ideal para esta aplicação ainda não foi encontrado.

Ligas com memória de forma (LMFs) são materiais que passam por uma transformação martensítica (TM) termoelástica, caracterizada por sua natureza reversível, que ocorre de uma fase austenítica de alta temperatura para uma fase martensítica de baixa temperatura. Uma vez

que a transformação é exotérmica no sentido direto e endotérmica no sentido reverso, essas ligas podem ser utilizadas por seus efeitos calóricos e vêm sendo amplamente exploradas para tal nos últimos anos. Como materiais elastocalóricos, elas devem ser empregadas em seu estado superelástico (SE). Nesse caso, o carregamento é realizado na fase austenítica e é está associado à formação de martensita induzida por tensão (MIT), resultando na liberação de calor. No descarregamento, a transformação reversa para austenita ocorre acompanhada tanto da recuperação da forma inicial quanto de uma absorção de calor.

Para ser utilizada como um meio refrigerante, a LMF deve apresentar uma grande variação de entalpia, e, portanto, um efeito calórico grande, durante a TM. Além disso, uma alta eficiência do material, medida pelo coeficiente de performance (COP), é necessária. Esse parâmetro é obtido como o quociente entre o calor absorvido durante a transformação reversa, pelo trabalho requerido para induzir a TM. Adicionalmente, uma vez que estes elementos serão submetidos a ciclos contínuos de carregamento e descarregamento, boas resistências à fadiga estrutural e funcional são essenciais.

Apesar de apresentar efeitos calóricos muito grandes, ligas do sistema NiTi apresentam um COP relativamente baixo e uma vida em fadiga insatisfatória. Essas limitações são devidas ao alto trabalho requerido e ao acúmulo de danos durante a ciclagem mecânica, ambos relacionadas à sua alta histerese mecânica característica. Com isso, uma alternativa a ser explorada se encontra no desenvolvimento de LMFs de baixa histerese. Sabe-se que a adição de Cu em substituição ao Ni em ligas NiTi binárias resulta em uma diminuição significativa da histerese mecânica de transformação. Como resultado, estudos mostram que, de fato, ótima estabilidade térmica e resistência à fadiga podem ser obtidas em ligas TiNiCu bem como em ligas quaternárias TiNiCu-X.

Estudos anteriores identificaram ligas TiNiCuCo e TiNiCuV como boas candidatas para uso como materiais elastocalóricos de boa estabilidade térmica, funcional e estrutural e, consequentemente, com uma boa resistência à fadiga potencial. Em estudo mais recente, foi observado que a adição de Nb aumenta significativamente a estabilidade térmica de uma liga TiNiCu. Entretanto, não existem maiores estudos sobre esse sistema. Neste contexto, considerando as similaridades nas adições de liga dos elementos Co, V e Nb bem como o menor custo e toxicidade do Nb, o presente trabalho consiste no desenvolvimento, síntese e caracterização de LMFs do sistema Ti-Ni-Cu-Nb. Trata-se de um sistema promissor para se

atingir ligas de alta estabilidade de TM simultaneamente a obtenção de calores latentes relevantes. O objetivo é explorar a estabilidade de fases, desafios no processamento termomecânico e as perspectivas de uso das ligas desenvolvidas.

1.2. Objective

1.2.1. Main objective

The main goal of this study is to develop and explore alloys in the Ti-Ni-Cu-Nb system with promising properties for elastocaloric use in solid-state refrigeration.

1.2.2. Specific objectives

- Perform a thermodynamic study of the Ti-Ni-Cu-Nb system through the CALPHAD method.
- Design candidate alloys based on thermodynamic calculations and literature data.
- Cast the selected alloys and investigate the effect of Nb on the phase stability and solidification sequence.
- Evaluate the effect of thermomechanical processing on the microstructure and heterogeneity of the cast-alloys.
- Optimize the processing route to achieve refined and uniform microstructure.
- Evaluate the use of heat-treatments to tailor the martensitic transformation temperature and enthalpy.

1.3. Thesis Structure

The present thesis is divided into eight chapters, as disposed in Figure 1-1. Chapter 1 provides a contextualization of the studied topic, as well as a presentation of the thesis' goals and framework. Chapter 2 discloses relevant theoretical background, exploring basic concepts and definitions of reversible martensitic transformation, shape memory effect and superelasticity, and current research on the development and challenges for the use of shape memory materials as elastocaloric components. Methodology, results and discussion are presented in Chapters 3 – 8, arranged by the specific goals. In chapter 3, the Ti-Ni-Cu-Nb was explored through computational thermodynamics calculations. Moreover, previously published results on this system were gathered, summarized and extrapolated to select promising compositions for further appraisal. Chemical compositions were designed aiming to obtain a majorly TiNi structure, attaining relevant shape memory effect, with β-Nb precipitates, favoring cold-working processing and the possibility to tailor the reversible martensitic transformation. The selected alloys were synthesized and the effect of Nb on the as-cast microstructure and solidification sequence were explored, respectively, in Chapters 4 and 5. As-cast microstructures consisted of a TiNi matrix, β-Nb/TiNi eutectic, and Ti_2Ni particles. The Nb content of the alloy, and its enrichment in the liquid during solidification, affects the amount of the eutectic and the morphology of the Ti_2Ni phase. Increasing Nb content was shown to inhibit the formation of Ti_2Ni and favor that of β-Ti. Thermomechanical processing was evaluated, addressing some limitations and challenges related to second-phase coalescence and partial melting, in Chapter 6. Alternatively, re-melting followed by fast-cooling suction-cast process was used to optimize the alloy's microstructure in Chapter 7, and a refined microstructure was achieved. The suction-cast alloy was submitted to thermomechanical process, and the different final heat-treatments were used to tailor the martensitic transformation temperatures and enthalpy, obtaining an increased latent heat and Af close to room temperature, in Chapter 8. The final chapter, Chapter 9, consists of a summary of the results and conclusions obtained in the present thesis, the contributions and relevance of the achieved results, and suggestions for future studies. The references used throughout the text can be found in Chapter 10.

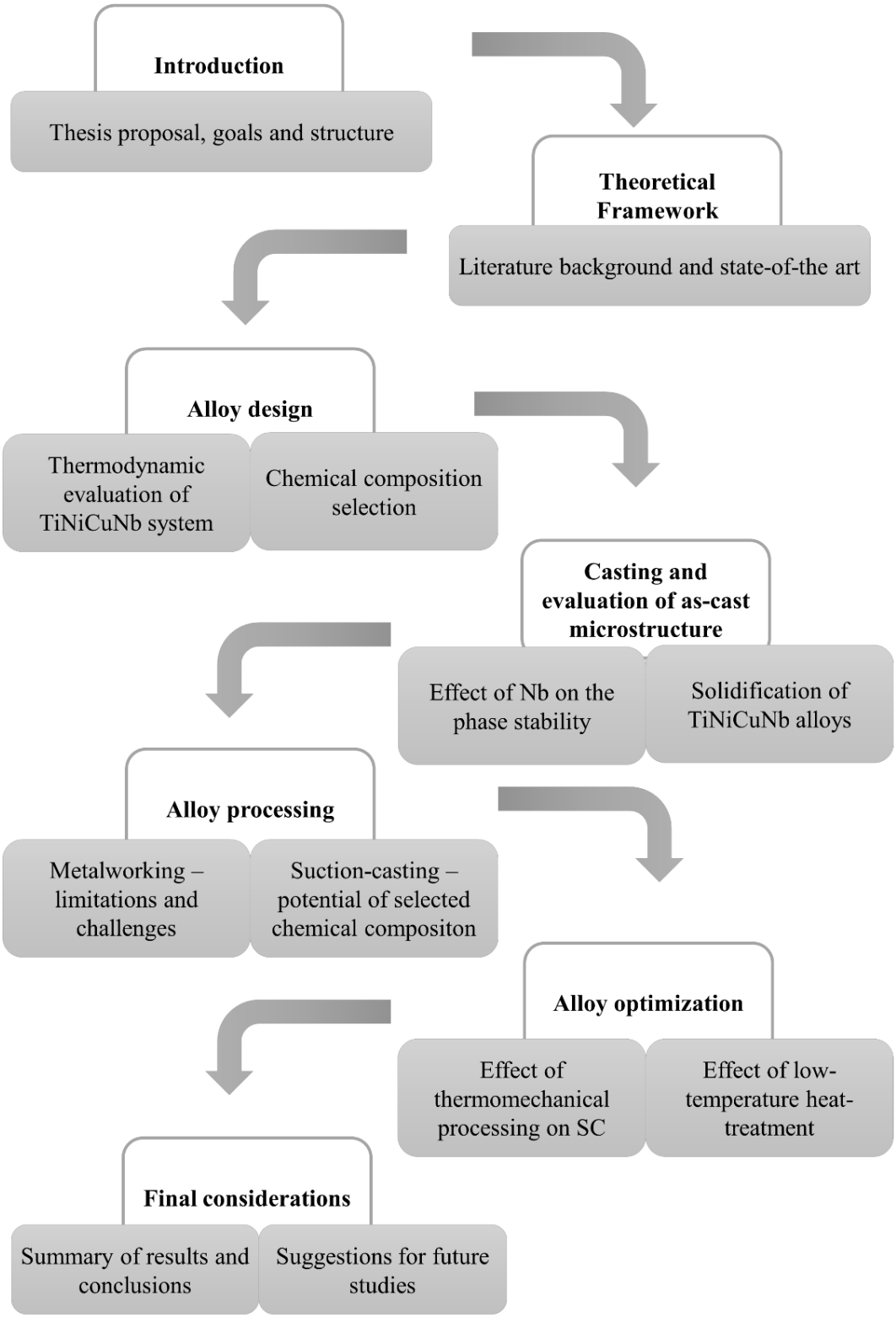

Figure 1-1 – Thesis structure

2. THEORETICAL FRAMEWORK

2.1. Background

2.1.1. Martensitic transformation

A martensitic transformation (MT) is a first order, displacive, and diffusionless solid-state phase transformation that has been observed in metallic and non-metallic crystals, minerals, and compounds. While diffusional phase transformations are related to atom-by-atom motion through interfaces, in MTs, atoms move in an orderly fashion by a shear-like mechanism over distances smaller than the interatomic spacing. This easy growth mechanism is illustrated in Figure 2-1. It results in a rapid change of crystal structure from a high-temperature parent phase, known as austenite, to a low-temperature and low-symmetry phase with the same chemical composition, known as martensite (1,2).

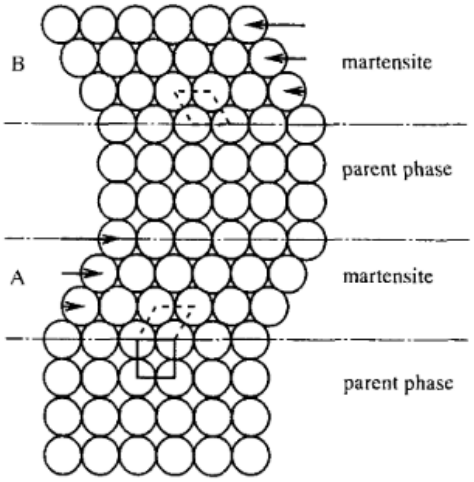

Figure 2-1 - A scheme of the martensitic transformation (1)

The forward transformation occurs when the component's temperature is decreased to the Ms temperature and its structure becomes completely martensitic when the temperature reaches the finishing transformation temperature, Mf. If cooling is interrupted, and temperature maintained between Ms and Mf, the transformation will cease, characterizing an athermal transformation (1).

During the MT, the development of transformation strains in a coherent crystal result in internal stresses and elastic distortions. For that reason, martensitic plates are thermally formed in a self-accommodating manner, presenting a variety of orientations. Each orientation corresponds to a martensite's *variant*, as illustrated in Figure 2-2. Within the parent and product phases, the strains can be accommodated either by twinning or by dislocation slip. The interaction and competition between these mechanisms of relaxation determine the features of the MT as well as the properties of the resultant martensite (3,4).

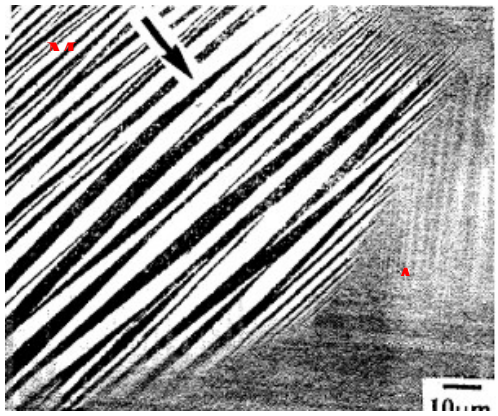

Figure 2-2 - Martensite variants (M) formed in austenitic grains (A) (1)

As strain phase transformations in which the state of the phases is completely determined by the strains of the lattice, MTs are strongly affected by the application of external loading. Because applied stresses have contributions to the free energies of parent and martensitic phases, loading affects the transformation temperatures and, hence, the interval of existence of these phases. Additionally, the MT itself and twinning in martensite act as deformation modes (3–5).

When heating is promoted in the martensitic phase, a *reverse transformation* to austenite occurs. This transformation begins at the austenitic start transformation temperature, As, and comes to an end at the austenitic transformation finishing temperature, Af. Therefore, a *thermal hysteresis* can be observed, and it is frequently given by the differences |Ms - Af| and |As – Mf|, as illustrated in Figure 2-3 (1,6).

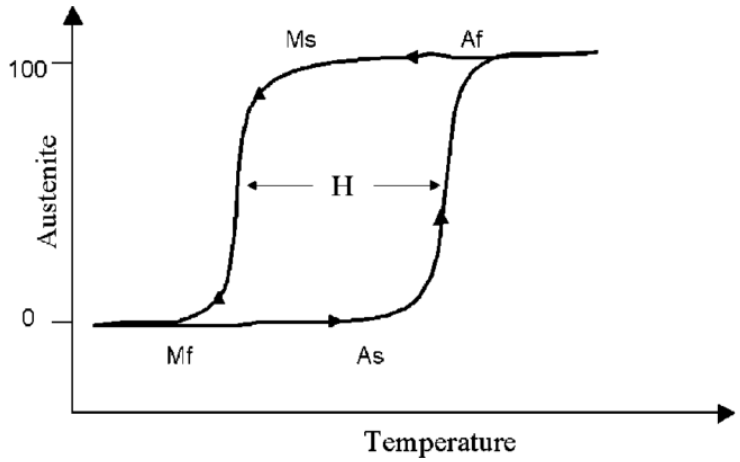

Figure 2-3 - Fraction of austenite as a function of temperature, highlighting the martensitic transformation's hysteresis (7)

The transformation temperatures differ from the temperature T_0 in which austenite and martensite present the same free energy, and, hence, are in thermodynamic equilibrium. The amount of undercooling/superheating required, respectively at the forward and reverse MT, and the occurrence of the transformation's hysteresis are related to non-chemical energy terms involved in the MT. These are the frictional work during interfacial motion on the network's shearing and the stored plastic energy. In this manner, the transformation hysteresis and the undercooling/superheating can be reduced by lowering the number of barriers to interfacial motion and increasing the compatibility of parent and product phases (5).

Certain alloys undergo a MT with a rather low thermal hysteresis. Additionally, the presence of high mobility interfaces and a predominantly elastic accommodation of the martensitic variants characterize a *thermoelastic martensitic transformation*. In these cases, where a thermoelastic equilibrium is reached and the chemical and non-chemical forces are balanced, the MT occurs in a *reversible* manner through the movement of interfaces during cooling and heating (8,9).

The occurrence of a reversible MT, which is observed in certain alloys such as Ni-Ti, Cu-Al-Zn, and Fe-Mn-Si, is responsible for the manifestation of two functional effects: the *shape memory effect* and the *superelasticity*. The characteristics of these functional properties are

determined by the features of the MT whereas the temperature ranges in which each effect will be observed is defined by the transformation's temperature (1,10).

2.1.2. Shape memory effect

The shape memory effect (SME) is defined as the ability to recover from an apparent permanent deformation by heating the component's temperature to above Af (1,11). A scheme of the development of the shape memory effect in a single-crystal is presented in Figure 2-4, and an example of a corresponding stress-strain curve is presented in Figure 2-5. During the processing of the single-crystal, cooling from an austenitic structure (Figure 2-4-a) to a temperature below Mf will result in the *thermal martensite*, with a certain variant distribution (Figure 2-4-b). This martensitic state will constitute the initial state of loading in Figure 4.5.

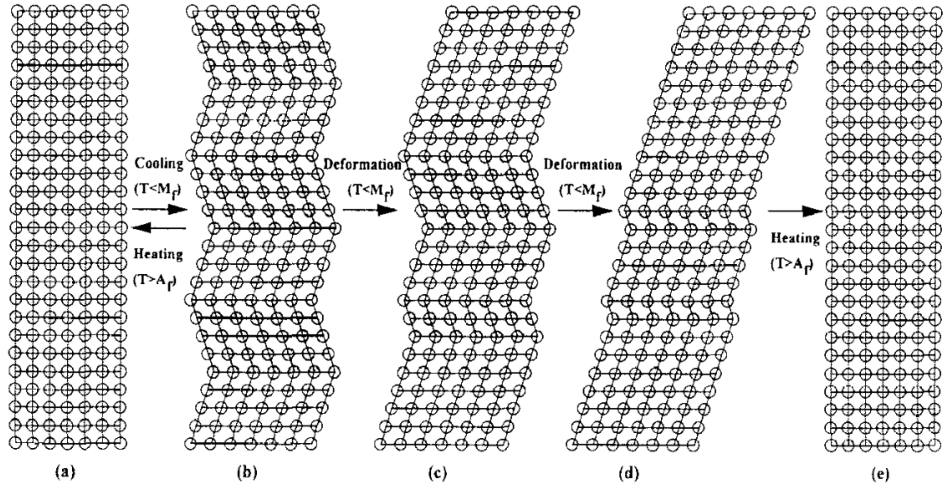

Figure 2-4 - Mechanism of shape memory effect (1)

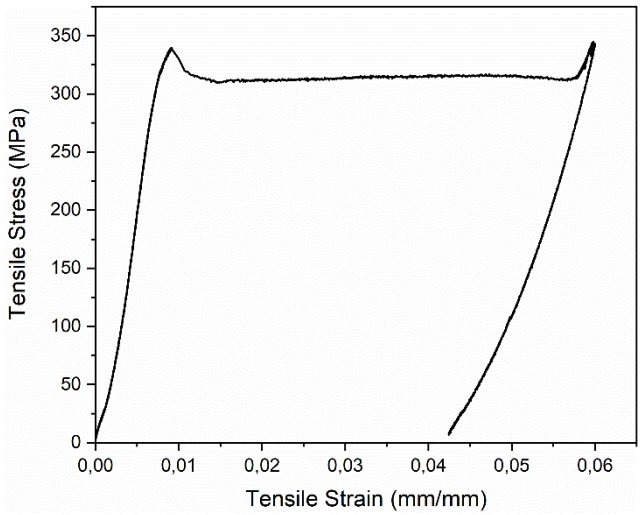

Figure 2-5 - Stress-strain curve corresponding to the shape memory effect (T<As) (12)

After the elastic regime, the deformation in the martensitic phase will be produced by a mechanism of variant reorientation, as presented in Figure 2-4-c and d. This state of loading corresponds to a stress plateau on the stress-strain curve, Figure 2-5. The variants that have their shearing components aligned to the applied stress tend to grow while the ones that are not favorable oriented tend to narrow down. This induces a preferential martensitic orientation, and the martensite becomes a *detwinned martensite* (1,10).

When loading is interrupted, the deformation is maintained, occurring only elastic recovery, which corresponds to the end of the loading/unloading stress-strain curve. During heating, the formation of austenite (Figure 4.4-e) through the reverse transformation is followed by a shape recovery thanks to its crystallographic reversibility. When the component is cooled, the thermal martensite will be formed again with various orientations, resuming the initial state (13).

In this manner, the SME is observed when the shape memory alloy is deformed in the martensitic phase by a mechanism of variant reorientation. The shape recovery is promoted by heating the unloaded component by means of the reverse transformation to austenite (1).

2.1.3. Superelasticity

When these same alloys are deformed in the austenitic phase, large amounts of non-linear deformation can be recovered during unloading. In these conditions, it is said that the alloy present superelasticity (SE), a particular case of the shape memory effect (1). In this case, the

application of stresses in determined critical values (σ^{Ms}) induces the formation of stress-induced martensite (SIM) by a network shearing mechanism. Associated with the stress-induced transformation, a macroscopic deformation is produced. By withdrawing the stresses, the martensite becomes unstable, transforming into austenite and recovering the initial shape. The result of these induced transformations is that the material can recover its shape from deformations of near 10%, simply by unloading it (10).

In the stress-strain curve of a superelastic cycle, illustrated in Figure 2-6, the stress-induced phase transformation (A → M) leads to the appearance of a stress plateau after the elastic deformation of austenite. During unloading, the reverse transformation (M → A) occurs in a stress plateau at lower stresses, and a mechanical hysteresis can be observed (1).

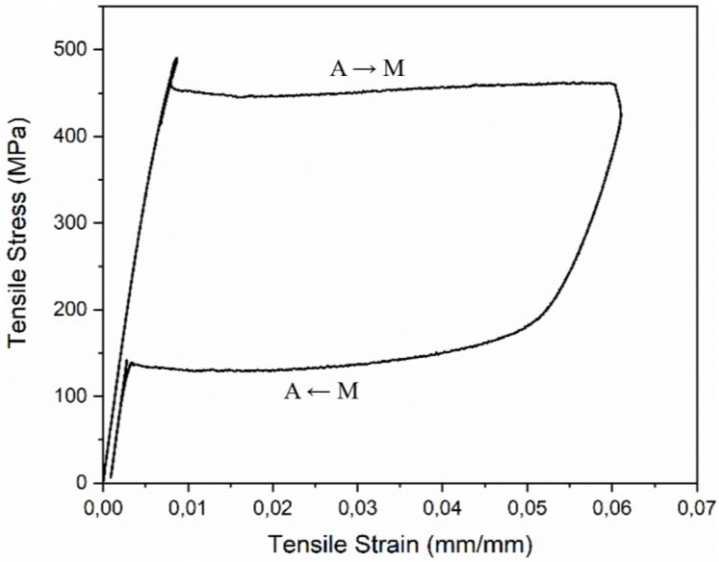

Figure 2-6 – Stress-strain curve of a shape memory alloy in the superelastic state (T>Af)

SE is only observed in temperatures above Af and below a critical temperature Md. Since increasing temperature favors the high-temperature austenitic phase, the stress required to induce martensite increases accordingly with increasing temperature. In temperatures above Md, the driving force for the induction of martensite is so high that the austenite plastically deforms before reaching σ^{Ms}. On the other hand, in temperatures lower than As, the induced

martensite will still be stable after unloading and no shape recovery will occur by withdrawing the applied stress (1).

2.1.4. Shape memory alloys in different application temperatures

The stress-strain behavior during loading/unloading of SMAs in different temperatures is illustrated in Figure 2-7. In (a), the temperature is inferior to As and the martensitic structure is maintained during unloading. In this case, the shape recovery can only be accomplished by heating, and the SME is observed. In (b), the temperature is superior to Af and a superelastic behavior with a complete shape recovery occurs. The increase in the test temperature in (c) and (d) leads to upward displacement of the superelastic curve, resultant from the higher σ^{Ms} required (1).

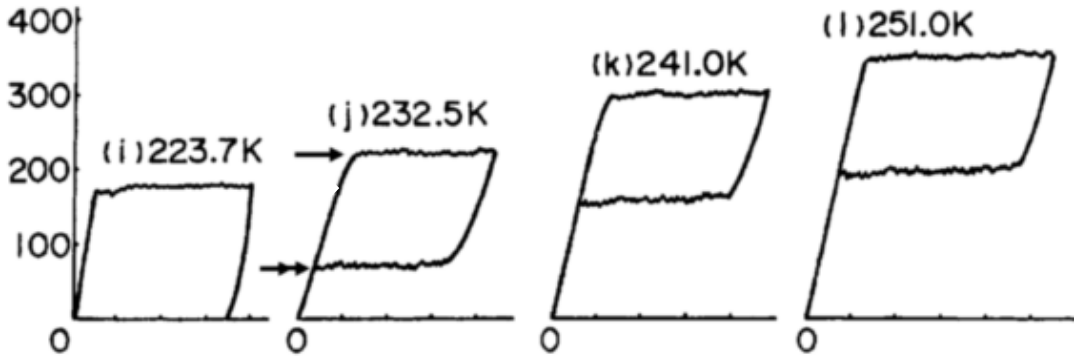

Figure 2-7 – Example of the behavior of a shape memory NiTi alloy in different loading temperatures (1)

Thus, an alloy that presents a thermoelastic MT presents both the SME and SE, depending on the loading temperature. The diagram in Figure 2-8 is a schematic representation of the regions in which each of these effects can be observed in the stress-strain range: in temperatures lower than As, the alloy will present the SME and in temperatures above Af, the alloy will present SE. In temperatures between As e Af, both SME and SE are observed (10).

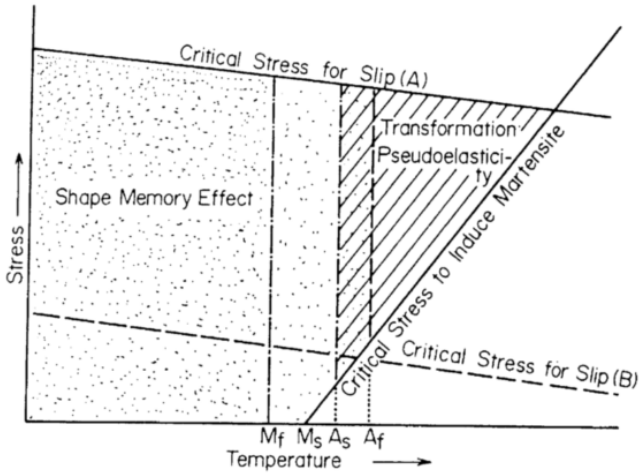

Figure 2-8 – Schematic representation of SME and SE in stress vs temperature range (10)

As previously pointed out, a significant increase in the critical stress for martensitic phase transformation induction σ^{Ms} (*Critical stress to induce martensite*) with increasing temperatures can be observed. In contrast, the yield strength slightly decreases with increasing temperature. The occurrence of plastic deformation in stresses above the yield strength hinders the SME and the SE. In general, the yield strength in alloys with functional behavior should be high, like observed in the *Critical stress for slip – A*. In alloys with low yield strength, like observed in *Critical stress for slip – B*, the presence of plastic deformation during the forward and reverse MT results in the presence of residual strains (10).

2.2. Solid-State Refrigeration

2.2.1. Current cooling technology

Heating, ventilation and air conditioning (HVAC) equipment hold responsibility for significant amounts of society's energetic demands. In 2013, HVAC accounted for 38% of the residential and commercial buildings' primary energy consumption in the United States of America and nearly 20% of the world's energy demands in 2015 (14–16). With the population growth and the increasing desire for building services and higher comfort levels, recent reports by the International Energy Agency show that the energy use for space cooling is expanding rapidly both in absolute terms and as a share of overall energy use in buildings (17). It has been too

pointed out that the scope for energy efficiency improvements remains large for heating and air conditioning (18).

Currently, the major cooling technology used is vapor-compression systems, which are based on closed-loop thermodynamic cooling cycles where heat is transported by compressing, condensing, expanding, and evaporating a working fluid. This mechanism relies on the basic physical principle that when a liquid evaporates, it absorbs heat and when it condenses, it releases heat. Even though the use of these systems is now a mature technology, it is still characterized by high environmental impacts and rather low energy efficiency (14,17,19).

A major cause of the environmental impacts is related to releases of the working fluids used as refrigerants into the atmosphere. These are mainly synthetic hydrofluorocarbons (HFCs) and chlorofluorocarbons (CFCs) designed specifically for HVAC applications. Despite being improved over the past years, they are still detrimental to climate change: CFCs enhance the degradation of the ozone layer, and HFCs are greenhouse gases, presenting global warming potentials (GWPs) of over 1000 times that of carbon dioxide. New refrigerants with low GWPs have been studied. However, many of these are either flammable, have low volumetric capacities, or require large design changes, significantly raising the equipment costs. In this manner, a satisfactory solution for this issue has not yet been achieved (14,15).

On the other hand, in the development of electronic systems, higher amounts of current densities in integrated circuits are required in smaller and smaller devices. This leads to higher demands on the cooling systems, which cannot be met by the current fan-cooling based solutions, and to severe thermal management problems due to the ongoing miniaturization. Furthermore, other growing cooling needs, such as the local cooling of blood and tissues during microsurgery, require new cooling systems, since the ones existent are not suitable (20,21).

These constraints added to the search for environmental-friendly methods lead to an increasing interest in the development of alternative HVAC technologies. Among the different recourses studied, solid-state technologies are based on a solid refrigerant coupled with an environmentally harmless heat-transfer fluid. This new technology has the potential to be more efficient in cooling and energy conversion applications than the currently used. To produce useful temperature differences and achieve relevant cooling, the solid refrigerant must by a material that present a large caloric effect (20,22–24).

2.2.2. The elastocaloric effect

Caloric effects are observed as the material releases/absorbs heat or undergoes a change in its temperature when exposed to an external field. The appropriate stimuli to achieve such caloric effects can be magnetic, electric, hydrostatic, or elastic, defining the magnetocaloric, electrocaloric, barocaloric, and elastocaloric effects, respectively (20,25).

These effects are particularly large when associated with the change of enthalpy in first-order phase transitions. Thermodynamically, in a two-phase equilibrium, the phases present the same free energy. As the free energy is equal to the enthalpy minus the temperature times the entropy, these separate contributions may be used to control the obtained caloric effect since small variations of external parameters lead to significant changes in these quantities. If the temperature of the materials is maintained during transformation, exothermic and endothermic reactions will result in heat release and absorption, and changes in entropy will be proportional to the exchanged heat. When the transition occurs adiabatically, the phase transformation is associated with a change in the material's temperature (22,26).

Among the several caloric effects, the magnetocaloric effect has been extensively studied, and devices that achieve temperatures differences of around 30K have been developed. However, these devices still present modest specific cooling powers and are based on rare earth-materials, resulting in expensive products that have failed to be applied. In turn, elastocaloric materials, which have been known for almost 40 years, has only recently experienced large research interest in developing new materials for solid-state refrigeration (22,23,27).

The elastocaloric effect is the mechanical analog of the magnetocaloric effect. It is defined as an isothermal entropy change or an adiabatic temperature change that occurs when certain materials are subjected to or released from a stress field, i.e., mechanical loading or unloading. This effect is related to stress-induced, first-order phase transitions, where coupling between an externally applied stress and the lattice is observed (26,28).

In comparison to other caloric alternatives, elastocaloric materials, also known as thermoelastic materials, present large available latent heat and large adiabatic temperature changes with a relatively simple mechanical control. Hence, they have the potential to operate at highly efficient systems with competitive costs. Accordingly, the US Department of Energy has identified elastocaloric technology as the HVAC alternative technology with the highest

potential (19). To get to this conclusion, an analysis was made by scoring different candidates according to the technical energy savings potential, other non-energy benefits, and cost/complexity criteria. The final ranking obtained is presented in Figure 2-9 (19). Detailed information on the technical energy saving potential and reported heating and cooling energy savings of elastocaloric-based technology in comparison to other HVAC alternatives can be found in APPENDIX I – Energy saving potential of elastocaloric-based HVAC .

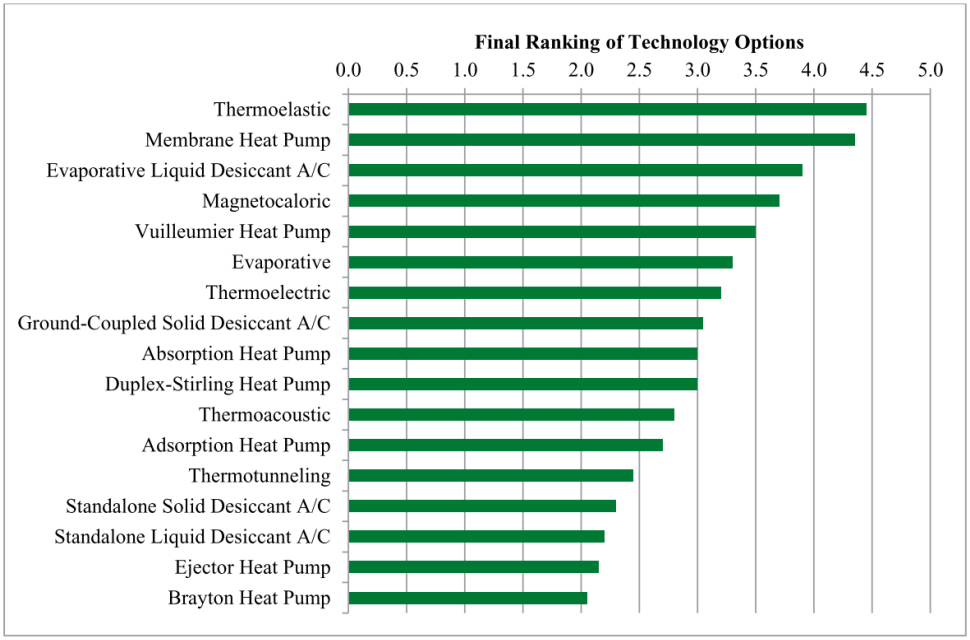

Figure 2-9 – Final ranking of HVAC alternative technology options developed by the U.S. Departement of Energy (19)

Shape memory alloys (SMA), which undergo stress-induced reversible MT in the superelastic state, are good candidates as elastocaloric/thermoelastic materials. The elastocaloric effect in these alloys has been studied over the past years, aiming to obtain information about the actual cooling potential of shape-memory based elastocaloric cooling devices (22,23,27,29,30). However, a 2017 report by the U.S Department (31) stated that, in order to develop a usable SMA-based cooling system, significant research is still required. Among the activities recommended, the development of different thermoelastic materials that meet the necessary properties is essential.

2.2.3. The use of shape memory alloys as solid-state refrigeration materials

Superelastic shape memory alloys undergo a heat-releasing transformation from austenite to martensite and a reverse heat-absorbing transformation from martensite to austenite during loading and unloading, respectively. In this manner, by exposing these alloys to subsequent mechanical straining and releasing, the combined caloric effects can be used in the realization of thermodynamic cycles both for cooling and heating purposes (24,27,32).

A basic adiabatic cooling cycle of a superelastic alloy is constituted by four stages, as illustrated in Figure 2-10 (27,32):

1) Adiabatic loading of the SMA component, resulting in its temperature increase;
2) Allowing the material's heat to flow out while loaded;
3) Adiabatic unloading of the SMA component, resulting in its temperature decrease, reaching a temperature below the initial;
4) Allowing heat to flow into the material, resulting in its temperature increase.

To accomplish the desired cooling, the design of the device must assure that the heat flow's stages 2 and 4 are related to a heat sink and a heat source, respectively. This can be developed either by cyclically timing the oscillation of the SMA component between the two heat exchangers or continuously circulating it. These devices can be based on direct thermal contact of the elastocaloric component to the heat sinks or they can rely on a fluid that acts as a heat transfer medium. Examples of different proposed devices can be found in Ref. (33–38).

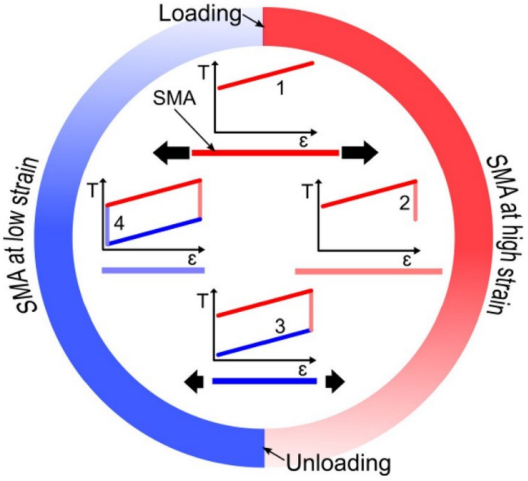

Figure 2-10 – Typical adiabatic elastocaloric cooling cycle (32)

A variety of possible thermodynamic cycles have also been explored by mixing adiabatic and isothermal stages during the direct and reverse MTs reactions, aiming to obtain higher efficiencies in different devices. Additionally, by alternating the timing sequence or circulation, the elastocaloric system could work as a heat source instead (32,39).

To evaluate the thermal efficiency, the coefficient of performance (COP) is conventionally used. It is defined as the ratio between the absorbed heat, Q_c, and the applied work, W (Eq. 1). Under ideal conditions, the absorbed heat is equal to the transformation's latent heat ΔH, and the COP_{mat}, which only depends on the material's properties, is given by Eq. 2 (40).

$$COP = \frac{Q_c}{W} \tag{1}$$

$$COP_{mat} = \frac{\Delta H}{W} \tag{2}$$

Both the required work and the absorbed heat are intrinsically related to the MT that takes place in the shape-memory element. The first, being directly proportional to transformation's mechanical hysteresis, and the second, to the MT's latent heat. These properties, in turn, are defined by the alloy's chemical composition and thermomechanical processing. Thereby, to

obtain efficient usable systems, besides optimizing the device's design and thermodynamic cycles, the alloy development is critical as the material's properties are intrinsically related to the cooling performance (32,41). Accordingly, the material's requirements and current developments will be assessed in the next topics.

2.2.4. Material's requirements

The first requirement for the shape-memory component is that it must present SE on the working temperature. To achieve this type of behavior, and to prevent the occurrence of non-recoverable strains, Af must be lower than the required cooling temperature. However, since the stresses required to induce the MT increase with increasing temperature in relation to Af, Af should not be too low to avoid the need for excessive loading (32). Sehitoglu *et al.* (2018) (42) have also pointed out that considering alloys with higher Md temperatures is a good strategy to obtain larger superelastic temperature ranges.

Thermodynamically, the alloy should present a giant elastocaloric effect, resulting in large temperature changes. The theoretical change in temperature can be related to the transformation's entropy changes, $\Delta S_{MT,}$ and latent heat, ΔH_{TM}, by Eq. 3 and Eq. 4, respectively, where C_p is the heat capacity (41–43):

$$\Delta T_{th} = \frac{T\Delta S_{TM}}{C_p} \quad (3)$$

$$\Delta T_{th} = \frac{\Delta H_{TM}}{C_p} \quad (4)$$

Thus, in order for the alloy to present a large cooling potential, ΔS_{MT} and ΔH_{TM} should be as large as possible. From a mechanical point of view, a low working input is desirable to obtain large COP. The working input is the work required to induce the MT. Hence, besides presenting adequate transformation temperatures, alloys with low stress to induce the MT and low transformation's hysteresis are preferable (32).

At last, but not least, the alloy should be able to withstand millions of loading cycles, as the component must operate continuously. This means that both functional and mechanical stability

and fatigue resistance are essential material properties for the development of cost-effective operational devices (23,27).

As a summary, five criteria can be defined to assess the potential of an elastocaloric material. These are presented in Table 2.1 associated with measurable material's properties:

Table 2.1 - Alloy criteria for elastocaloric use.

Criteria	Material properties
Large caloric effect	$\uparrow \Delta H_t$
Low mechanical work input	$\downarrow \sigma_{Ms}$, ↓mechanical hysteresis
High functional stability	↓dAf and $d\Delta H_t$ during cycling
Good structural stability	↓Nf
Adequate transformation temperature and superelasticity	Af slightly below room temperature for room temperature applications

Functional and structural fatigue limit the service life of the shape memory material employed as refrigerant and were pointed out as the main barrier for elastocaloric cooling application (23,27,37). For that, this work will be focused on minimizing the degradation processes during cycling by developing a potentially low hysteresis alloy that can still present considerable caloric effects.

2.2.5. State of the art – SMAs for elastocaloric applications

The elastocaloric effect was firstly explored in FeRh alloys, associated with an antiferromagnetic-ferromagnetic phase transition. Despite the high entropy changes and the giant elastocaloric effect, the high cost of the rare-earth Rh limited further development of these alloys (44–46).

The potential of SMAs in solid-state refrigeration has attracted the attention of Quarini and Prince (2004)(24), who evaluated the enthalpy changes during direct and reverse MTs as well

as temperature changes during loading and unloading of a superelastic $Ni_{50.7}Ti_{49,3}$. As a result, they reported excursions of +16°C and -14°C of the ambient temperatures and obtained a deduced COP of 12.6. With these results, it was demonstrated that the solid-state cooling effect using shape memory alloys was real and should be explored.

Further investigations of the elastocaloric effect associated with the MT in SMAs for solid-state cooling were developed by Bonnot *et al.* (2008)(26). They observed that the same isothermal entropy change can be obtained both by inducing the structural transition by strain or stress. A large elastocaloric effect has been achieved in the tested $Cu_{68.13}Zn_{15.74}Al_{16.13}$ single crystal. Mañosa *et al.* (2009)(22) estimated temperature shifts larger than those reported for giant magnetocaloric materials in a Cu-Zn-Al single crystal, reaffirming the potential use of shape memory alloys for close-to-room temperature mechanical refrigeration. Cui *et al.* (2012)(47), on the other hand, projected that efficiencies of up to 83.7% of the theoretical Carnot cycles could be achieved with elastocaloric technology associated with the MT's latent heat. As a comparison, efficiencies of up to 70% were calculated for magnetocaloric technology, and up to 60%, for commercial vapor compression technology.

The elastocaloric effect in Cu-Zn-Al alloys has also been reported by Grància-Condal *et al.* (2018)(48), Qian *et al.* (2016)(49), Vives *et al.* (2011)(50) and Mañosa *et al.* (2013)(51). Grància-Condal *et al.* have performed a calorimetric study of the elastocaloric effet on a $Cu_{68.3}Zn_{14.2}Al_{17.5}$ alloy and observed a temperature change of 12.3K driven by moderate uniaxial compressive stress. Also under compression, Qian *et al.* obtained an adiabatic temperature change of 4K for $Cu_{68}Al_{16}Zn_{16}$. Vives *et al.*, in turn, observed heterogeneities on the temperature distribution during the reverse strain-induced MT in a Cu-Zn-Al single crystal. For that, they highlighted the importance of controlling the microstructure dynamics to get maximum undercooling in the desired regions of the sample. Mañosa *et al.* observed that both isothermal entropy and adiabatic temperature changes are large and reproducible in a polycrystalline Cu-Zn-Al alloy over a broad temperature span of ~130K.

Among studies in other Cu-based alloys, worth noting elastocaloric effects have been reported in Cu-Al-Mn (49,52,53). Xu *et al.* (2016)(52) measured a temperature shift of 13K, covering a range of over 100K in a columnar-grained $Cu_{71.5}Al_{17.5}Mn_{11}$. For a microwire with a similar composition, Yuan *et al.* (2019)(53) measured a reversible adiabatic temperature change of 4K

and noted low transformation hysteresis while Qian *et. al.* (2016)(49) calculated a potential COP of approximately 13.3 for a $Cu_{73}Al_{15}Mn_{12}$ alloy.

In TiNi alloys, Cui *et al.* (2012)(47) noted that a coefficient of performance as high as 11 can be achieved on elastocaloric cooling based on a commercial TiNi wire, measuring a temperature change of 17 °C. Ossmer *et al.* (2014)(54) investigated TiNi films and observed an undercooling of -16K upon mechanical unloading under adiabatic conditions and a coefficient of performance of 7.7 was determined. Pataky *et al.* (2015)(55) measured an adiabatic temperature change of 14°C in a TiNi single crystal and Zhou *et al.* (2018)(56) obtained an undercooling of -11K and a COP of 4.5. These results show that a large elastocaloric effect can be achieved in TiNi alloys. However, their fatigue life is a drawback in their potential use for elastocaloric cooling, as it has been soon pointed out by Quarini and Prince (2004)(24), Cui *et al.* (2012)(47) and Ossmer *et al.* (2015a)(57).

While high transformation enthalpy, and, hence, caloric effects are obtained in TiNi, the adiabatic temperature change has been shown to be proportional to the mechanical work released by the reverse martensitic transformation during unloading by Ding *et al.* (2021) (58). The high transformation's mechanical work is intimately related with the large B2-B19' transformation's hysteresis that take place in TiNi alloys, resulting in high energy loses, cyclic degradation and jeoperdazting structural and functional fatigue (59–61). The large mechanical hysteresis of binary TiNi was also related to a decreased COP of this alloy when compared to a Cu-Zn-Al alloy by Tušek *et al.* (2015) (62). In this sense, efforts have been made to tailor binary TiNi alloys, seeking adequate compromise between caloric effect, mechanical work and satisfatory fatigue resistance.

Optimizing the alloy microstructure was mostly done by using nanoncrystaline structures and grain size engineering (63–69). Lin *et al*. (2022) (66), Dang *et al.* (2023) (68), Chen *et al.* (2022) (69) and Chen *et al.* (2023)(65) showed that the elastocaloric cooling performance of polycrystalline TiNi can be enhanced via grain refinement through proper thermomechanical processing. Improved COP and cyclic stability were obtained, with decreases in the adiabatic temperature change. Xu et al. (2022) (70) proposed a phase field simulation based on a grain size dependent and thermomechanically coupled model to improvethe elastocaloric effect of TiNi, also highlightng the role of texture and gradient nano grain structures to optimize the material's COP. A Ni-concentration dependent model was latter suggested, to formulate the

martensitic transformation start temperature by Xu et al. (2023) (71). On the other hand, elastocaloric devices based on TiNi have been developed using compressive stress (65,72,73), while the use of shear stresses have been explored by Zhu *et al.* (2022) (74)

Another alternative on materials development lies in the study of TiNi-based alloys with small transformation hysteresis, seeking alloys with satisfactory mechanical and functional stability but that still present relatively large latent heats. In Figure 2-11-a, it can be observed that enthalpy variations comparable to binary TiNi's can be obtained in ternary TiNi-based systems (75). Figure 2-11-b presents the transformation's enthalpy ΔH_{AM} and the transformation's temperature hysteresis ΔT_H, which is intrinsically related to the mechanical hysteresis, of several TiNi-based alloys (76). Despite the inverse relationship between these two properties, ΔH_{TM} and ΔT_H, alloys with relatively low hysteresis and still attractive latent heat such as Ni-Ti-Cu, Ni-Ti-Cu-Co, Ni-Ti-Pd, Ni-Ti-V, and Ni-Ti-Cr can be achieved, representing good candidates to be explored.

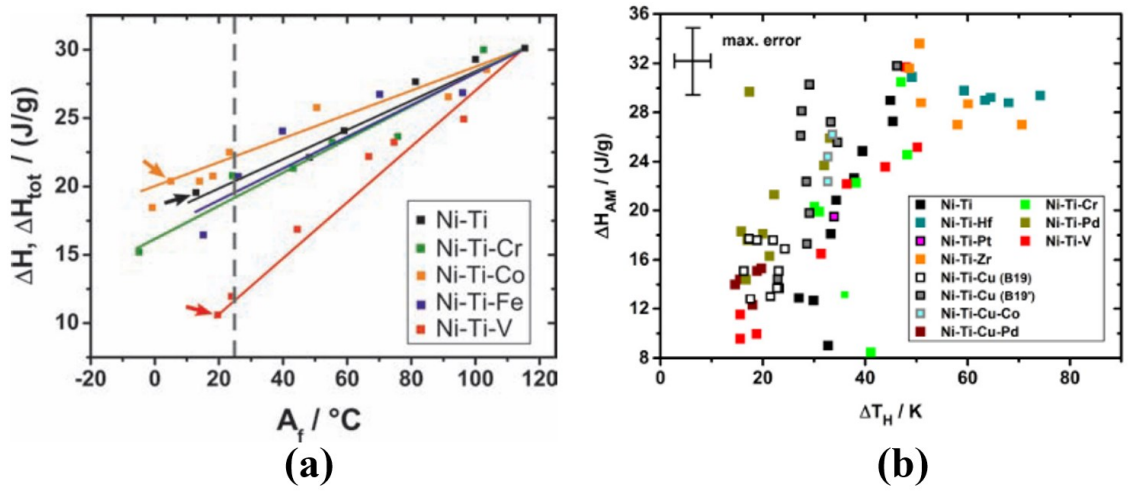

Figure 2-11 - (a) Latent heat as a function of Af for different NiTi-based ternary alloys (75) **and (b) enthalpy variation and thermal hysteresis of the martensitic transformation in different NiTi-based alloys** (76)

The stress hysteresis of SMAs can be largely reduced by high crystallographic compatibility between the austenitic and martensitic phases. One of the cofactor conditions is measured by how close the middle eigenvalue of the transformation stretch matrix λ_2 is to 1 (77,78).

Accordingly, the relation between the hysteresis width ΔT_H and λ_2 of various NiTi-based alloys, as well as the dependence of the latent heat of the austenite-martensite transformation ΔH_{AM} to this cofactor value, can be observed in Figure 2-12. Ni-Ti-Cu-Pd alloys is highlighted for the high crystallographic compatibility and low temperature hysteris.

It can noted from Figure 2-12 that the alloys that present greater MT's crystallographic fit, present both the lowest transformation hysteresis and latent heat, reinforcing the tendency previously observed in Figure 2-11-b. From an elastocaloric cooling perspective, these alloys might have the potential of undergoing lower fatigue damage and presenting lower required working input. As a result, even with latent heats lower than that of binary NiTi and Cu-based alloys, these types of alloys have the potential to present high COPs and good fatigue resistance.

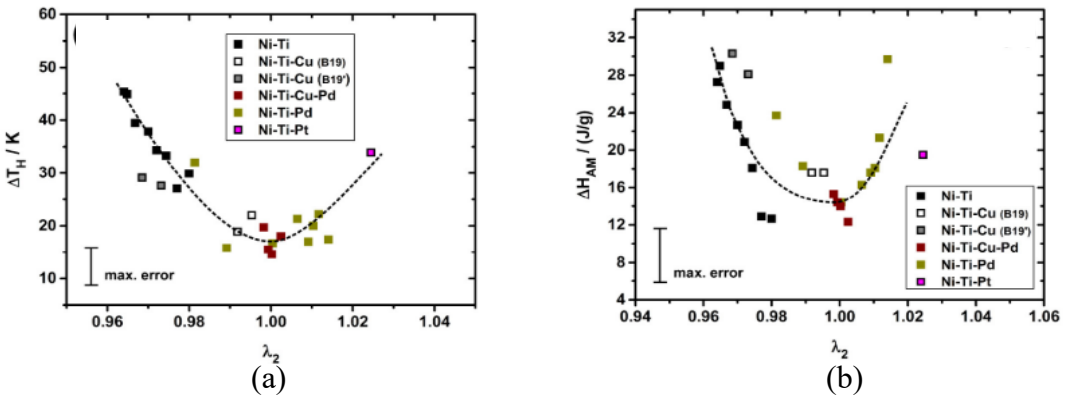

Figure 2-12 – Relation between transformation's (a) thermal hysteresis and (b) latent heat to the middle eigenvalue of the transformation stretch matrix λ_2 (76)

Later, Bruederlin *et al.* (2018)(79) noted that $Ti_{54.7}Ni_{30.7}Cu_{12.3}Co_{2.3}$ and $Zn_{45}Au_{30}Cu_{25}$ were the only alloys to the date of their publishing that achieved all the required cofactor conditions for great crystallographic compatibility. Due to the high cost of $Zn_{45}Au_{30}Cu_{25}$, they pointed TiNiCu-based alloys as promising candidates in obtaining fatigue-resistant alloys.

The elastocaloric effect has additionally been reported in Fe-Pd single crystals (80–82), in Pd-In-Fe (83), as well as in the magnetic shape memory alloys Ni-Mn-Ga-based (84–87), Ni-Mn-Sn (Cu) (85), Ni-Mn-In-based (88–91), Ni-Fe-Ga (55,92–97), Ni-Mn-Sn-based (94,98–101), Co-Ni-Al (55,102), Co-Ni-Ga-based (103) and in the ferroelectric Ba-Sr-TiO (104,105). Literature reviews, gathering different alloys according to properties required for elastocaloric

cooling, have been provided by Kirsch *et al.* (2018)(32), Qian *et al.* (2016a)(39) and Sehitoglu *et al.* (2018)(42).

Figure 2-13 presents the adiabatic temperature changes, ΔT_{ad}, vs the coefficient of performance, COP, in different systems, under tensile and compressive loading. In accordance to previous observations, despite the high adiabatic temperature change, TiNi binary alloys present a relatively small COP under tensile stresses. The efficiency of these alloys can be improved by using compressive loading. On the other hand, TiNiCu and CuZnAl systems can be highlighted for their balanced combination of ΔT_{ad} and COP. At last, the $Ni_{45}Ti_{47.25}Cu_5V_{2.75}$ alloy was identified by Wieczorek *et al.* (2017)(75) as the most promising candidate shape memory alloy for elastocaloric cooling due to its great caloric effect/efficiency combination.

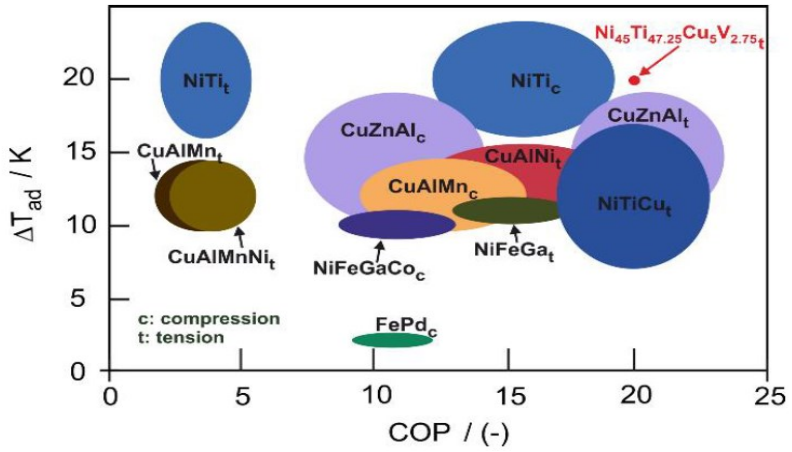

Figure 2-13 – Adiabatic temperature change and coefficient of performance in shape memory systems under tensile and compressive stresses (39,75)

Besides NiTiCuV, Wieczorek *et al.* (75) have studied other TiNi-based alloys, as observed in Table 2.2. NiTiCuCo and NiTiCuFe can be pointed out for their high ΔH_{TM} and COPs. Even if their strain recoveries were not satisfactory, these results reinforce that TiNiCu-based alloys with small transformation hysteresis are alloys that can indeed be worth exploring as alternatives to TiNi, in an attempt to obtain elastocaloric materials with a high COP and a satisfactory fatigue resistance.

Table 2.2 - Compilation of elastocaloric cooling key parameter for NiTi-based SMAs (75)

Composition	Heat treatment (°C/min)	A_f/(°C)	ΔH_{tot}/(J/g)	W/(J/g)	COP/(−)	Strain recovery ($N = 1$)/%	Strain recovery ($N = 10$)/%
$Ni_{51.1}Ti_{48.9}$	500/10	31.8	15.1	3.1	4.8	99.1	95.4
$Ni_{51.1}Ti_{48.9}$	550/3	4.0	14.6	2.5	5.8	97.9	87.4
$Ni_{50}Ti_{44}V_6$	800/10	−1.5	10.3	0.7	14.7	96.6	85.1
$Ni_{45}Ti_{47.25}Cu_5V_{2.75}$	500/10	5.2	9.2	0.5	20.0	99.3	98.7
$Ni_{39.83}Ti_{50}Cu_5Co_{5.17}$	500/10	0.2	18.3	2.6	7.0	53.4	35.6
$Ni_{42.87}Ti_{50}Cu_5Fe_{2.13}$	500/10	0.5	19.9	1.9	10.5	86.1	65.3
$Ni_{50}Ti_{44}V_6$	500/10	—	0	0.4	—	99.9	97.8
$Ni_{50}Ti_{44}V_6$	600/10	—	0	2.1	—	92.2	83.2
$Ni_{44}Ti_{50}Co_6$	500/10	16.4	14.8	7.1	—	20.0	15.3
$Ni_{44}Ti_{50}Co_6$	800/10	18.3	22.1	4.1	—	10.6	7.1

Sehitoglu *et al. (2018)*(42) presented results of the fatigue response of several important shape memory alloys versus the normalized cycling strain range $\Delta\varepsilon/\varepsilon_{th}$, where $\Delta\varepsilon$ is the strain amplitude and ε_{th} is the transformation strain (Figure 2-14). From this perspective, the Heusler magnetic Ni_2FeGa can be highlighted due to its relatively high fatigue life. However, these alloys brittleness is a significant drawback in their production. Regarding TiNi-based alloys, it can be noted that the binary alloy's fatigue life can, in fact, be improved by adding Cu.

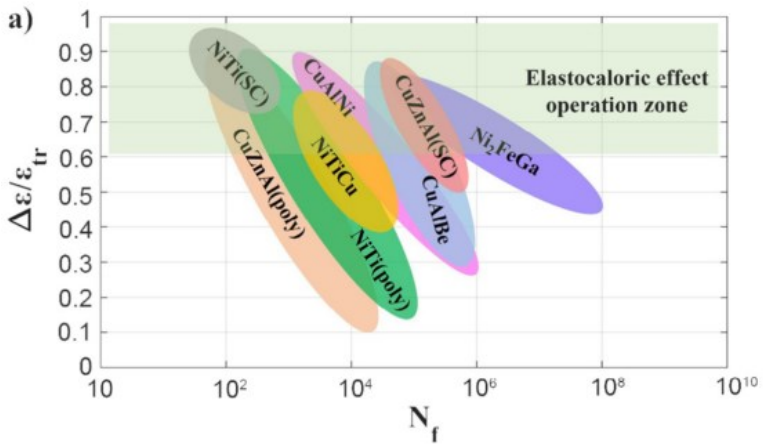

Figure 2-14 – Fatigue life of different alloy systems as a function of the normalized strain amplitude (42)

Based on this literature assessment, TiNiCu-based alloys were noted to be good potential candidates on the development of fatigue resistant shape memory alloys for elastocaloric cooling. For that reason, TiNiCu alloys will be briefly discussed in the next topic and a

gathering of NiTiCu-based alloys studies relevant for such application will be presented. A summary of thermodynamic properties and COP measurments can be found in APPENDIX II – Thermodynamic properties and COP measurements of TiNi and TiNiCu-based alloys.

2.3. TiNiCu Alloys

2.3.1. General properties

Binary near-equiatomic TiNi alloys have been intensively investigated and still are the most important commercial SMAs thanks to their great functional properties. However, to meet some specific needs and expand their applications range, ternary and quaternary TiNi-based SMAs have been developed. In this manner, researchers seek increasing transformation temperatures, controlling transformation hysteresis, and/or improving mechanical properties and corrosion resistance of binary TiNi alloys (10,106,107).

The addition of some amounts of copper in substitution for nickel results in ternary alloys with narrower thermal and stress transformation hysteresis, lower composition sensitivity of the transformation temperatures, and increased damping capacity when compared to the binary NiTi alloys. These characteristics are usually associated with improved structural and functional fatigue properties as well as better actuation response (1,106,108–110).

2.3.2. Present phases

The Cu added in binary NiTi occupy Ni sites in the crystal structure. The parent phase remains as the body centered cubic CsCl BCC_B2 present in binary TiNi up to additions of 30at%Cu, forming a ternary (Ni,Cu)Ti phase. These alloys present a reversible MT and, hence, the SME. However, Cu additions higher than 10at% embrittle the alloy and conventional manufacturing processes become difficult (1,111).

In this system, martensite with both monoclinic B19’ and orthorhombic B19 crystal structures can be present, depending on the Cu content. When the Cu content is lower than 7at%, the alloy goes through a direct B2-B19’ transformation. When it is higher than 7at%, a two-step B2-B19-B19’ MT is observed and microstructures containing B19, B19’ or both B19 and B19’ can be obtained. By increasing the Cu content, the B19 transformation start temperature (Ms’) slightly increases whereas the B19’ transformation start temperature (Ms) decreases drastically, as it is

shown in Figure 2-15. This results in a wider temperature range over which B19 martensite is stable with increasing Cu content (1,112,113).

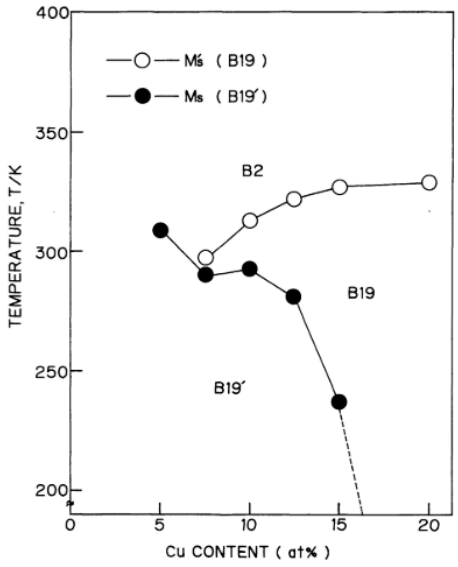

Figure 2-15 – Cu-content dependence of transformations temperatures in Ti-Ni-Cu alloys (112)

It was previously shown that when the Cu content exceeds 15at%, the B19-B19' transformation is not detected even at liquid nitrogen temperature (1), which is in accordance to Nam *et al.* (1990)(112) findings. More recent studies have detected the two-stage transformation in Ni-Ti-$Cu_{16at\%}$ by in situ XRD analysis (114) and in Ni-Ti-$Cu_{20at\%}$ by XRD experiments with synchrotron radiation (115). However, the fraction of B19 transformed into B19' martensite is small, and this transformation was not detected neither by DSC nor by ER analyses. Accordingly, it was later stated that for Cu contents higher than 20at%, the second transformation is suppressed entirely, and the MT becomes a single step B2-B19 transformation (116).

Regarding second-phases, the presence of $Ti_2(Ni,Cu)$ phase has been observed in heat-treated alloys. This face-centered cubic intermetallic is formed at a nanometric scale and is initially coherent with the B2 phase. When incoherent, they affect the growth of the martensitic phase since they don't undergo a MT (110,117).

Thermodynamic assessments aided by the experimental and CALPHAD (CALculation of PHAse Diagrams) approaches have been performed. The stable phases in the Ni-Ti-Cu system were summarized by Zhang *et al.* (2013)(118) and Zhu *et al.* (2014)(119) and are presented in Table 2.3. The stoichiometries of the phases are presented along with their crystal structures. Atoms that occupy the same site on the crystal structure are represented within parenthesis. The presence of the intermetallic austenitic TiNi B2 phase can be noted, as well as Ni, Cu, and Ti solid solutions. Other binary intermediate phases with ternary solubility such as Ni_3Ti, NiTi, Cu_4Ti, Cu_2Ti, Cu_3Ti_2, Cu_4Ti_3, CuTi, $CuTi_2$ are also pointed out. The τ_i phases, in turn, refer to ternary compound phases.

Table 2.3 – Thermodynamically stable phases in the Ni-Ti-Cu system

Phase	Prototype	Pearson symbol	Temperature range (°C)	Composition range
TiNi, Ti(Ni,Cu), BCC_B2	CsCl	cP2	<1311	Dissolves ~30 at%Cu with ~50 at%Ti
γ (Ni), FCC_A1	Cu	cF4	<1455	%Ti < 0.14
γ (Cu), FCC_A1	Cu	cF4	<1085	%Ti < 0.14
β-Ti, BCC_A2	W	Cl2	882 - 1670	Dissolves: ~14at%Cu, ~10at%Ni
α-Ti, HCP_A3	Mg	hP2	<882	Dissolves: ~1.6at%Cu, ~0.2at%Ni
Ni_3Ti	Ni_3Ti	hP16	<1380	Dissolves ~5 at%Cu
Ti_2Ni, $Ti_2(Ni,Cu)$	$NiTi_2$	cF96	<984	Dissolves ~6 at%Cu
Cu_4Ti	Au_4Zr	oP20	<885	78 – 80.9 at%Cu, dissolves ~1 at%Ni
Cu_2Ti, $(Cu,Ni)_2Ti$	Au_2V	oC12	870 - 890	Dissolves ~7 at%Ni
Cu_3Ti_2	Cu_3Ti_2	tP10	<875	Dissolves ~5at%Ni

Cu_4Ti_3	Cu_4Ti_3	tl14	<925	Dissolves ~7 at%Ni
CuTi	γCuTi	tP4	<982	48–52 at%Cu, dissolves ~2 at%Ni
$CuTi_2$, $(Cu,Ni)Ti_2$	$MoSi_2$	tl6	<1005	Dissolves ~13 at%Ni
τ_1 (CuNiTi)	$MoSi_2$	tl6	<1190	Dissolves 13–55 at%Cu
τ_2 $(Cu,Ni)_3Ti_2$		tP10	120 - 850	~3–5at%Cu with 40at%Ti
τ_4 ($CuNi_{14}Ti_5$)	$BaPb_3$	hR12	930	~5–9 at%Cu
τ_6 ($CuNi_2Ti$)	$TiAl_3$	tl8	870, 900	~25–26.5 at%Cu

When compared to the binary near equiatomic NiTi alloys with an excess of Ni, the addition of Cu leads to the prevention of Ti_3Ni_4 precipitation and the suppression of the R-phase. However, the B2 ↔ B19 MT is associated with low mechanical hysteresis (1,120).

2.3.3. NiTiCu-based alloys for elastocaloric cooling

Besides Wieczorek *et al.* (2017)(75), other researchers have evaluated the use of NiTiCu and NiTiCu-based shape memory alloys for elastocaloric cooling applications. Bechtold *et al.* (2012)(28) have compared the elastocaloric properties of TiNi and TiNiCu films and their relation to functional fatigue. They have noted that both materials presented similar elastocaloric response but TiNi temperature changes degrade during cycling while TiNiCu doesn't, as illustrated in Figure 2-16. Moreover, stable elastocaloric effect were achieved in nanocrystalline $Ti_{50}Ni_{40}Cu_{10}$ (121), and cold-rolled and aged (Ni,Cu)-rich (122) and Ti-rich (123) TiNiCu alloys.

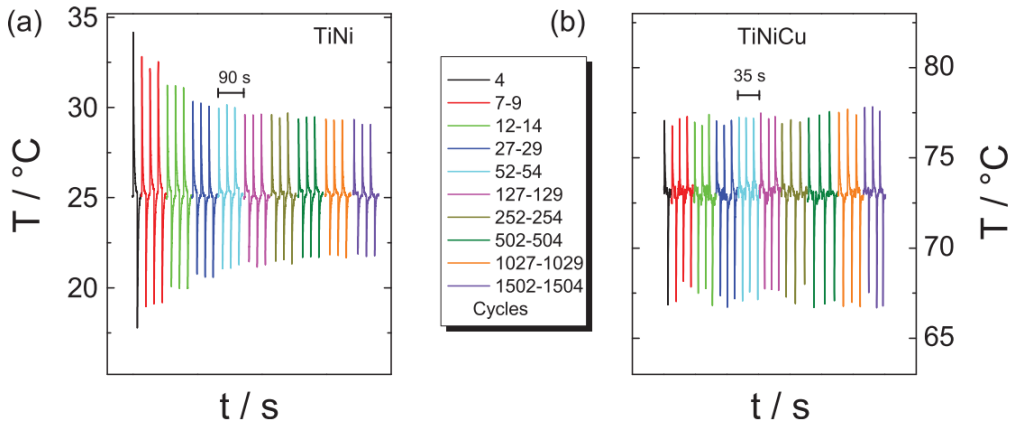

Figure 2-16 - Time-temperature profiles of TiNi and TiNiCu during superelastic cycling (28)

Chluba *et al.* (2015)(124) reported $Ti_{54}Ni_{34}Cu_{12}$ films as ultralow-fatigue shape-memory films that withstood at least 10 million transition cycles. However, these alloys presented a high Af temperature of 62 °C. Then, aiming to adjust the transformation temperatures to the potential working temperature of a cooling device, Chluba *et al.* (2016)(125) developed Ti-rich TiNiCuCo and TiNiCuFe films. By adding Co and Fe, they were able to reduce the Af temperature significantly. Additionally, they obtained TiNiCuCo alloys with latent heat comparable to that of TiNiCu of 7.9 J/g, adiabatic temperature changes comparable to that of the TiNi films of 10K, and a COP 25% larger than that of binary TiNi. A transformation strain of ~1.6% and an operational temperature range of ~50 K were also measured. Ossmer *et al.* (2015)(57) noted that, unlike TiNi films, TiNiCuCo films present negligible fatigue and retain the local characteristics of the elastocaloric effect. Compared to TiNi films, which exhibited an adiabatic temperature cooling of -16 K, these films exhibited a reduced temperature change of -12 K. However, they also presented a reduced work input for pseudoelastic cycling, resulting in an improved material's COP of 15.

Ultra-high thermal and superelastic cyclic stability was latter obtainined in a bulk TiNiCuCo alloy by Ahadi *et al.* (2021) (126). Transformation temperature changes of ~0.1°C aftwer 200 cycles were obtained, attributed to the presence of semi-coherent Ti_2Cu precipitates which would help satisfy the compatibility criteria. Low hysteresis and high cyclic stability was also reported in bulk TiNiCuFe (127,128).

From another perspective, Frenzel *et al.* (2015)(76) studied the effect of alloy composition on the martensitic start temperatures and latent heats in TiNi-based alloys. Their results show that latent heats as high as 30 J/g can be obtained in TiNiCu alloys with 5at%Cu, which undergo a B2-B19' transformation. For the B2-B19 phase transformation in alloys with 10at%Cu, transformations enthalpies of 17 J/g were measured. Quaternary TiNiCuCo and TiNiCuPd were also studied and latent heats as high as 26 J/g and 15.3 J/g were obtained respectively. These results are shown in Figure 2-12. Alloys from the TiNiCuPd system were the ones that presented λ_2 closer to 1 and, hence, the lowest transformation's hysteresis.

Accordingly, Meng *et al.* (2015)(129) found that a $Ti_{50.5}Ni_{33.5}Cu_{11}Pd_{4.5}$ alloy exhibits excellent thermal stability even after 5000 thermal cycles. They also observed that the hysteresis tends to decrease and that very few dislocations are introduced during thermal cycling. Li *et al.* (2018)(130) investigated the shape memory behavior and the hysteresis under load in a $Ti_{50}Ni_{33.5}Cu_{12.5}Pd_4$ alloy with near-zero thermal hysteresis and observed that the SME and hysteresis presented excellent stability during thermal cycling when the external stress is applied thanks to the rare introduction of dislocations.

A good value of COP was obtained in the $Ni_{45}Tu_{47.25}Cu_5V_{2.75}$ alloy in the studies of Wieczorek *et al.* (2017)(75). Even though the latent heats of this material are not so large, this alloy presents a sufficiently low Af temperature, low mechanical work input, and excellent functional stability. This work, which results were summarized in Table 2.2, suggests that a good combination of key parameters is essential for the material to present high efficiency and have the potential use as an elastocaloric cooling material.

More recently, Tong *et al.* (2019)(131) reported that doping Nb into $Ti_{54}Ni_{34}Cu_{12}$ significantly enhances the thermal cycling stability of the ternary material. The excellent thermal cycling and two-way shape memory effect stability of the novel TiNiCuNb was attributed to improvements in the yield strength, geometric compatibility between martensite and parent phase and introduction of β-Nb phase (131,132). These findings present Nb as an alternative to the promising V, Co, and Pd additions in the Ni-Ti-Cu system, and a new quaternary system in which potential alloys for elastocaloric cooling can be developed.

2.3.4. NiTiCu-Nb

Pioneer studies in the Ti-Ni-Cu-Nb system were performed by Louzguine *et al.* (2004)(133). Motivated by previous studies in $Ti_{60}Cu_{14}Ni_{12}Sn_4Nb_{10}$, where Nb was added as a β-Ti stabilizer, they investigated an arc-melted $Ti_{50}Ni_{20}Cu_{20}Nb_{10}$ alloy. As a result, they obtained high strength and ductile alloys with a fine microstructure constituted by a quaternary β-(Ti,Nb,Ni,Cu) solid solution, a monoclinic TiNi-type (Ti,Nb)(Ni,Cu) phase, and a $(Ti,Nb)_2(Cu,Ni)$ phase which is a solution of Nb (replacing Ti) and Ni (replacing Cu) in the Ti_2Cu phase.

In shape memory alloys, the introduction of Nb in a ternary TiNi-based system was firstly developed in NiTiHf alloys, in which it was effective in increasing the alloys' cold workability thanks to the formation of a ductile Nb-rich phase (134). Hereupon, Jiang *et al.* (2015)(135), suggested adding Nb to a brittle Ni-Ti-Cu alloy to improve its ductility since no brittle intermetallic has been found in the binary Cu-Nb phase. Accordingly, a $(Ti_{50}Ni_{38}Cu_{12})_{93}Nb_7$ alloy was designed and its microstructure, transformation behavior, and mechanical properties were investigated.

The as-cast alloy presented a microstructure composed of Ti(Ni,Cu) (B2 TiNi) and Nb-rich (β-Nb) phases. Single-step B2-B19 transformations were observed after different heat-treatments conditions of the drawn alloy. The heat-treatments were effective in changing the transformation's temperature, the ultimate tensile strength (UTS), the maximum elongation, and the critical stress for MT induction (σ^{Ms}) of the alloy. The highest UTS, of over 1500MPa, was obtained after heat-treatment at 400°C. However, these samples also presented the highest σ^{Ms}. In samples treated at 700°C, a plateau strain of near 3% was observed along with a σ^{Ms} of around 200MPa. σ^{Ms} smaller than 100 MPa were obtained in alloys treated at 500°C and 600°C, in which plateau strains smaller than 2% was observed. The austenitic finishing temperatures varied from 17°C to 40°C (135). The XRD, DSC, and tensile test results are presented in Figure 2-17.

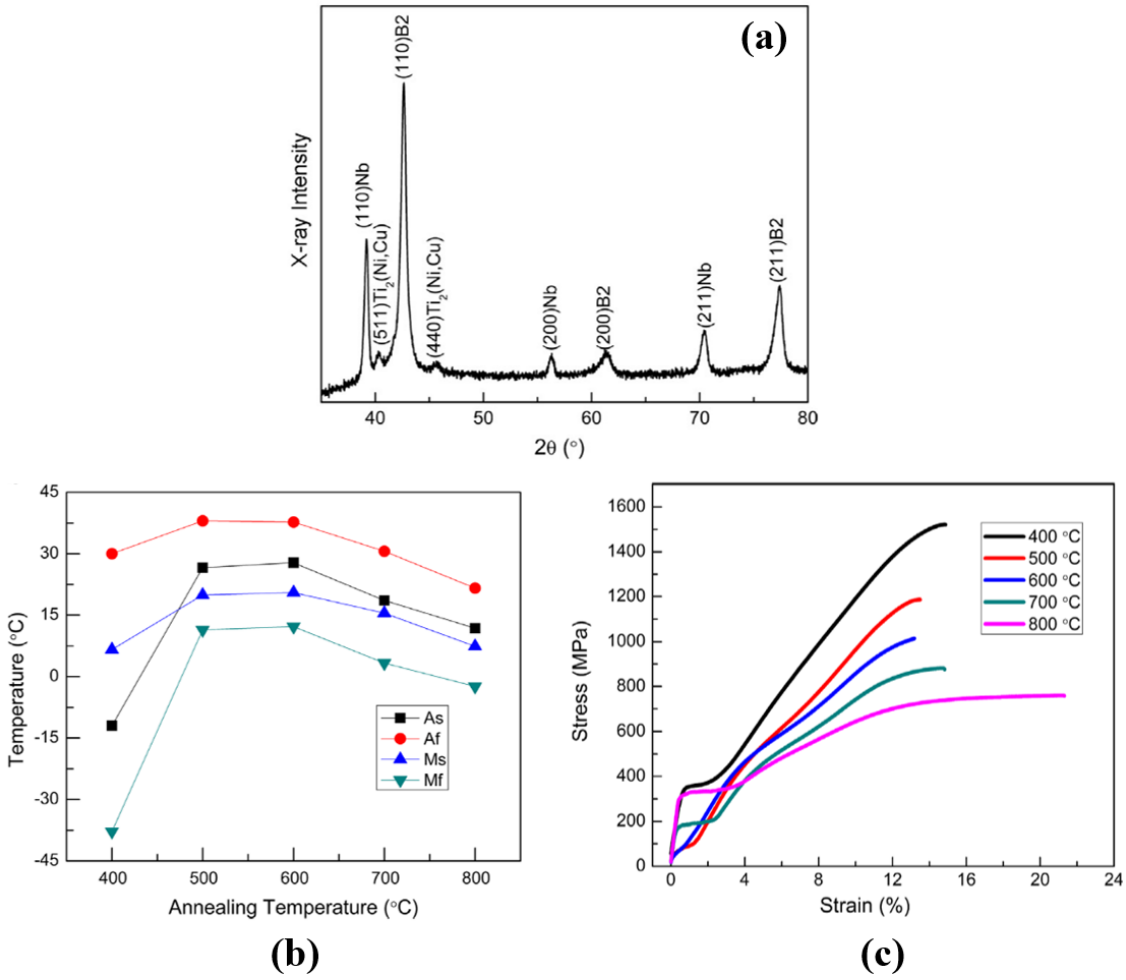

Figure 2-17 – (a) XRD results for an as-cast $(Ti_{50}Ni_{38}Cu_{12})_{93}Nb_7$ and (b) transformation temperatures tensile stress-strain curves for this alloy heat-treated at different (135)

The influence of Nb content on the MT and mechanical properties of TiNiCuNb shape memory alloys was assessed by Wang *et al.* (2016)(136). For that, arc-melted $(Ti_{50}Ni_{40}Cu_{10})_{100-x}Nb_x$ alloys with x = 0, 5, 10 and 15 at% were investigated. It was observed that the addition of Nb does lead to the presence of the ductile β-Nb phase, increasing the elongation of $Ti_{50}Ni_{40}Cu_{10}$, as it can be noted from the tensile tests in Figure 2-18-a. The addition of higher amounts of Nb resulted in increasing both σ^{Ms} and the yield strength while increasing shape recovery was also reported. Regarding the MT, all the alloys exhibited one-step B2↔B19 transformations. It was also observed (Figure 2-18-b) that while the transformation temperatures decreased with increasing Nb content, the transformation hysteresis slightly increased due to decreases in the middle eigenvalue. Besides B2 NiTi and β-Nb phases, $Ti_2(Ni,Cu)$ was also present at room temperature.

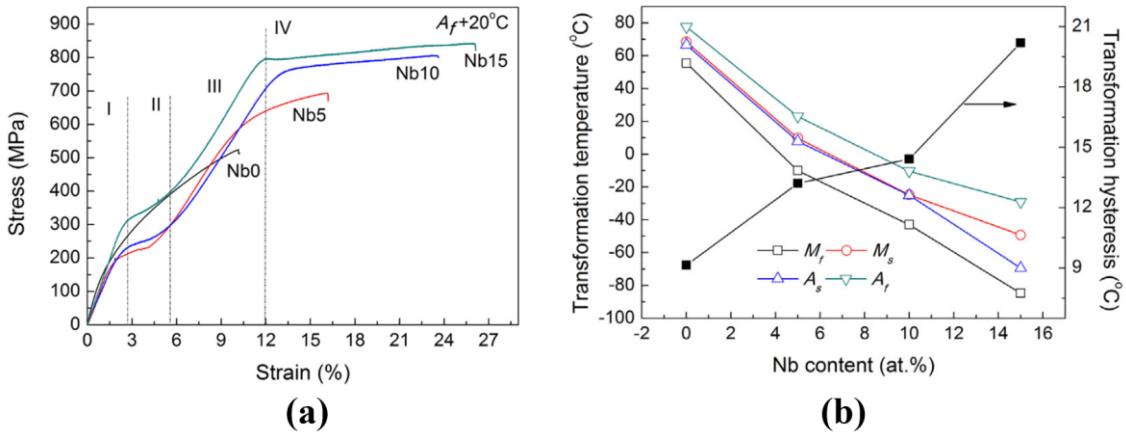

Figure 2-18 – (a) Stress-strain curves and (b) transformation temperature and hysteresis as a function of Nb content for $(Ti_{50}Ni_{40}Cu_{10})_{100-x}Nb_x$ alloys, with x = 0 (Nb0), 5 (Nb5), 10 (Nb10) and 15 (Nb15) at% (136)

Liu *et al.* (2018)(137) studied the martensitic transformation in arc-melted $(Ti_{50}Ni_{38}Cu_{12})_{100-x}Nb_x$ shape memory alloys with x = 0, 5, 10, 15 at% and detected two-step B2→B19→B19' transformation during cooling through dynamic mechanical analysis (DMA) and low-temperature XRD. However, the B19→ B19' phase transformation was not detected in the DSC analysis, in accordance with what was previously reported. According to Liu *et al.* (137), this transformation is characterized by a wide temperature interval and a small enthalpy. It was also pointed out that it may occur in temperatures lower than the detection limit. At last, regarding the transformation temperatures, it was also observed that they decrease monotonously with increasing Nb content.

These studies indicate the potential of obtaining TiNiCuNb alloys with good mechanical properties presenting a predominant B2↔B19 phase transformation, which is characterized by an intrinsic lower hysteresis than that of B2↔B19'. Their properties and characteristic transformation temperatures are influenced both by the Nb content and heat-treatment conditions, providing powerful tools for alloy optimization. Hence, there is a good research opportunity on developing and evaluating TiNiCuNb alloys that are potentially suitable for solid-state cooling applications. OBJ

3. ALLOY DESIGN

3.1. Introduction

The binary Ti-Ni system, involving stable and metastable phases, is well-explored. The austenitic phase that undergoes reversible MT, and, hence, is associated with the SME and SE, is the TiNi intermetallic. In regions of excesses of Ni, Ti_3Ni precipitates under equilibrium conditions while metastable Ti_3Ni_4 and Ti_2Ni_3 can be formed at low-temperature heat-treatments of a supersaturated TiNi matrix. In regions of excess of Ti, Ti_2Ni precipitates are observed (10).

Assessments of ternary Ti-Ni-Cu (118,138) and Ti-Ni-Nb (139–142) systems are also available. When adding Cu in binary TiNi SMAs as a substitute for Ni, TiNi remains the primary phase with additions of up to 30at% Cu, with Cu dissolved in Ni's atomic site. $Ti_2(Ni,Cu)$, $Ti(Ni,Cu)_2$, CuTi second-phases have been reported in the as-cast microstructure of TiNiCu SMAs (1,112,143–148). In turn, a typical TiNiNb SMA, $Ti_{44}Ni_{47}Nb_9$, is constituted by TiNi and nearly pure β-Nb (1).

The addition of Nb in a ternary NiTi-based SMA was firstly introduced in TiNiHf, in which it was effective in increasing the alloys' cold workability thanks to the formation of the ductile β-Nb phase (134). Hereupon, Jiang *et al.* (2015) (135), suggested adding Nb to a brittle TiNiCu alloy to improve its ductility. Studies on TiNiCuNb alloys have reported the presence of TiNi, β-Nb and $Ti_2(Ni,Cu)$ (131,132,135,136,149). However, thermodynamic assessments of the Ti-Ni-Cu-Nb quaternary system are not yet available.

Computational tools based on first principles calculations, CALPHAD, and finite element analysis can be used at different stages of alloy design, from chemical composition selection (150–152) , to processing route determination (153–155) and optimizations. The use of these type of methodologies diminishes costs and time associated with traditional experimental trials. In this context, a study of the TiNiCuNb system was performed using the CALPHAD method for selecting alloy chemical compositions for further evaluation. The aim is to design TiNiCuNb alloys that have the potential to be explored as suitable materials for solid-state cooling applications at room temperature. Formable SMAs with high cycling stability, SE at room temperature, and relatively high transformation enthalpies are desirable.

For that, element interactions and stability regions were evaluated using different configurations under equilibrium. In the chosen chemical compositions, a significant fraction of the TiNi phase must be present to obtain the functional properties. The precipitation of the β-Nb ductile phase is desirable for favoring cold working, and further testing its effects during superelastic cycling. Other second phases should be avoided to prevent alloy embrittlement. Functional properties reported in Refs. (131,135,136,149) were then related with calculable thermodynamic quantities for varying Nb contents and heat-treatment conditions. Extrapolations from reported results were used to achieve alloys with Af close to room temperature and properties that can be controlled by heat-treatments.

3.2. Methodology

Thermodynamic calculations were performed in Thermo-Calc®, using TCNI8 database. Investigated phases were based on previous experimental and CALPHAD results (118,131,135,136,138–142,149). Binary Ti-Ni was used as the reference system. Ti-Cu, Ni-Cu, Ti-Nb and Ni-Nb binary diagrams were obtained to evaluate the interaction of each solute atom with Ti and Ni. Cu-Nb equilibrium was assessed to evaluate the interaction between the two solute atoms.

The base alloy for Nb addition was a ternary TiNiCu alloy. Thus, calculations on the Ti-Ni-Cu ternary system were computed as follows: ternary equilibrium at different temperatures; evaluation of the Ti-Ni phase diagram with fixed amounts of Cu; and addition of Cu as a substitute for Ni in alloys with different Ti contents.

The effect of Nb in the Ti-Ni system was evaluated by calculating pseudobinary Ti-Ni phase diagrams with varying fixed Nb contents. In Ti-Ni-Cu, calculations were performed by adding Nb in a Ti-rich ($Ti_{52}Ni_{38}Cu_{10}$), the equiatomic-equivalent $Ti_{50}Ni_{40}Cu_{10}$ and a (Ni+Cu)-rich ($Ti_{48}Ni_{32}Cu_{10}$) base-alloys, with fixed Cu content of 10at%. In this case, three different approaches were used in pseudobinary calculations:

- Nb-addition as a stoichiometry substitute for Ni;
- Nb-addition as a stoichiometry substitute for Ti;
- Nb-addition while maintaining the Ti:Ni:Cu stoichiometric proportion.

To relate measured functional properties with calculable thermodynamic quantities, the chemical compositions studied in Refs. (131,132,135,136,149) were explored. The chemical composition of different phases was calculated at various compositions and equilibrium temperatures using single point equilibrium and property diagram calculations. Extrapolation of the results were undertaken to assess potential alloys for further investigation.

3.3. Results and Discussion

3.3.1. Thermodynamic assessment of the Ti-Ni-Cu-Nb system

3.3.1.1. Binary equilibrium calculations

The Ti-Ni phase diagram, based on Ref. (4,10), is illustrated in Figure 3-1-a. The ordered intermetallic TiNi can be observed in near-equiatomic composition. This is a B2-CsCl type structure, which undergoes the reversible martensitic transformation. The maximum solubility of Ti is 50.7 at%, only deviating slightly from the equiatomic intermetallic composition. Excesses of Ti precipitate as Ti_2Ni, which is formed from the liquid phase at 984°C. In turn, the maximum solubility of Ni is 56at%. This solubility decreases sharply with decreasing temperature, and excesses of Ni precipitate as $TiNi_3$ under equilibrium. The Ni-rich phase can be formed from the liquid in a eutectic reaction or by heat-treating a supersaturated TiNi matrix at high temperatures. However, in TiNi SMAs with excess of Ni, low-temperature heat-treatments are vastly explored to obtain metastable coherent Ti_3Ni_4 precipitates and optimize martensitic transformation temperatures and mechanical properties (10).

Ti-Cu and Cu-Ni phase diagrams were calculated based on Ref. (156) and Ref. (157), respectively. Ti-Cu interactions, Figure 3-1-b, form a complex phase diagram with various intermetallic compounds and invariant reactions. Up to 15at% of Cu can be dissolved in the high-temperature β-Ti phase whereas a decreased solubility of 1.4at% occurs in the low-temperature α-Ti. In near-equiatomic compositions, Ti and Cu form a B11 CuTi tetragonal structure. Ti_2Cu intermetallic is observed when the Ti content is higher than 50at%. Cu_3Ti_2, Cu_4Ti_3 and Cu_4Ti occur, respectively, for increasing Cu content. In turn, Ni and Cu, Figure 3-1-c, form a well-known isomorphous system, showing full solubility as a single face centered cubic (FCC) solid solution (158). This is coherent to previous observations that in Ti-Ni-Cu alloys, Cu occupies Ni sites in the TiNi structure (1).

Ni-Nb and Ti-Nb phase diagrams, based, respectively, on Refs. (159,160) and Ref. (161), are presented in Figure 3-1-d and -e. Nb and Ti, Figure 3-1-d, form a body-centered cubic (BCC) disordered solid solution (β) within a wide range of temperatures at all compositions. When the allotropic transformation of Ti occurs, the formation of α-Ti is observed whereas the β-phase becomes a Nb-rich phase. On the other hand, the presence of intermetallic phases Nb_7Ni_6 (μ) and Ni_3Nb (π) (140) can be observed in the Nb-Ni phase diagram, Figure 3-1-e. The solubility of Nb in FCC (Ni) is close to 10at% while that of Ni in β-(Nb) is approximately 4at%.

In the Cu-Nb system, Figure 3-1-f, no intermetallic phases are formed. Close to 3.5 at% Cu is dissolved in Nb at high temperatures and a peritectic reaction is observed. Equilibrium in temperatures lower than the peritectic at 1092°C is constituted by FCC (Cu) and BCC β-(Nb) with only small amounts of solid solutions atoms (157).

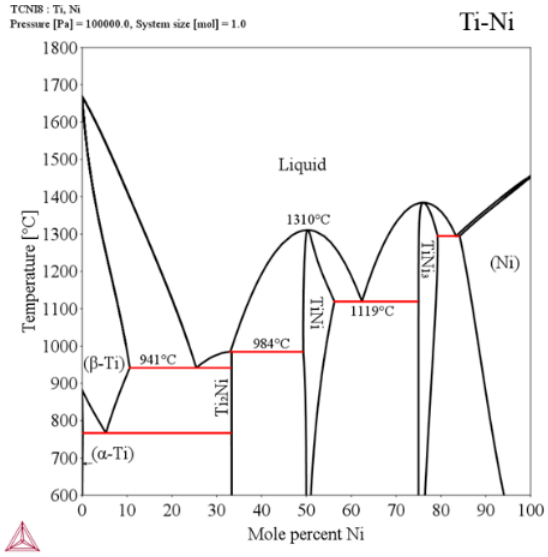
TCNI8 : Ti, Ni
Pressure [Pa] = 100000.0, System size [mol] = 1.0
Ti-Ni
Liquid
1310°C
1119°C
984°C
941°C
(β-Ti)
(α-Ti)
Ti2Ni
TiNi
TiNi3
(Ni)
Temperature [°C]
Mole percent Ni

(a)

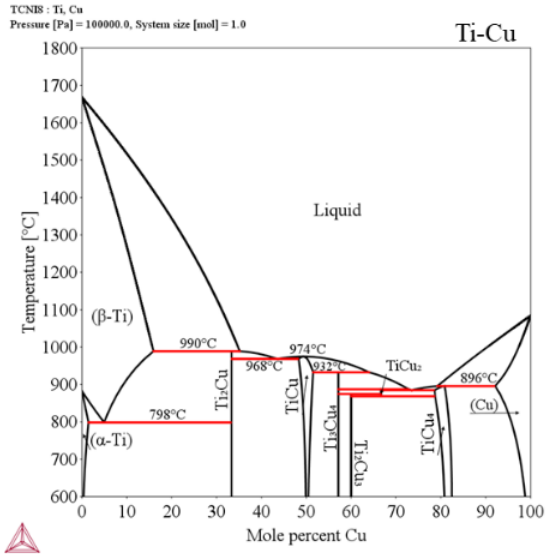
TCNI8 : Ti, Cu
Pressure [Pa] = 100000.0, System size [mol] = 1.0
Ti-Cu
Liquid
(β-Ti)
990°C
974°C
968°C
972°C
TiCu2
896°C
(Cu)
798°C
(α-Ti)
Ti2Cu
TiCu
Ti3Cu4
Ti2Cu3
TiCu4
Temperature [°C]
Mole percent Cu

(b)

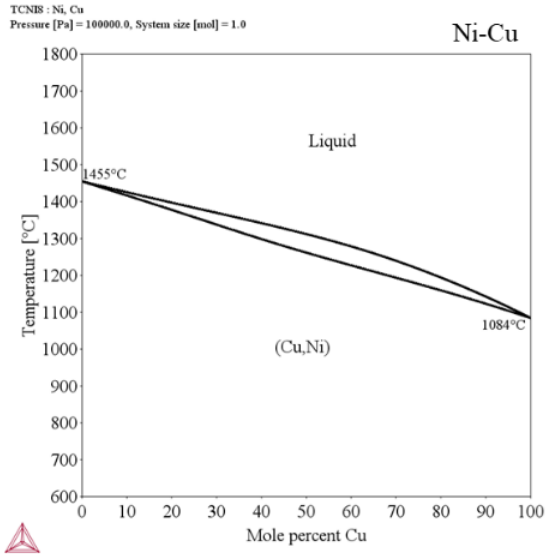
TCNI8 : Ni, Cu
Pressure [Pa] = 100000.0, System size [mol] = 1.0
Ni-Cu
Liquid
1455°C
1084°C
(Cu,Ni)
Temperature [°C]
Mole percent Cu

(c)

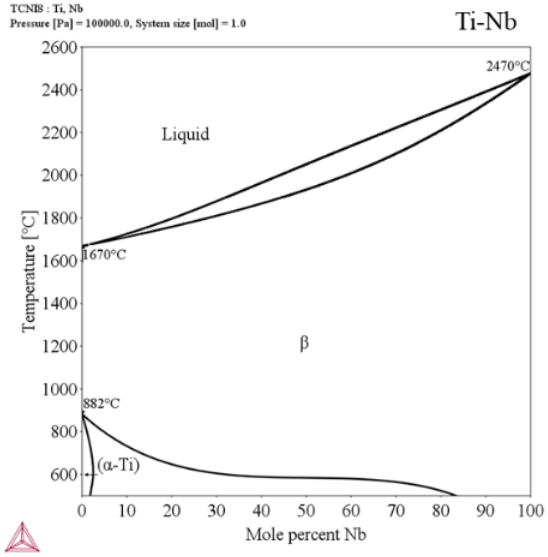
TCNI8 : Ti, Nb
Pressure [Pa] = 100000.0, System size [mol] = 1.0
Ti-Nb
2470°C
Liquid
1670°C
β
882°C
(α-Ti)
Temperature [°C]
Mole percent Nb

(d)

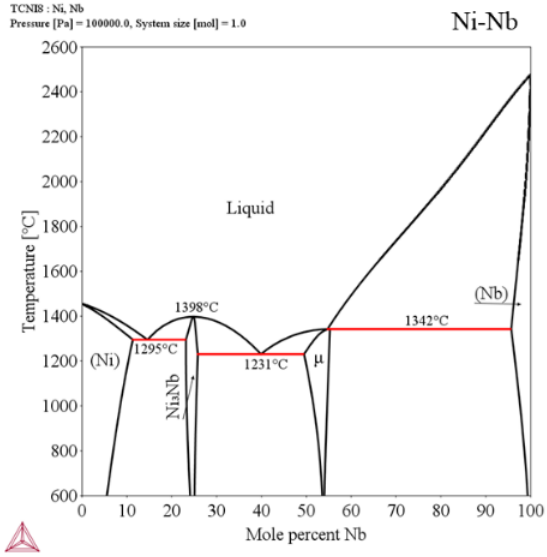
TCNI8 : Ni, Nb
Pressure [Pa] = 100000.0, System size [mol] = 1.0
Ni-Nb
Liquid
1398°C
1342°C
(Nb)
(Ni)
1295°C
1231°C
μ
Ni3Nb
Temperature [°C]
Mole percent Nb

(e)

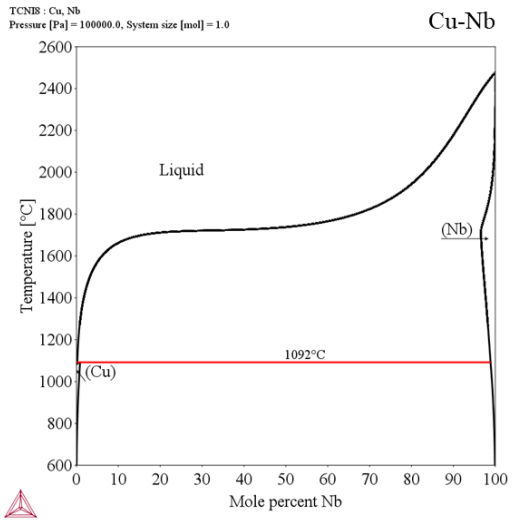

(f)

Figure 3-1 – (a) Ti-Ni, (b) Ti-Cu, (c) Ni-Cu, (d) Ti-Nb, (e) Ni-Nb, and (f) Cu-Nb binary phase diagrams

3.3.1.2. Ti-Ni-Cu analyses

Ternary phase diagrams in the Ti-Ni-Cu system for Cu contents smaller than 20at% are presented in Figure 3-2. The TiNi austenitic phase can be observed in the region of near 50at%Ti in the whole analyzed Cu-content range. With increasing temperature, this phase dissolves higher amounts of Ni and Cu. Excesses of Ti are also dissolved in TiNi at high temperatures, such as 1000°C (Figure 3-2 -c) and 1200°C (Figure 3-2-d), while at temperatures below 800°C (Figure 3-2- a and -b), it remains close to 50at%, presenting a behavior like that of binary Ti-Ni. In the Ti-rich region, Ti_2Ni is observed. In turn, Ni_3Ti and $(Cu,Ni)_2Ti$ are stable depending on the Cu content in the (Cu+Ni)-rich side. From the phase diagrams at higher temperatures, it can be noted that second phases present melting points lower than the TiNi matrix. At 1000°C, Ti_2Ni is no longer stable, and it is replaced by liquid.

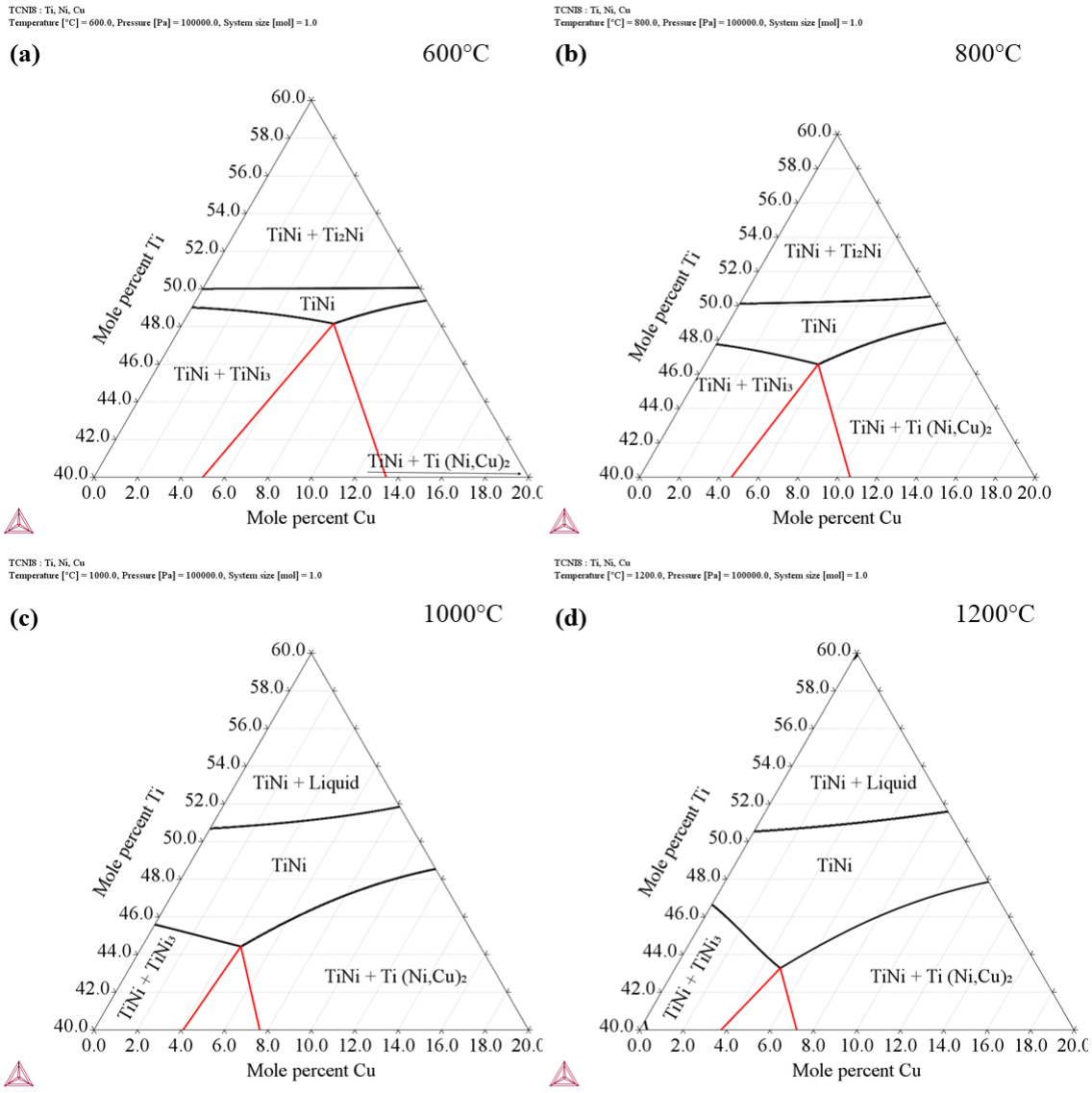

Figure 3-2 – Ti-Ni-Cu ternary phase diagrams at (a) 600°C, (b) 800°C, (c) 1000°C and (d) 1200°C

When Cu addition is considered in the Ti-Ni phase diagram, Figure 3-3, the intermetallic TiNi field shifts to decreasing Ni-contents. This occurs because Cu occupies Ni atomic sites. Comparing with the Ti-Ni binary, the stability region of the equiatomic phase increases, as greater excesses of Ti and Ni are supported. The stability region of Ti_2Ni is decreased while β-Ti is also stable in the Ti-rich region. In the region of excess of Ni, $TiNi_3$ is still the equilibrium second phase.

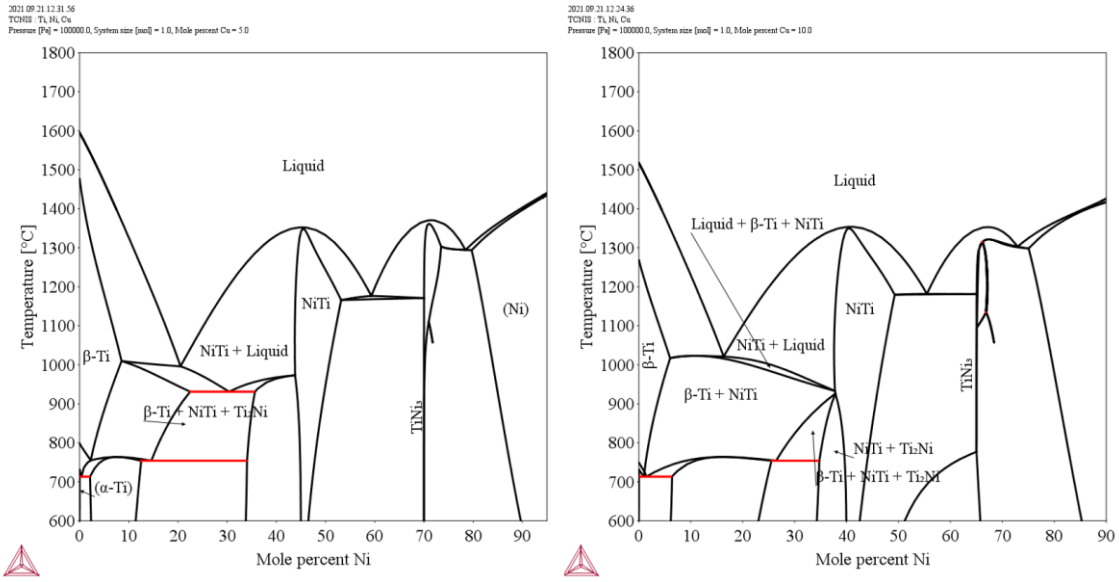

Figure 3-3 – Ti-Ni phase pseudobinary phase diagram with addition of (a) 5at% Cu and (b) 10at% Cu

Pseudobinary calculations considering Cu addition as a substitute for Ni are presented in Figure 3-4. Equilibrium phases are the same as previously observed in ternary calculations. In the Ni-rich base alloy with 48 at% Ti (Ti48), Figure 3-4-a, Ni_3Ti and $(Cu,Ni)_2Ti$ are observed in addition to the TiNi matrix. Ni_3Ti precipitates from TiNi at temperatures lower than 780 °C when the Cu addition is lower than 7 at%. $(Cu,Ni)_2Ti$ is formed from TiNi at intermediate Cu contents, and from the L + TiNi region at Cu contents higher than 14 at%. In the equiatomic $Ti_{50}Ni_{50}$, Figure 3-4-b, even amounts as high as 20 at% Cu can be dissolved into the TiNi matrix with no second-phase formation. In the Ti-rich alloys with 52 at% Ti (Ti52), Figure 3-4-c, the TiNi one-phase field is only observed at high temperatures for Cu contents higher than 8at%. In temperatures lower than 1000°C, Ti-rich precipitates are present under equilibrium. For Cu additions lower than 8at%, Ti_2Ni is formed from the TiNi + liquid region while in intermediate Cu contents, it precipitates from TiNi. At high Cu additions, β-Ti precipitation occurs at high temperatures and equilibrium shifts into α-Ti at low temperatures.

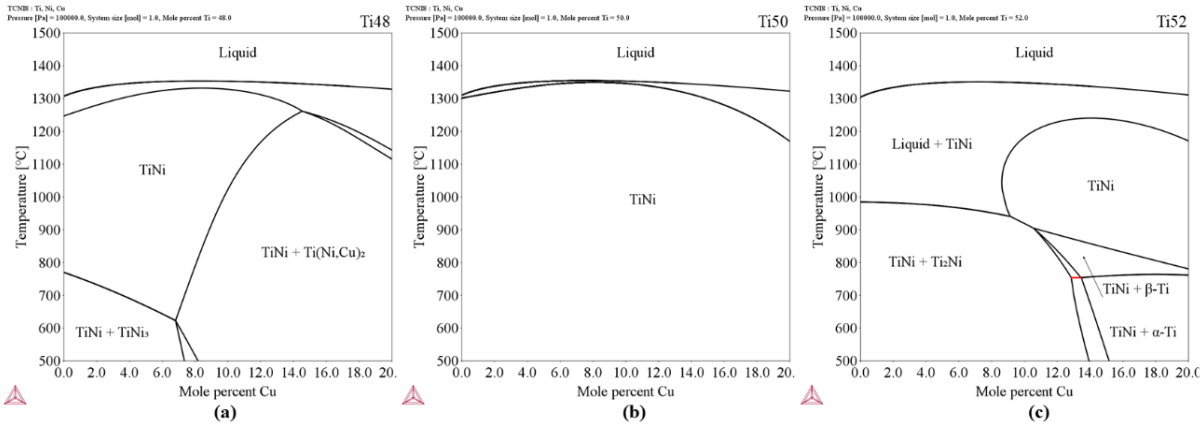

Figure 3-4 - Effect of addition of Cu as a substitute for Ni in alloys with fixed (a) 48 at% Ti, (b) 50 at% Ti and (c) 52 at% Ti.

3.3.1.3. Effect of Nb addition in the Ti-Ni phase diagram

Analyses of the Ti-Ni pseudobinary with fixed amounts of Nb are plotted in Figure 3-5. The addition of Nb increases the maximum solubility of Ti in the TiNi phase and this solubility's dependence with temperature. The formation of β-Nb occurs at low temperatures in the Ti-rich side. Besides Ti_2Ni, the β-phase can be formed at high temperatures, presenting varying amounts of Ti and Nb. In the Ni-rich side, $TiNi_3$ is still the equilibrium intermetallic compound. Additionally, $NbNi_3$ is stable for high Nb and Ni contents.

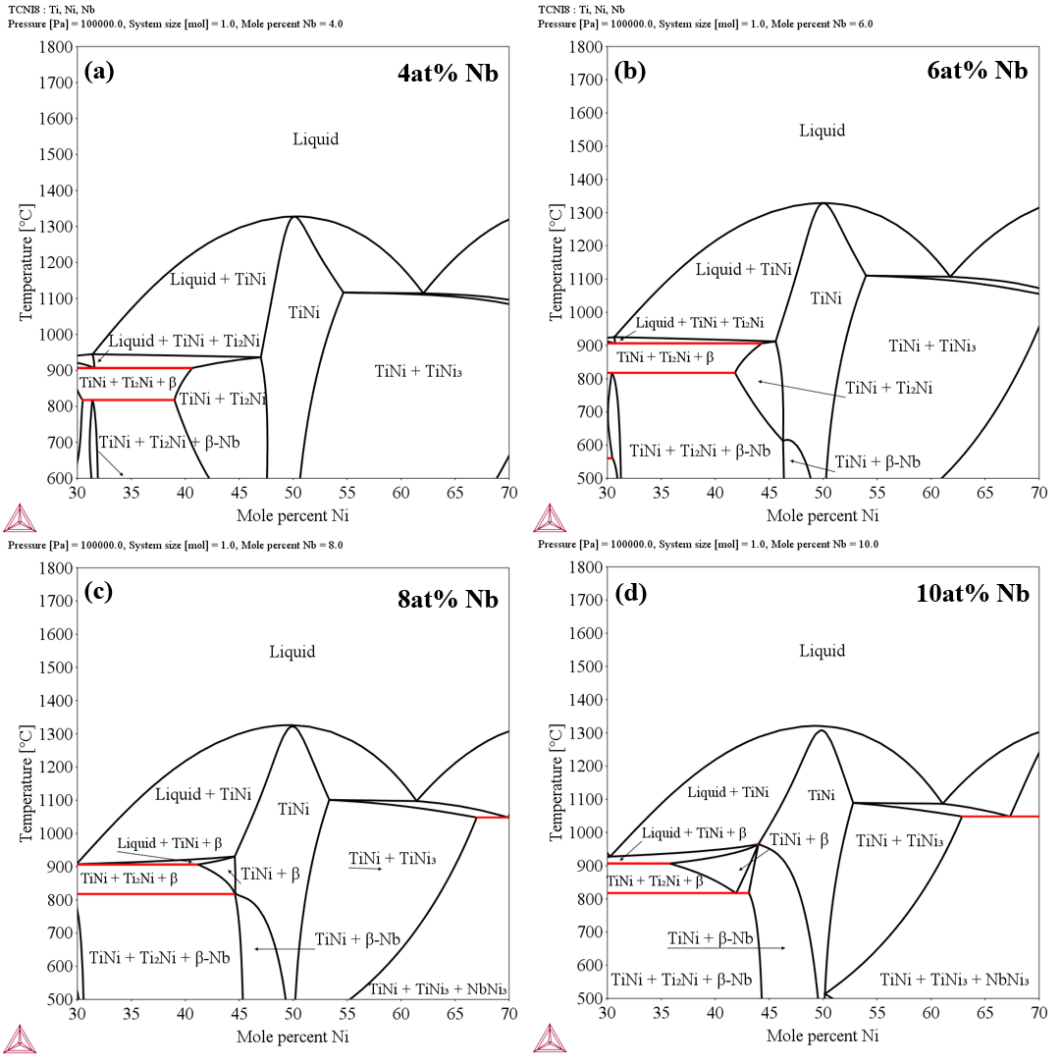

Figure 3-5 - Ti-Ni pseudobinary phase diagram with the addition of (a) 4 at% Nb, (b) 6 at% Nb, (c) 8 at% Nb and (d) 10 at% Nb.

3.3.1.4. Effect of Nb addition in substitution for Ni in TiNiCu

When Nb is added as a substitute for Ni in TiNiCu base alloys (Figure 3-6), the maximum solubility of this element in the TiNi matrix decreases with increasing Ti-content, going from ~10at% in $Ti_{48}Ni_{42-x}Cu_{10}Nb_x$ (Ti48Cu10) to ~6at% in $Ti_{50}Ni_{50-x}Cu_{10}Nb_x$ (Ti50Cu10), and less than 1at% in $Ti_{52}Ni_{48-x}Cu_{10}Nb_x$ (Ti52Cu10). Excesses of Nb precipitate with Ti as the β solid solution, identified as β-Ti/Nb. Thus, the TiNi one-phase field shrinks considerably with increasing Ti content of the base alloy due to the formation of Ti_2Ni and β-Ti/Nb second phases. Ti_2Ni is present in the low-Nb content region and β-Ti/Nb is formed from the liquid + TiNi field. Further cooling of alloys in these systems leads to the dissociation of β-Nb/Ti into Nb-

rich β-Nb and Ti-rich β-Ti phases. Additionally, a eutectoid decomposition of β-Ti/Nb into β-Nb and α-Ti can be observed at 550°C in Ti50Cu10 and Ti52Cu10.

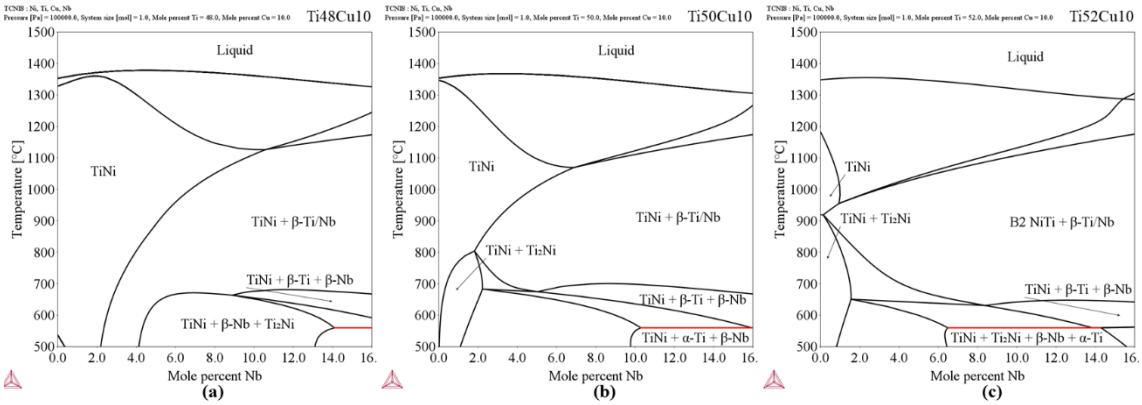

Figure 3-6 - Effect of Nb addition substitute for Ni in (a) $Ti_{48}Ni_{42-x}Cu_{10}Nb_x$, (b) $Ti_{50}Ni_{40-x}Cu_{10}Nb_x$ and (c) $Ti_{52}Ni_{48-x}Cu_{10}Nb_x$

3.3.1.5. Effect of Nb addition in substitution for Ti in TiNiCu

When Nb is added in place of Ti, Figure 3-7, a one-phase TiNi field is obtained at high temperatures within the whole analyzed Nb content range for all studied base-alloys. In $Ti_{48-x}Ni_{42}Cu_{10}$ (Ni42Cu10), precipitation of $(Cu,Ni)_2Ti$, with null Nb solubility, is expected with volume fractions lower than 5.2%. In $Ti_{50-x}Ni_{40}Cu_{10}Nb_x$ (Ni40Cu10), no second phases were observed and Nb atoms dissolve in the TiNi matrix, mainly occupying Ti's site. In $Ti_{52-x}Ni_{38}Cu_{10}Nb_x$ (Ni38Cu10), the precipitation of Ti-rich Ti_2Ni and β-Ti occurs when Nb contents are smaller than 3.2at% while β-Nb constituted by over 70% Nb is observed in alloys with Nb contents higher than 3.2at%.

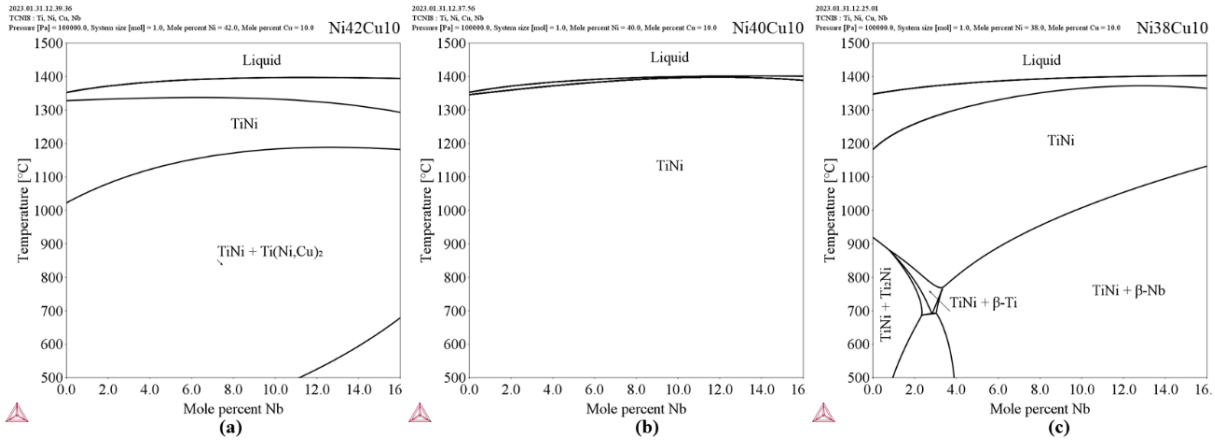

Figure 3-7 - Effect of Nb addition substitute for Ti in (a)$Ti_{48-x}Ni_{42}Cu_{10}Nb_x$, (b) $Ti_{50-x}Ni_{40}Cu_{10}Nb_x$, and (c) $Ti_{52-x}Ni_{38}Cu_{10}Nb_x$

The less complex diagrams obtained in this section can be related to the similarity of Nb and Ti observed in the binary calculations (Section 3.3.1.1), which seems to allow a greater fit when Nb is added in the place of Ti. Higher solubilities were achieved when compared to when this element is added as a substitute for Ni. Moreover, a wide region of small fractions of β-Nb in a TiNi matrix can be achieved in the Ti-rich base-alloy.

3.3.1.6. Effect of Nb addition in $(TiNiCu)_{100-x}Nb_x$ in TiNiCu

Pseudobinaries obtained by adding Nb while maintaining the Ti:Ni:Cu proportions are presented in Figure 3-8. TiNi matrix and β-Nb second-phase are the main phases in the (Ni+Cu)-rich and equiatomic equivalent base alloys whereas increasing Ti favors the stability of Ti_2Ni. A eutectic reaction from the liquid + TiNi field can be observed, leading to the formation of TiNi and β-Nb. The Nb content in the eutectic decreases slightly with increasing Ti, as the one-phase TiNi field shrinks.

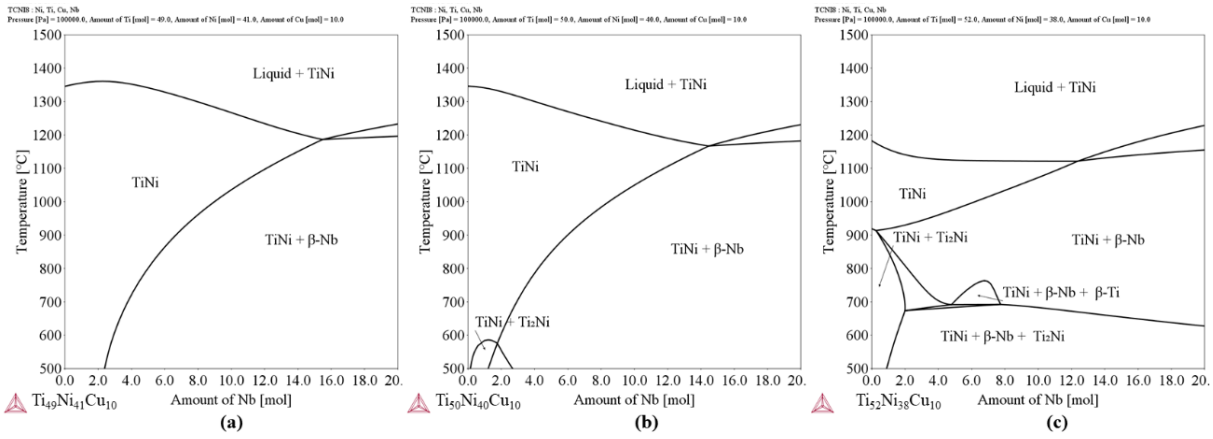

Figure 3-8 – Effect of Nb addition substitute for Ni in $(Ti_{48}Ni_{42}Cu_{10})_{100-x}Nb_x$, $(Ti_{50}Ni_{40}Cu_{10})_{100-x}Nb_x$ and $(Ti_{52}Ni_{38}Cu_{10})_{100-x}Nb_x$

In summary, it has been noted from the CALPHAD analyses that Ni and Cu form an isomorphous system whereas Ti and Nb dissolve each other completely at high temperatures. Both Cu and Nb increase the stability region of the TiNi austenitic phase in pseudobinary calculations of the Ti-Ni phase diagram. The addition of Cu shifts the TiNi intermetallic composition because this solute atom is dissolved in Ni's atomic sites.

The Cu content was fixed at 10at% in the place of Ni for further analyses of the Ti-Ni-Cu-Nb system. When Nb is added as a substitute for Ni, the solubility of Nb on TiNi decreases drastically with increasing Ti content, leading to the precipitation of β-Nb/Ti, α-Ti and Ti_2Ni. The TiNi one-phase field is limited to small Nb additions and high temperatures. β-Nb appears when β-Nb/Ti dissociates into a Ti-rich and a Nb-rich phase. When Nb is added instead of Ti, the high solubility of Nb can be highlighted and a one phase TiNi field occurs at high temperatures. The formation of β-Nb occurs in the Ti-rich base alloy. In the equiatomic equivalent, no second phases are present, while $Ti(Ni,Cu)_2$ is observed in the (Ni+Cu)-rich. When Nb is added while maintaining Ni:Ti:Cu proportions, the TiNi phase field shrinks with increasing Ti content and β-Nb, Ti_2Ni, and β-Ti second phases were observed.

Because of the similarities of Ti and Nb elements and the potential in obtaining alloys constituted by high amounts of TiNi and precipitation of β-Nb phase, the $Ti_{52-x}Ni_{38}Cu_{10}Nb_x$ system, Figure 3-7-c, was selected for further evaluation.

3.3.2. Literature background data analysis

3.3.2.1. Summary of reported experimental results.

A summary of reported properties of Ti-Ni-Cu-Nb alloys is listed in Table 3.1, where σ_{Ms} is the stress to induce the MT, ΔT is the thermal hysteresis and Af is the austenitic finishing temperature. None of these quaternary alloys is completely characterized by an elastocaloric cooling perspective, and ΔHt and ΔTad have not yet been assessed.

Table 3.1- Properties of Ti-Ni-Cu-Nb alloys obtained from a - Jiang et al., 2015 (135)**; b -** Wang et al., 2016 (136)**; c -** Liu et al., 2018 (137)**; d -** Tong et al., 2019 (131)

Alloy Composition	σ_{Ms}	ΔT	Af	Ref
$(Ti_{50}Ni_{38}Cu_{12})_{93}Nb_7$	350 MPa		30°C	a
	50 MPa		37°C	a
	150 MPa		30°C	a
	320 MPa		22°C	a
$Ti_{50}Ni_{40}Cu_{10}$		9°C	80°C	b
$(Ti_{50}Ni_{40}Cu_{10})_{95}Nb_5$	200 MPa	13°C	22°C	b
$(Ti_{50}Ni_{40}Cu_{10})_{90}Nb_{10}$	240 MPa	14°C	-10°C	b
$(Ti_{50}Ni_{40}Cu_{10})_{85}Nb_{15}$	340 MPa	20°C	-30°C	b
$Ti_{50}Ni_{38}Cu_{12}$			70°C	c
$(Ti_{50}Ni_{38}Cu_{12})_{95}Nb_5$			20°C	c
$(Ti_{50}Ni_{38}Cu_{12})_{90}Nb_{10}$			-5°C	c
$(Ti_{50}Ni_{38}Cu_{12})_{85}Nb_{15}$			-30°C	c
$(Ti_{54}Ni_{34}Cu_{12})_{90}Nb_{10}$		11.5°	57°C	d

3.3.2.2. Effect of Nb on the transformation temperatures

In order to evaluate how the MT critical temperatures vary with the alloy's chemical composition, the Afs highlighted in Table 3.1 were plotted against the chemical compositions of the respective alloys. Based on the atomic site occupation and the binary phase diagrams obtained in thermodynamic analysis (Section 3.3), (Ni+Cu) and (Ti+Nb) contents were considered. Within the analyzed alloys, two contrary tendencies can be observed in Figure 3-9. Af increased in the first half while it decreased in the second half of the curve with increasing (Ni+Cu) content and decreasing (Ti+Nb) content. The manufacturing route and performed heat-treatments were not considered in this analysis. In this manner, it can be inferred that a range of Af can be obtained in a certain alloy composition depending on the thermomechanical processing.

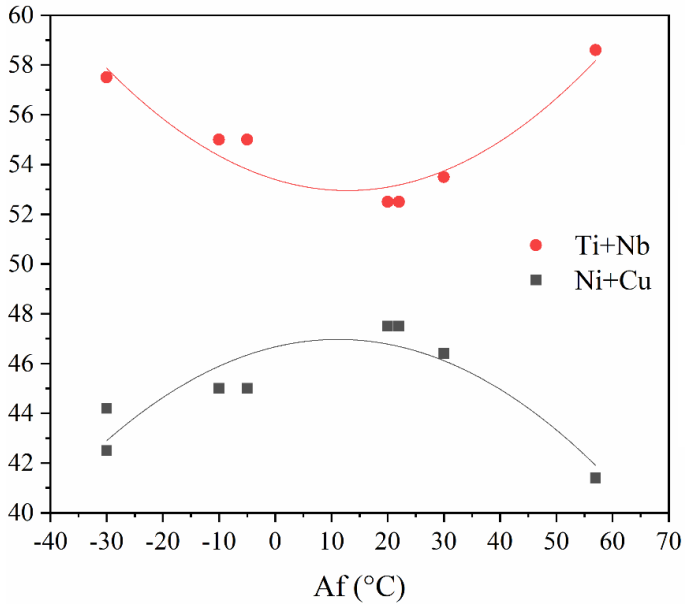

Figure 3-9 – Austenitic finishing temperature Af as a function of the alloy's chemical composition

The $(Ti_{54}Ni_{34}Cu_{12})_{90}Nb_{10}$ alloy (131,132), which exhibited excellent thermal stability presented an Af too high for cooling applications at room temperature (57°C). However, the tendency of decreasing Af with the addition of Nb is observed both on $(Ti_{50}Ni_{40}Cu_{10})_{100-x}Nb_x$ (136) and $(Ti_{50}Ni_{38}Cu_{12})_{100-x}Nb_x$ (137), where low Af temperatures were obtained. In binary TiNi alloys, the transformation temperatures are strongly affected by the chemical composition of the TiNi

phase in the region of excesses of Ni (10). In ternary TiNiNb alloys, it has been discussed that both Ni/Ti ratio and Nb content alters the valence electron concentrations (c_v), affecting Ms (162,163). Thus, the Afs obtained for $(Ti_{50}Ni_{40}Cu_{10})_{100-x}Nb_x$ and $(Ti_{50}Ni_{38}Cu_{12})_{100-x}Nb_x$ alloys were plotted against calculated Ni/Ti ratio and maximum Nb content in TiNi in alloys with varying Nb contents (Figure 3-10). The decrease in Af could be related to enrichments of both Ni and Nb in the TiNi matrix.

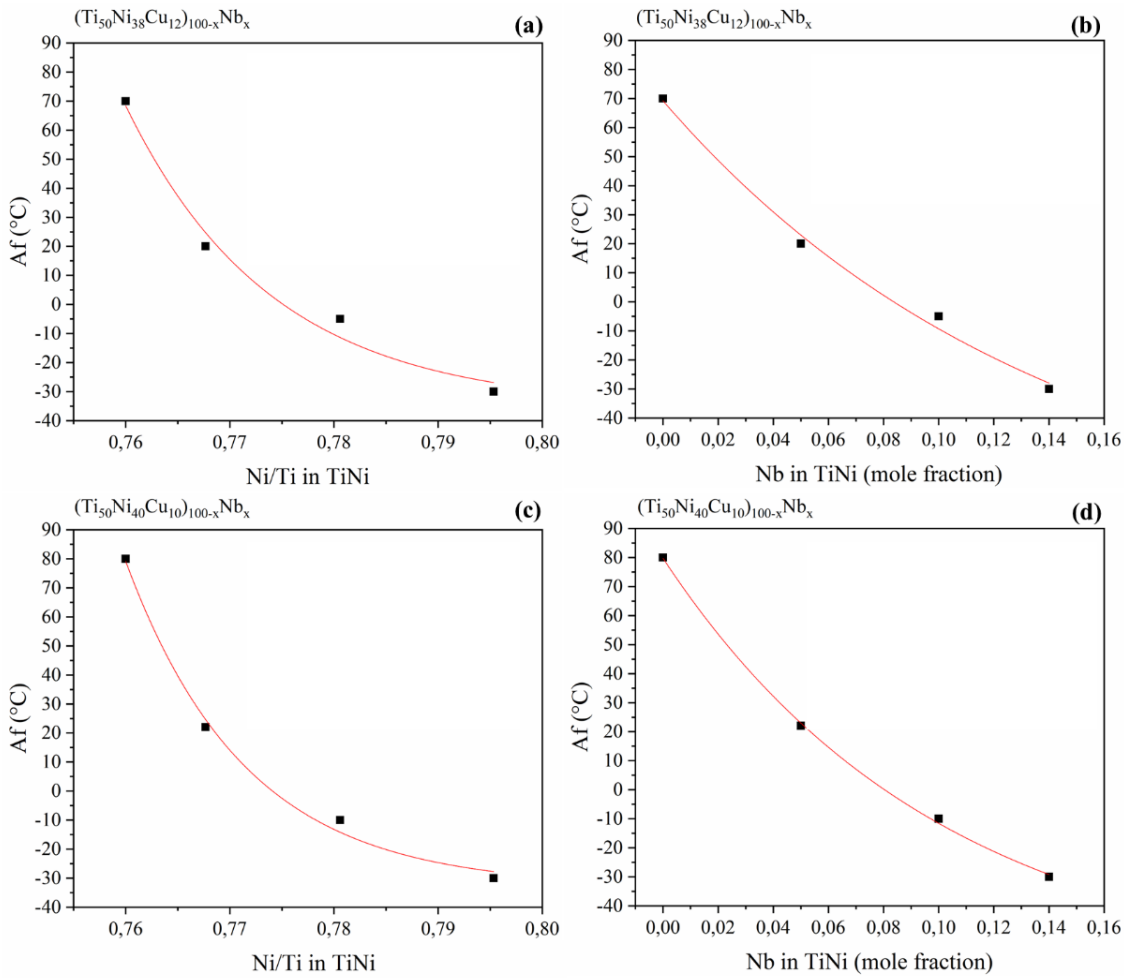

Figure 3-10 – Austenitic finishing temperature Af as a function of (a,c) Ni/Ti ratio and (b,d) Nb solubility in (a,b) $(Ti_{50}Ni_{38}Cu_{12})_{100-x}Nb_x$ and (c,d) $(Ti_{50}Ni_{40}Cu_{10})_{100-x}Nb_x$ alloys

3.3.2.3. Effect of heat-treatments

Results reported by Jiang et al., 2015 (135) in $(Ti_{50}Ni_{38}Cu_{12})_{93}Nb_7$ with different heat-treatments indicate that this tool can be used for transformation temperature adjustment. The as-cast alloy is constituted by TiNi, β-Nb, and $Ti_2(Ni,Cu)$. However, no information was provided on the microstructure in the heat-treated conditions. From the calculated cooling diagram, Figure 3-11-a, besides TiNi and β-Nb, $(Ti,Nb)_3Ni$ is a stable phase. $Ti_2(Ni,Cu)$ may have formed instead due to precipitation kinetics. Neither of the Ti-rich phases are stable at the performed heat-treatment temperatures of 400°C, 500°C, 600°C, 700°C and 800°C, where a two-phase TiNi + β-Nb equilibrium occurs.

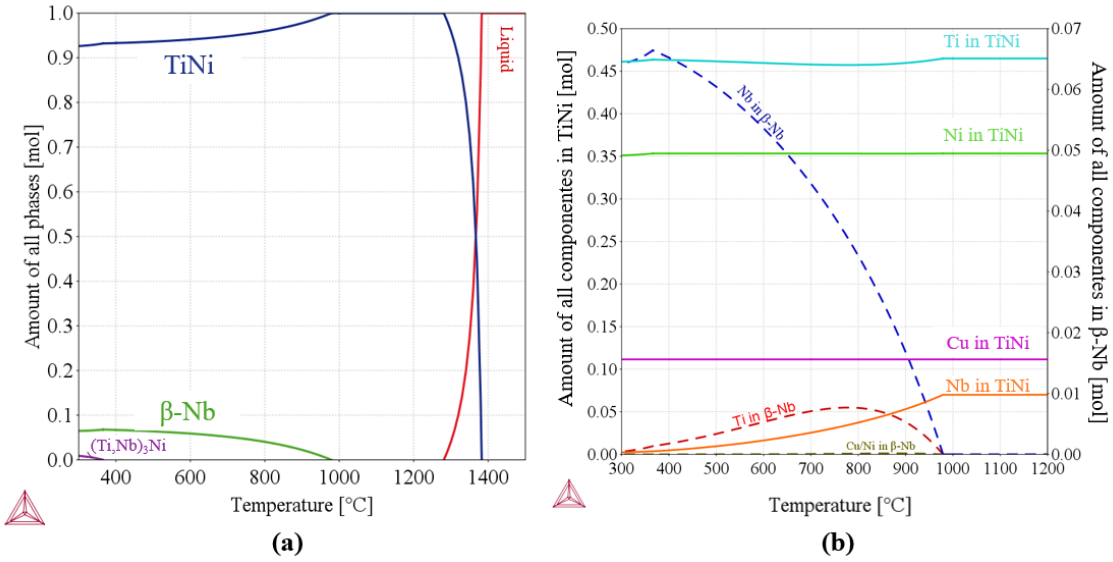

Figure 3-11 – (a) Solidification curve and (b) amount of Ti, Ni, Cu and Nb in TiNi and β-Nb phases in $(Ti_{50}Ni_{38}Cu_{12})_{93}Nb_7$

The element contents in TiNi and β-Nb phases are presented in Figure 3-11-b. Near-null Cu and Ni are dissolved in β-Nb. In turn, the solubility of Ti can be as high as 25%, when ~0.01 mol of Ti precipitates with ~0.04 mol of Nb. The depletion of Ti from the matrix with the precipitation of β-Nb can be associated with enrichments of Ni in the TiNi matrix. Because the Ti solubility in β-Nb changes with temperature, there is a possibility that variations on the Ni:Ti ratio in the matrix occur after different heat-treatments, which can be associated with varying

Afs. In binary TiNi with excesses of Ni, the formation of Ti_3Ni_4 in low-temperature heat-treatments leads to decreasing Ni content in the TiNi matrix and is accompanied by increasing Afs (1,10). Contrarily, when Ti is dissolved in β-Nb while Ni is not, the Ni fraction in TiNi increases, and lower Afs can be achieved.

The effect of Nb content in TiNi in varying temperatures on Af was also considered. For that, the solubility of Nb in TiNi at different heat-treatment temperatures was calculated and related with Afs measured by Jiang *et al* (135), as plotted in Figure 3-12. The increasing direction of equilibrium temperature is indicated by an arrow. At lower temperatures, lower Nb solubilities are observed, thus leading to higher volume fractions of β-Nb, in accordance with Figure 3-11-a. In Figure 3-12, two regions with distinct behaviors can be identified regarding the variation of Af. The first (I) refers to heat-treatments at 400°C and 500°C. The second (II), to temperatures of 600°C and higher. In region II, Af decreases with increasing heat-treatment temperature, where higher Nb solubility occurs. In region I, the inverse tendency is observed.

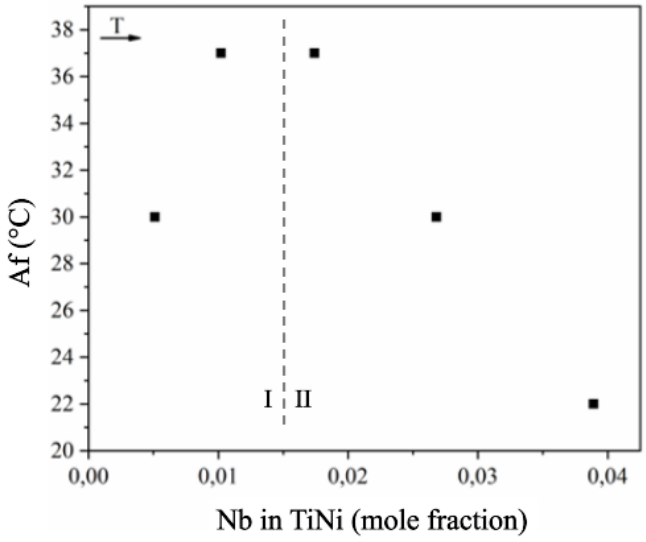

Figure 3-12 – Effect of (a) Nb dissolved in TiNi on Af of $(Ti_{50}Ni_{38}Cu_{12})_{93}Nb_7$ alloy after heat-treatment at various temperatures

Besides Nb solubility in the TiNi matrix, the kinetics of precipitation of β-Nb may also affect the amount of dissolved Nb after different heat-treatments. These two contributions are reversibly dependent on temperature, as the precipitation of β-Nb is dependent on diffusion

mechanisms. While it appears, from region II, that higher fractions of Nb in the matrix phase leads to lower Afs, the kinetic factor may be predominant at lower temperatures, resulting in relevant deviations from equilibrium and the inverse tendency on Af. Therefore, there is an indication that the presence of Nb as a solute atom in the TiNi lattice, either due to higher solubility at higher temperatures or by solute trapping at lower temperatures, results in decreasing Af.

3.3.3. Evaluation of $Ti_{52-x}Ni_{38}Cu_{10}Nb_x$ alloys by the CALPHAD method

In section 3.3, $Ti_{52-x}Ni_{38}Cu_{10}Nb_x$ was selected as a promising system to achieve alloys presenting a TiNi matrix with the possibility of precipitation of β-Nb under equilibrium. In section 3.3.2, the effect of Nb content in Af could be related with the chemical composition of the alloy and the TiNi phase. The effect of heat-treatment was associated with variations on the Ti dissolved in β-Nb and Nb dissolved in TiNi, both resulting in chemical compositions alterations in the austenitic phase. In the present assessment, additions of 4, 6, 8 and 10 at% Nb were evaluated in the selected $Ti_{52-x}Ni_{38}Cu_{10}Nb_x$ system based on interactions obtained between literature results and calculable thermodynamic quantities.

Ti-Ni-10at%Cu phase diagrams with different Nb contents are presented in Figure 3-13-a. At temperatures higher than 800°C, stable solid phases in the Ti-rich region are TiNi and β-Nb. The maximum solubility of Ti in TiNi increases with increasing Nb content whereas the formation of β-Nb occurs for higher temperatures and increasing Ni-content. The precipitation temperature of β-Nb as a function of Nb-content in $Ti_{52-x}Ni_{38}Cu_{10}Nb_x$ can be seen in Figure 3-13-b. The volume fraction of β-Nb of different alloys is plotted as a function of temperature in Figure 3-13-c. For Nb contents higher than 3at%, the formation of β-Nb is favored with increasing Nb, as it precipitates at higher temperatures. Up to 5 vol% of β-Nb can be obtained and increasing Nb content leads to higher fractions of this phase at a fixed temperature. These results indicate that volume fractions higher than 95% of TiNi can be obtained with the precipitation of small amounts of β-Nb.

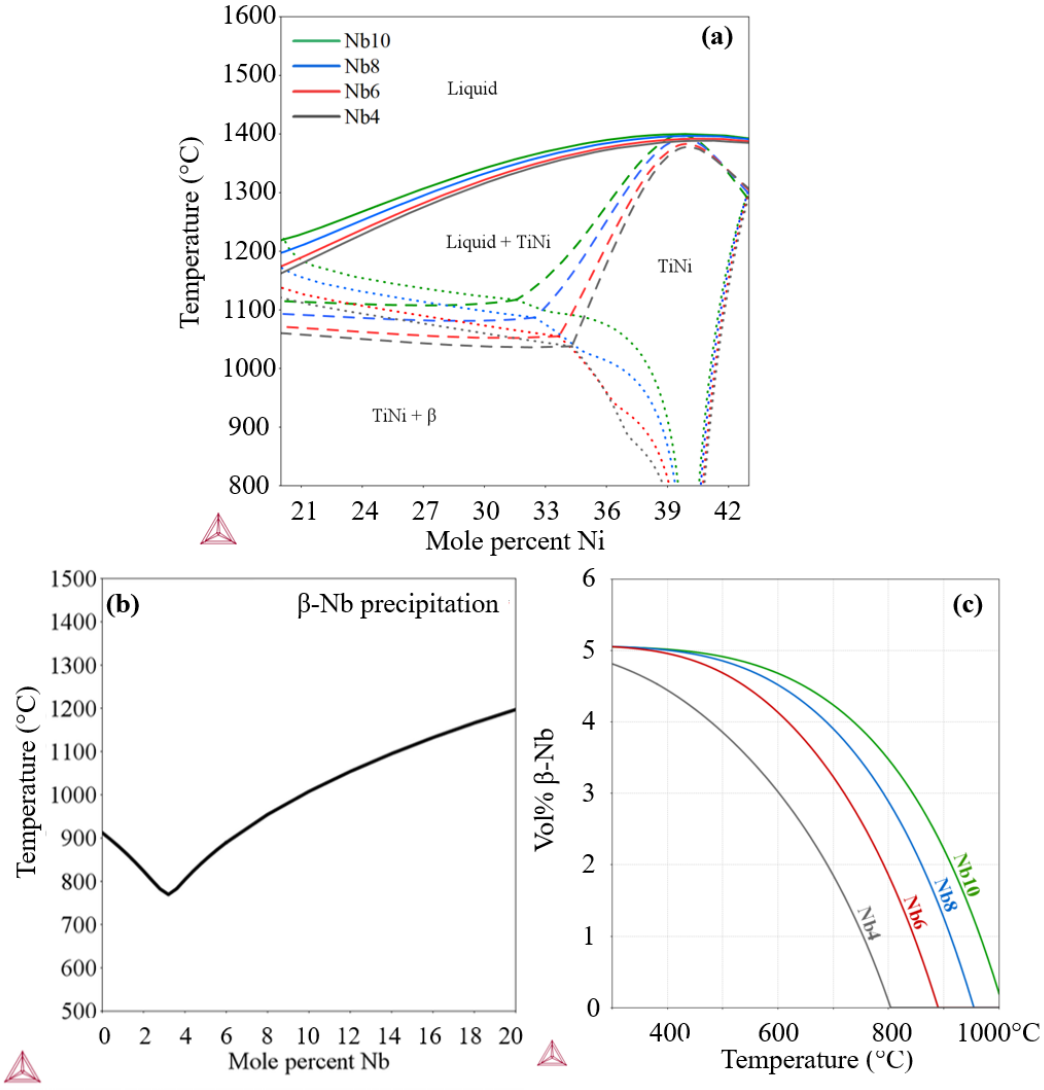

Figure 3-13 – (a) Ti-Ni pseudobinaries with fixed 10at%Cu and varying Nb contents, and (b) β-Nb precipitation temperature as a function of Nb content in $Ti_{52-x}Ni_{38}Cu_{10}Nb_x$

Regarding forming processes, hot working should be favored in alloys with lower Nb contents within the analyzed ones. This is because it will be possible to produce deformation in a one-phase region with no need of excessive heating. In turn, cold-working should be favored in alloys with higher Nb contents due to higher fractions of β-Nb.

The change on Ti's solubility in β-Nb and Nb's in TiNi at varying temperatures were adopted to evaluate the potential use of heat-treatments to adjust Af. As it can be noted in Figure 3-14-a, the amount of Ti dissolved in β-Nb depends on the temperature in all the analyzed alloys, with maximum Ti solubility higher with decreasing alloy's Nb-content. Nb solubility in TiNi

also varies with temperature, Figure 3-14-b, and higher values are achieved in the alloy with the highest Nb content. The Nb content in TiNi tends to stabilization close to the low temperature range. Hence, the differences in the solubility of Ti in β-Nb and of Nb in TiNi with temperature suggest that these are heat-treatable alloys.

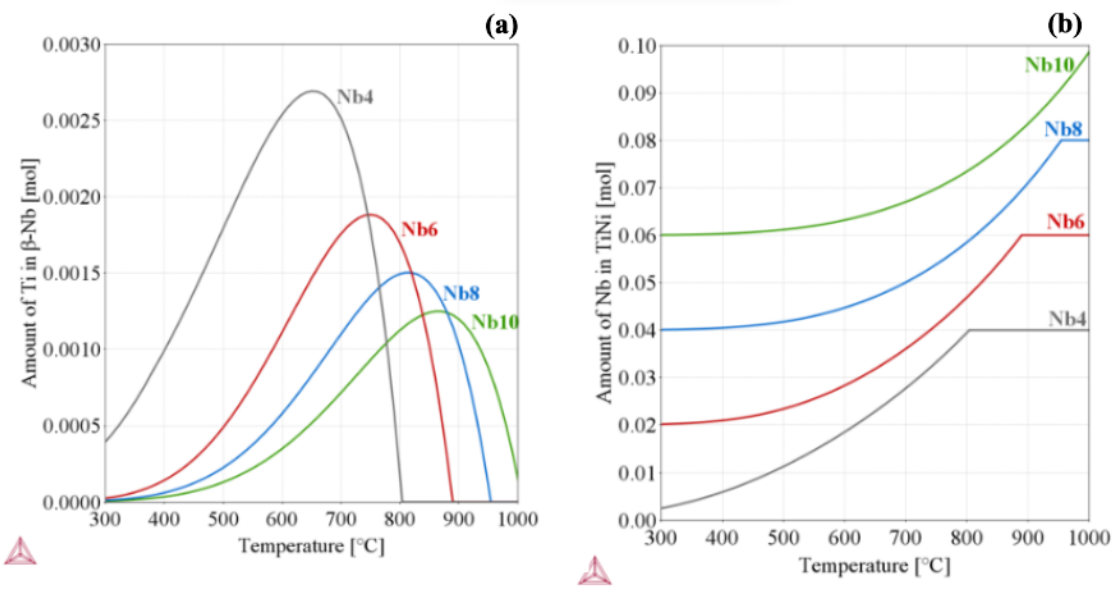

Figure 3-14 – (a) Ti solubility in β-Nb and (b) Nb solubility in TiNi as a function of temperature in $Ti_{52-x}Ni_{38}Cu_{10}Nb_x$, x = 4,6, 8 and 10at% alloys

The (Ni+Cu)/(Ti+Nb) ratio of the alloy's chemical composition was plotted against Afs to approximate achievable Afs. A linear fit with $R^2 > 0.96$ was calculated in the range of Afs lower than room temperature. Because the studyied alloys present a Ti+Nb constant equal to 52at% ((Ni+Cu)/(Ti+Nb) = 0.92), Afs close to 25°C can be achieved: 27°C is calculated using mean coeffient values.

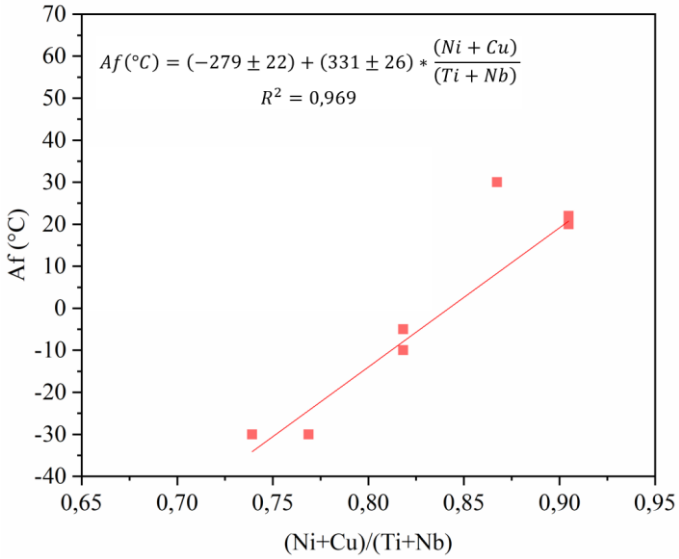

Figure 3-15 - Linear fit of Afs obtained from literature results as a function of (Ni+Cu)/(Ti+Nb) ratio of the alloy composition.

3.4. Conclusions

In this chapter, CALPHAD method was used to perform a thermodynamic analysis of the Ti-Ni-Cu-Nb system, aiming to obtain TiNiCuNb shape memory alloys that are potentially formable, heat-treatable alloys presenting high cycling stability and superelasticity at room temperature. In calculations using various approaches, TiNi, β-Nb/Ti, β-Nb, β-Ti, α-Ti, Ti_2Ni and $Ti(Ni,Cu)_2$ phases were observed. Because of the similarities between Ti and Nb and the potential in obtaining alloys constituted by a TiNi matrix with β-Nb precipitation, the $Ti_{52-x}Ni_{38}Cu_{10}Nb_x$ system was selected. By relating results reported in the literature with calculable thermodynamic quantities, decreases in Af with increasing alloy's Nb content could be related both to enrichments of Ni and Nb in TiNi. The effect of heat treatment was associated with varying amounts of Ti dissolved in β-Nb and Nb in TiNi at different temperatures.

$Ti_{52-x}Ni_{38}Cu_{10}Nb_x$, alloys with 4, 6, 8 and 10 at% Nb were evaluated. These alloys presented high fractions of TiNi with up to 5 vol% β-Nb under equilibrium. While the TiNi phase is essential for the alloy's functional behavior and for obtaining relatively high transformation enthalpies, the formation of β-Nb is expected to result in improvements in the cold-formability. Variations of Ti solubility in β-Nb and of Nb in TiNi were observed in equilibrium calculations,

indicating that heat-treatments may be effective in altering martensitic transformation temperatures.

4. ROLE OF Nb ON THE PHASE STABILITY AND MORPHOLOGY OF Ti-Ni-Cu-Nb ALLOYS

4.1. Introduction

Based on the binary phase diagram analysis [17–24], the isomorphous Ti-Nb interactions at high temperatures [21], and the thermodynamic evaluations performed in Chapter 3, quaternary alloys were produced by adding Nb as a substitute for Ti in the $Ti_{52}Ni_{38}Cu_{10}$ base alloy. In this study, alloys previously selected, 3.3.3, were cast and evaluated. The aim is to understand the role of Nb in the phase stability of Ti-Ni-Cu-Nb alloys through thermodynamic calculations and microstructural analyses.

4.2. Experimental Procedure

$Ti_{52-x}Ni_{38}Cu_{10}Nb_x$ alloys were synthesized with Nb additions of x = 4, 6, and 10 at%, hereafter referred as Nb4, Nb6, and Nb10, respectively. Thermodynamic simulations using ThermoCalc (2018b) software were used to predict the equilibrium microstructures using the TCNI8 (v8.1) database.

Melting was performed from elemental constituents (> 99.5% purity) into 30 g ingots in an arc-melting furnace. This procedure was performed under an argon-controlled atmosphere in a water-cooled copper mold. Each ingot was remelted at least six times to ensure chemical homogeneity, being turned over after each melting/solidification step. A new Nb10 sample was cast and homogenized for 24 h at 900 °C to achieve close-to-equilibrium conditions in the alloy with the highest Nb content. Slow cooling took place inside of the furnace.

Samples from the as-cast and homogenized alloys were cut, mounted, ground, and mechanically polished for microstructural evaluation through scanning electron microscopy (SEM)/energy-dispersive X-ray spectroscopy (EDS) (FEI Inspect S50) with backscattered electrons. X-ray diffraction (XRD) was used for phase identification in a PANalytical Empyrean diffractometer with Cu K-α radiation, with 2θ ranging from 30 to 110°, at a scan speed of 0.02°/s. Materials Project database was used for peak indexation based on the phases reported in previous studies [12–15,25–27]. The relative integrated peak areas were used to qualitatively compare the phase fractions of the different alloys.

Differential scanning calorimetry (DSC; Shimadzu - DSC60) was used to assess the reversible martensitic transformation of the as-cast alloy. The specimens were cooled to -100 °C and subsequently heated at 20 °C/min to 100 ° C. Cooling to -100 °C occurred at the same rate as the heating. This heating/cooling cycle was repeated five times to acquire information on thermal cycling stability.

4.3. Results

4.3.1. Equilibrium calculations

The $Ti_{52-x}Ni_{38}Cu_{10}Nb_x$ system was initially assessed using its pseudobinary phase diagram, as shown in Figure 4-1-a. The volume fractions of the equilibrium phases as a function of temperature in the selected alloys, marked in Figure 4-1-a, were obtained using the equilibrium calculator and are illustrated in Figure 4-1-b. Nb4 is represented by red lines, Nb6 by blue lines, and Nb10 by green lines. The different dashed lines represent the different phases illustrated in Figure 4-1-b. Under these conditions, all cast alloys should solidify as pure TiNi, and as much as 5vol% of β-Nb could precipitate during slow cooling.

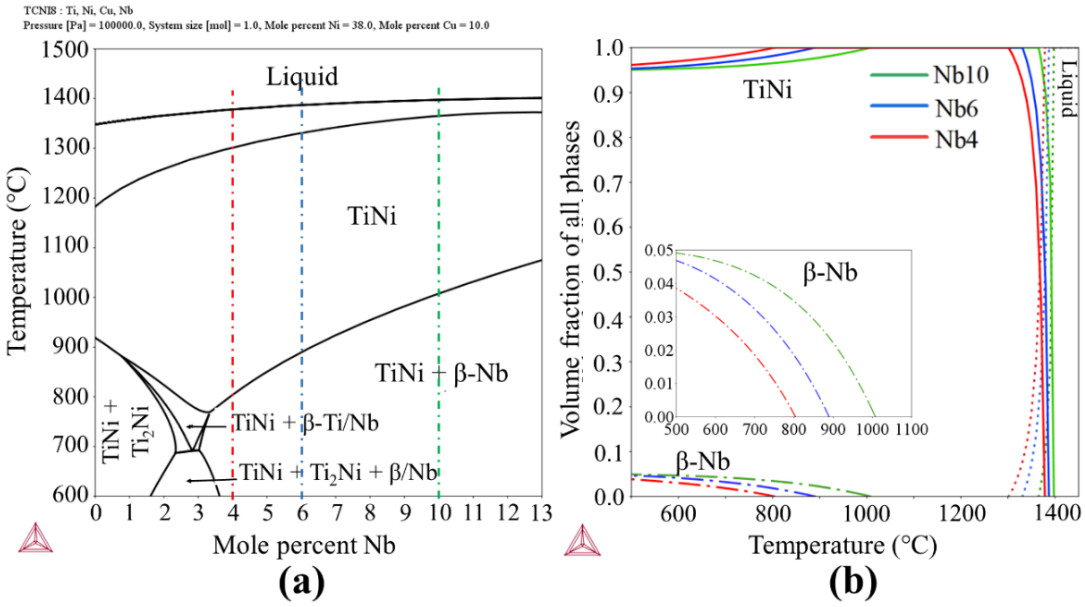

Figure 4-1 - (a) $Ti_{52-x}Ni_{38}Cu_{10}Nb_x$ pseudobinary phase diagram and (b) volume fractions of stable phases with varying temperatures under equilibrium conditions for x = 4, 6, 8, and 10at%.

4.3.2. Microstructural evaluation and phase identification in the as-cast alloys

The XRD spectra of the as-cast alloys are illustrated in Figure 4-2. The B2 type TiNi (MP #571) austenitic phase was identified, whereas β-Nb (MP #75) and Ti_2Ni (MP #1808) peaks were present in all compositions.

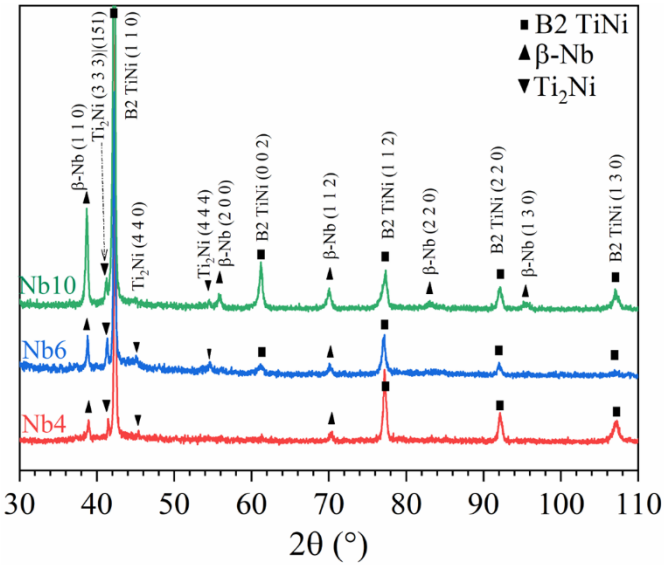

Figure 4-2 - XRD spectra of the as-cast alloys.

Backscattered electron images of the as-cast samples obtained using SEM are shown in Figure 4-3. EDS analysis, Table 4.1, was used to identify the phases based on the XRD results. The grey matrix phase, indexed as number 1, was identified as the TiNi phase. The white phase, number 2, is an Nb-rich phase identified as β-Nb in the XRD spectra. The dark gray phase, number 3, was identified as the Ti_2Ni intermetallic. Additionally, the black particles, number 4, exhibited over 90at% Ti, suggesting that it is metallic Ti.

Table 4.1. Mean element contents measured on the EDS semi-quantitative analysis of different phases in Nb4, Nb6, Nb8, and Nb10 as-cast alloys. Values are in atomic percent.

		Ti (at%)	Ni (at%)	Cu (at%)	Nb (at%)
TiNi	**Nb4**	46.5 ± 0.3	41.7 ± 0.8	9.0 ± 0.9	2.7 ± 0.1
	Nb6	45.0 ± 0.6	41.2 ± 1.6	9.8 ± 1.6	3.7 ± 0.5
	Nb10	44.3 ± 0.5	42.9 ± 0.6	8.1 ± 0.5	4.6 ± 0.3
b-Nb	**Nb4**	34.8 ± 2.0	9.0 ± 4.3	4.5 ± 1.4	51.7 ± 6.6
	Nb6	22.7 ± 2.0	7.1 ± 2.0	3.8 ± 0.8	64.7 ± 6.6
	Nb10	23.1 ± 2.7	10.3 ± 1.9	5.1 ± 1.0	61.5 ± 5.5
Ti_2Ni	**Nb4**	62.3 ± 0.2	30.2 ± 0.6	3.7 ± 0.1	3.8 ± 0.3
	Nb6	56.4 ± 1.9	30.8 ± 0.7	4.6 ± 0.6	8.2 ± 1.9
	Nb10	52.8 ± 1.2	31.0 ± 0.1	6.0 ± 0.7	10.2 ± 0.9
Ti	**Nb10**	90.1 ± 2.7	3.4 ± 1.8	1.4 ± 0.5	5 ± 0.6

β-Nb was mainly observed in a lamellar eutectic constituent with the TiNi phase. Its volume fraction, obtained by dividing the integrated peak areas of this phase by the sum of all the integrated peak areas in the XRD pattern, increased with increasing Nb content:15, 23, and 31% were observed in Nb4, Nb6, and Nb10 alloys, respectively. Ti_2Ni exhibited different morphologies and distributions as a function of the alloy composition. In Nb4, a dendritic-like morphology was observed. In Nb6, prismatic precipitates were observed within the matrix phase and associated with the β-Nb phase and the eutectic structure. In Nb10, the Ti_2Ni precipitates were mainly intercalated with the β-Nb/TiNi eutectic constituent. Metallic Ti was

not observed in Nb4; however, it was noteworthy in the Nb10 alloy, where it appeared in relatively high amounts as dendrites.

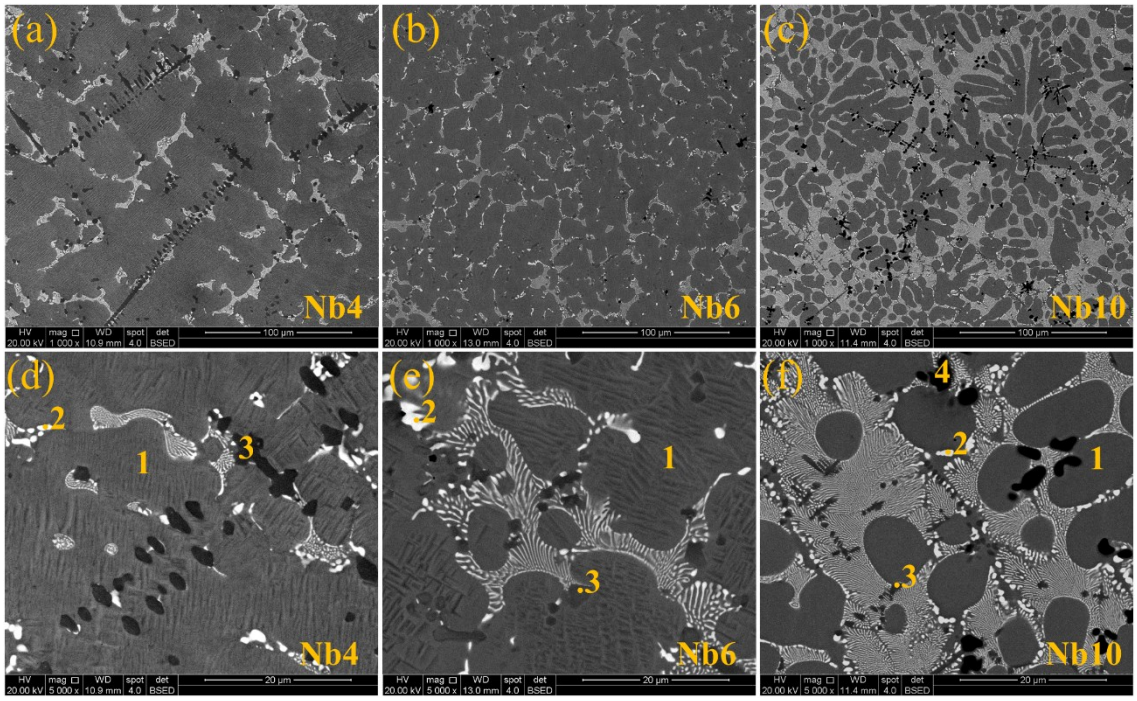

Figure 4-3 - Backscattered electron images of (a,b) Nb4, (c,d) Nb6, (e,f) Nb8, and (g,h) Nb10 alloy at (a,b,c) 1000X and (d,e,f) 5000X magnifications.

4.3.3. Effect of homogenization on the Nb10 as-cast microstructure

The Nb10 alloy was selected for the homogenization treatment such that it would be possible to observe the effect of this heat treatment on all the identified second phases, namely β-Nb, Ti_2Ni, and Ti. After homogenization, the phase constitution of the as-cast alloy was maintained, as shown in Figure 4-4.

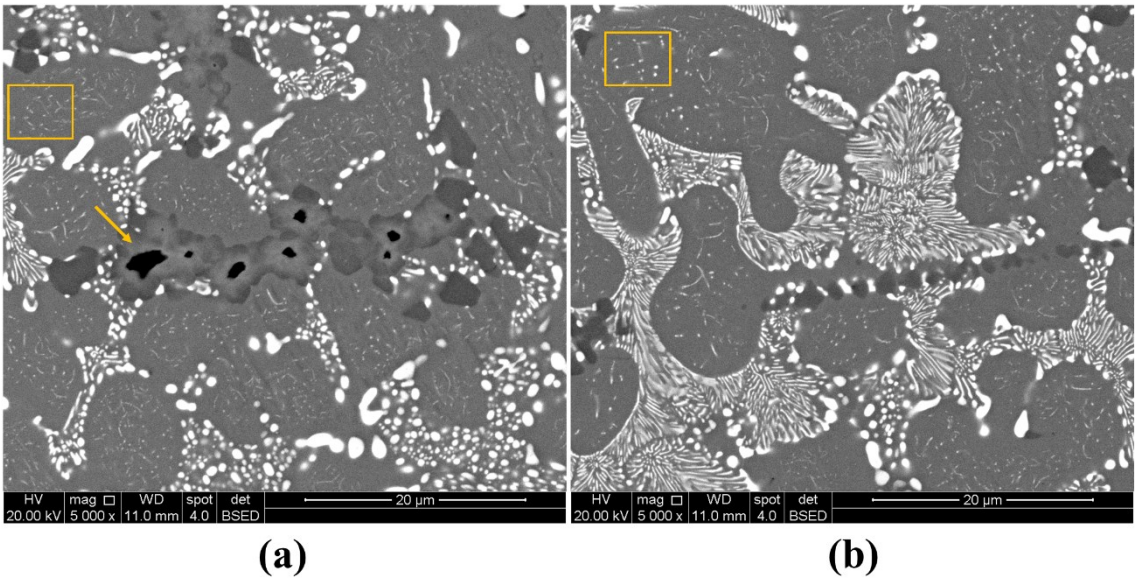

Figure 4-4 - Backscattered electron images obtained in the SEM analyses in different regions of the homogenized Nb10 alloy at 5000X magnification.

Partial coalescence of the β-Nb lamellae and Ti_2Ni particles was observed, as shown in Figure 4-4-a. By comparing with the as-cast microstructure, it appears that Ti_2Ni precipitates formed and coalesced around the Ti particles, as indicated by the arrow. There were also regions, as shown in Figure 4-4 -b, where no apparent second-phase coalescence occurred. In turn, fine precipitation within the TiNi matrix was observed both in regions with high and low second-phase coalescence, as highlighted by the rectangles. The contrast of these precipitates in the backscattered analysis suggests that they are also Nb-rich.

4.3.4. DSC analysis

The Nb6 alloy, with an intermediate Nb content, was selected for thermal stability analyses. The DSC chart obtained during the thermal cycling of this alloy, as illustrated in Figure 4-5, showed a stable transformation behavior. It exhibited an austenitic finishing temperature (Af) less than, but close to room temperature, favoring further superelastic cycling. With thermal cycling, Af varied from 13.7 °C in the first cycle to 14.3 °C in the fifth cycle, as obtained from the tangent line method. Variations of 1.2 °C and 0.4 °C were observed on the direct and reverse martensitic transformation peak temperatures, respectively.

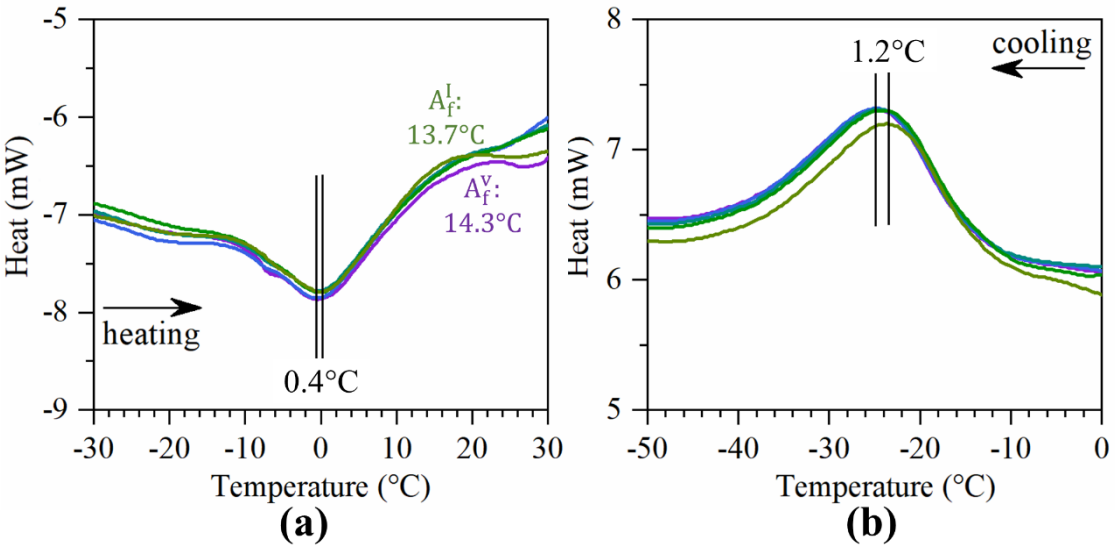

Figure 4-5 - DSC chart for the thermal cycle test of as-cast Nb6 alloy during (a) heating and subsequent (b) cooling.

4.4. Discussion

From conventional thermodynamic calculations, Figure 4-1, TiNi and β-Nb are the equilibrium phases for all the cast alloys. However, all of them exhibited similar behavior as the Ti-rich alloys, and the Ti_2Ni intermetallic phase was identified. β-Nb and Ti_2Ni particles exhibited stable behavior during homogenization; at a temperature where only small amounts of β-Nb and no Ti_2Ni are thermodynamically expected, they coalesced rather than dissolving. Metallic Ti was also observed, mainly, in the Nb10 alloy, where it was partially dissolved to form Ti_2Ni during the homogenization treatment. However, the fine precipitation of what appears to be β-Nb during homogenization may be due to a supersaturation of Nb on the TiNi matrix.

The second-phase morphology and distribution in the as-cast microstructures suggested that their formation occurred during solidification. The coalescence of these particles during homogenization, in turn, implies that local equilibrium conditions have been reached, resulting in a stable microstructure. Based on these results and discussions, the Scheil calculator was used to predict the phases formed during solidification. In this calculation, the equilibrium chemical composition of the solid phases formed at varying temperatures is considered, whereas diffusion is only expected to occur in the liquid.

In Figure 4-6, the solid phases in equilibrium with the liquid are presented as functions of temperature and solid fraction. The results are in qualitative agreement with the observed microstructure: solidification starts with the formation of the TiNi matrix, whereas the β-phase and the Ti_2Ni intermetallic phase are predicted in the final stages. The solidification process is concluded by the occurrence of a eutectic reaction in all the alloys. In Nb4 and Nb6, Ti_2Ni solidification occurs before the eutectic reaction, being favored in the alloy with a lower Nb content. In Nb10, the β-phase appears first. The eutectic temperature is related to the presence of all these three phases in equilibrium with the liquid. Because it is a quaternary system, a reaction taking place at a constant temperature implies a four-phase reaction, L → TiNi + β + Ti_2Ni.

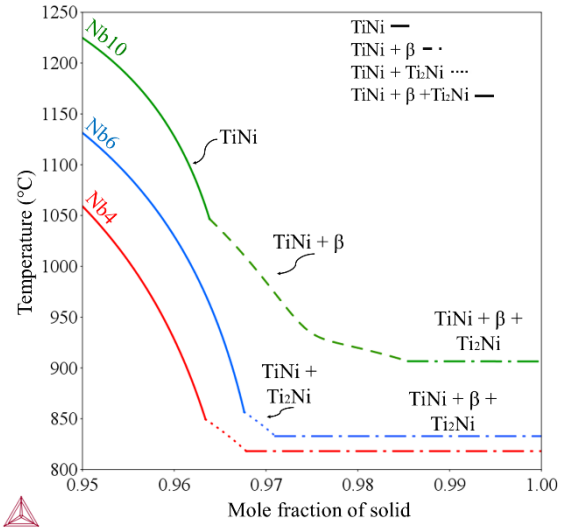

Figure 4-6 - Simulation of solidification using the Scheil calculator.

It is worth pointing out that the presence of metallic Ti, which exhibits a high-temperature β crystal structure, was highlighted in Nb10, where the Scheil calculation predicted the formation of the BCC β-phase outside of the eutectic reaction. Because the β-phase can present varying Ti and Nb contents in the thermodynamic calculations, it appears that the formation of β-Ti is favored at higher temperatures whereas the formation of β-Nb takes place in the three-phase L→ β-Nb + TiNi eutectic. In this case, in addition to favoring the occurrence of a three-phase L → β-Nb + TiNi eutectic, the calculated β-phase may be related to the formation of β-Ti.

Considering that cooling takes place out-of-equilibrium, possibly leading to high chemical segregation when solid phases are formed, further analyses on the equilibrium phases that take place were performed. Virtual liquid compositions at varying temperatures for the Nb6 alloy, obtained via Scheil calculations, were used in the equilibrium calculator to obtain pseudobinary diagrams considering the tendencies observed in the liquid composition variation. Under 90% solid formation, Ti-Ni pseudobinaries were analyzed with fixed Nb and Cu contents at different stages, Figure 4-7-a. In this region, the formation of the three-phase L → β + TiNi eutectic succeeding the pre-eutectic formation of TiNi is expected, even within the TiNi + liquid region shown in Figure 4-6.

In the final stages, Figure 4-7-b, where the calculated Ni and Cu contents were relatively low and fixed, a Ti-Nb pseudobinary was analyzed such that the partition of Ti and Nb in a liquid enriched in these elements could be assessed. It was observed that the formation of Ti_2Ni can occur in different ways. At low Nb contents, it forms individually from the liquid and is succeeded by the occurrence of a four-phase L → TiNi + β + Ti_2Ni eutectic reaction. At intermediate Nb contents, it occurs only in the four-phase eutectic reaction after the formation of the β-phase and three-phase L → TiNi + β reaction. In turn, at high Nb contents, Ti_2Ni does not form, and only a three-phase eutectic is observed. These results are consistent with the different morphologies observed for this phase in the microstructural analysis of Nb6, where it appeared within the TiNi matrix in association with the TiNi + β eutectic constituent.

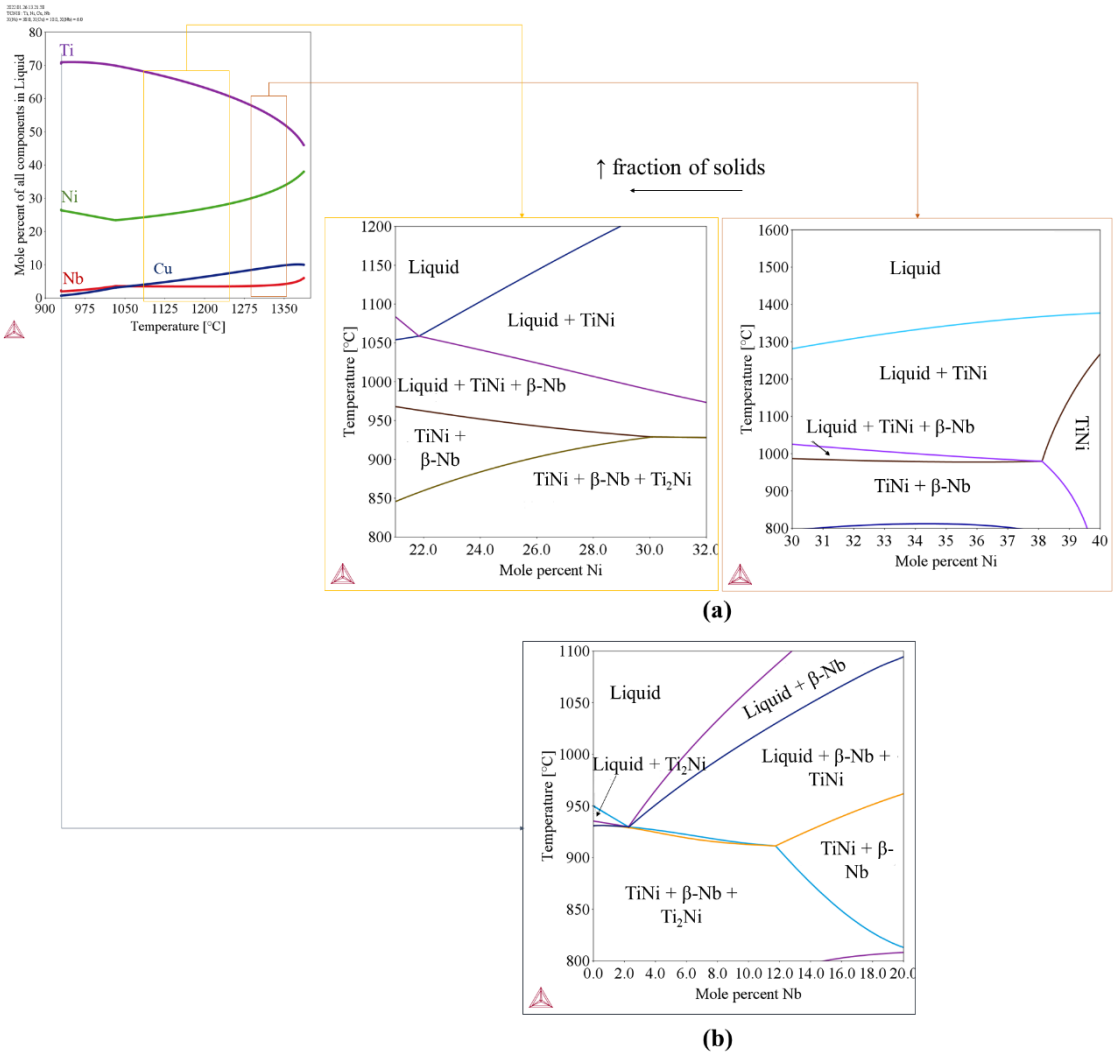

Figure 4-7 - Equilibrium analyses of (a)TiNi pseudobinary with fixed Nb and Cu contents at different stages of solidification and (b) TiNb pseudobinary with fixed Ni and Cu contents on the final stages of solidification.

The Ti-Nb pseudobinary represented in Figure 4-7-b can also be related to the effect of different amounts of Nb in the liquid phase of alloys with varying Nb contents. In Nb4, Ti_2Ni exhibited a dendritic-like morphology, which is in agreement with what is expected for compositions with lower Nb content in relation to Ti. In Nb10, where the predicted formation of Ti_2Ni only occurs in the four-phase eutectic reaction, it was only observed intercalated with the TiNi + β eutectic constituent, whereas a high fraction of the two-phase constituent was observed. This is under the expected when higher amounts of Nb about Ti occur. Therefore, it was observed that higher amounts of Nb, as observed in Nb10, hinder the formation of the Ti_2Ni intermetallic. This may be due to the effect of Nb as a solute atom in the Ti_2Ni lattice delaying its formation. Because

excess Ti is not observed in the TiNi phase, its precipitation as β-Ti may be thermodynamically and/or kinetically favored.

This behavior is closely related to the Ni-Ti-Nb ternary system, whose liquid projection, illustrated in Figure 4-8, shows the formation of different three-phase and four-phase eutectic reactions involving the TiNi, β, and Ti_2Ni phases. In alloys with higher Nb contents and, thus, higher Nb enrichments in the liquid, the formation of the β phase and three-phase L → TiNi + β reaction are favored, leading to the presence of β-Ti and higher fractions of TiNi + β-Nb lamellae. In contrast, alloys with lower Nb contents exhibited a favored formation of Ti_2Ni, which was also embedded in the TiNi matrix, while no β-Ti was observed.

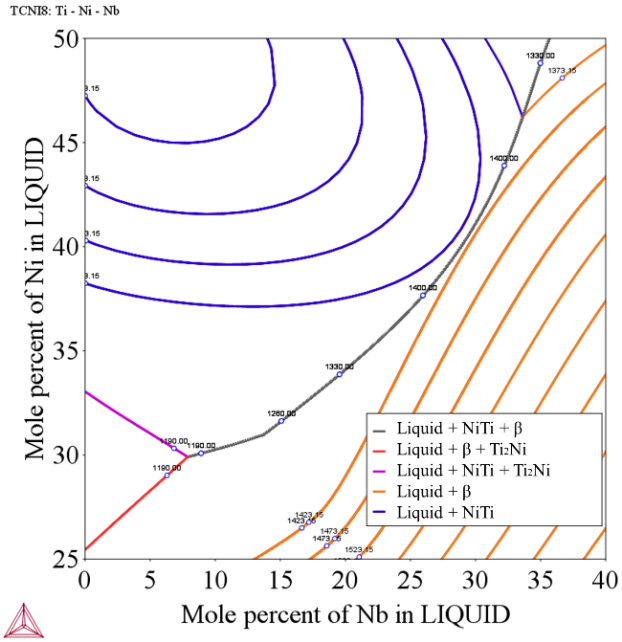

Figure 4-8 - Liquidus projection of ternary Ti-Ni-Nb

Therefore, the phases obtained in the as-cast alloys were observed in the equilibrium phase diagrams when chemical segregation during solidification was considered. Furthermore, the different morphologies and distributions observed are consistent with the different cooling sequences in these calculations and were directly related to the Nb content of the alloy. The resultant microstructure exhibited high stability because local equilibrium was reached, and metastable second phases were not easily dissolved, as indicated by the homogenized microstructure.

Although the produced alloys presented a complex microstructure constituted by metastable phases that were not dissolved during homogenization, the TiNi martensitic transformation promoted in the calorimetric test of the as-cast alloy exhibited high reproducibility. Because higher changes in transformation temperatures are expected to occur within the initial thermal cycles in TiNi alloys [28–32], the reproducibility observed in the martensitic transformation of the alloy indicates a high thermal stability.

An Af less than, but close to room temperature, obtained for the Nb6 alloy indicates that superelastic behavior may be achieved at room temperature. Therefore, the results achieved for the as-cast microstructure indicate the potential of alloys with stable room-temperature superelasticity.

4.5. Conclusions

In this study, $Ti_{52-x}Ni_{38}Cu_{10}Nb_x$, x = 4, 6, and 10 at% alloys were produced, and the effect of Nb on the phase stability was evaluated using microstructural analyses and thermodynamic simulations. All the cast alloys were composed of a matrix TiNi phase, a eutectic TiNi/β-Nb constituent, and Ti_2Ni precipitates. Despite not being expected from ideal equilibrium conditions, β-Nb and Ti_2Ni can be formed during solidification owing to chemical segregation: the former, in eutectic reactions, and the latter, embedded in the TiNi matrix or within a four-phase eutectic constituent. The morphology of the Ti-rich intermetallic was associated with the Nb content of the alloy and Ti/Nb partition on the liquid. A higher Nb content seemed to hinder the formation of Ti_2Ni, and metallic Ti was also observed in Nb10. This phase constitution exhibited stable behavior during homogenization treatment, which was related to the development of local equilibrium conditions.

5. EFFECT OF Nb ADDITION ON THE THERMODYNAMIC OF SOLIDIFICATION IN A Ti-Ni-Cu ALLOY

5.1. Introduction

In Chapter 4, the effect of Nb on the phase stability in $Ti_{52-x}Ni_{38}Cu_{10}Nb_x$ alloys was evaluated. The as-cast phase constitution could not be predicted on conventional thermodynamic calculations, being related to chemical segregations during solidification. However, the metastable second phases presented high stability during homogenization treatment. In this study, we aim to use the CALPHAD method employing the Scheil calculator in association with experimental microstructural and semi-qualitative chemical analysis (EDS) to provide further understanding on the development of different phases during solidification of TiNiCuNb alloys.

5.2. Experimental Procedure

$Ti_{52-x}Ni_{38}Cu_{10}Nb_x$ alloys with Nb additions of x = 4, 6, 8 and 10 at% were produced from elemental constituents (>99.5% purity) into 30 g ingots by arc-melting using 250-300 mA in a water-cooled copper mold. Samples were remelted at least six times to promote chemical homogeneity. The cast alloys will be hereafter referred as Nb4, Nb6, Nb8 and Nb10, according to the alloy's Nb content.

X-ray diffraction (XRD) was used for phase identification in a Panalytical Empyrean diffractometer with Cu-Kα radiation and a scan speed of 0.02°/s. The microstructure of the as-cast alloys was evaluated by scanning electron microscopy (SEM – FEI Inspect and FEI Quanta 3D FEG) using backscattered electrons. EDS mapping and punctual analyses were performed to provide a comparative analysis on the solute distribution within different phases.

Solidification and thermodynamic simulations were performed using the CALPHAD method on ThermoCalc employing TCNI8 – v8.1 database. Scheil-Gulliver solidification simulation assumes that mixing of all elements is effective in the liquid while no diffusion occurs in the solid phases. Thermodynamic equilibrium is considered in liquid/solid interface. The use of this method allows to consider the solute redistribution during solidification, which can provide insights on how solute segregation leads to the formation of out-of-equilibrium phases (164–166). Some examples where this model has been used to describe the solidification behavior in

various systems can be found in Refs. (167–170). In this study, variations in the liquid composition during solidification were obtained using Scheil calculator. The equilibrium calculator was used to assess equilibrium, considering the chemical segregation that generates different phases during solidification as measured by Scheil calculations and EDS element distribution through phases formed in different stages of solidification.

5.3. Results and Discussion

5.3.1. Microstructure and phase constitution of the as-cast alloys

TiNi, Ti_2Ni and β-Nb phases were identified by means of XRD, as pointed out Figure 5-1-a. In the as-cast microstructures, Figure 5-1- b-e, TiNi is the matrix phase; β-Nb appeared mainly in a eutectic constituent with TiNi; and Ti_2Ni presented geometric and dendritic-like morphologies, frequently associated with β-Nb and the eutectic constituent. Additionally, metallic Ti was identified via EDS in Nb10, where it appeared as dendrites. No Cu-rich phase or Cu/Nb intermetallic were observed. Further evaluation on the effect of Nb on the alloys' microstructure were explored in Chapter 4.

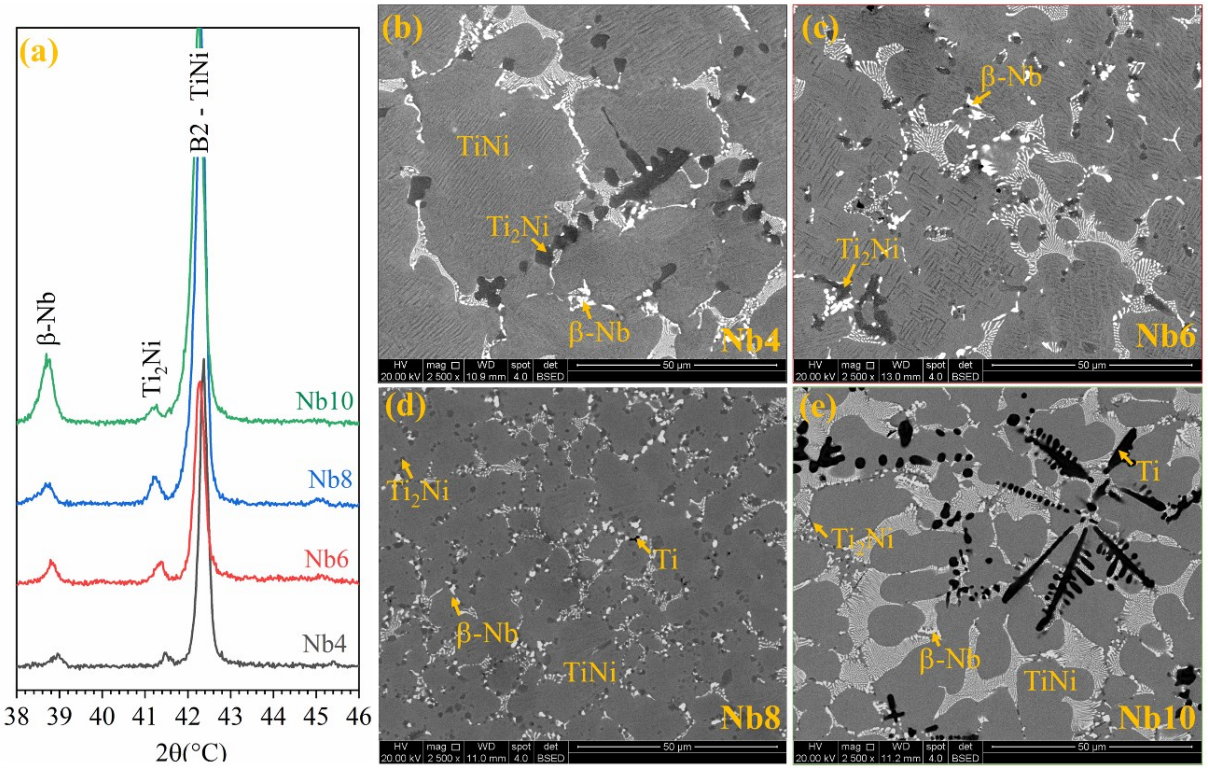

Figure 5-1- (a) XRD pattern and backscattered electrons images of (b) Nb4, (c)Nb6, (d) Nb8 and (e) Nb10 as-cast alloys.

5.3.2. Computational thermodynamic analysis

The microstructure constitution of the as-cast alloys was previously pointed out to be in qualitative agreement with results obtained from the Scheil solidification calculator (Chapter 4, section 4.4), plotted in Figure 5-2-a. It is expected that solidification starts with the formation of TiNi and finishes with the formation of Ti_2Ni and β-Nb. Variations on the amount of Ni and Ti in the liquid phase during solidification are presented in Figure 5-2-b and -c, respectively. When the TiNi matrix is formed, enrichments on the Ti content concurrent to decreases on Ni's were observed in all compositions. The composition profile changes in the final steps of solidification, with the formation of second phases, as indicated by the full arrows. The calculated chemical gradient of these two elements on liquid are greater with decreasing Nb content, and the second-phase development is favored in the alloy with the highest Nb percentage.

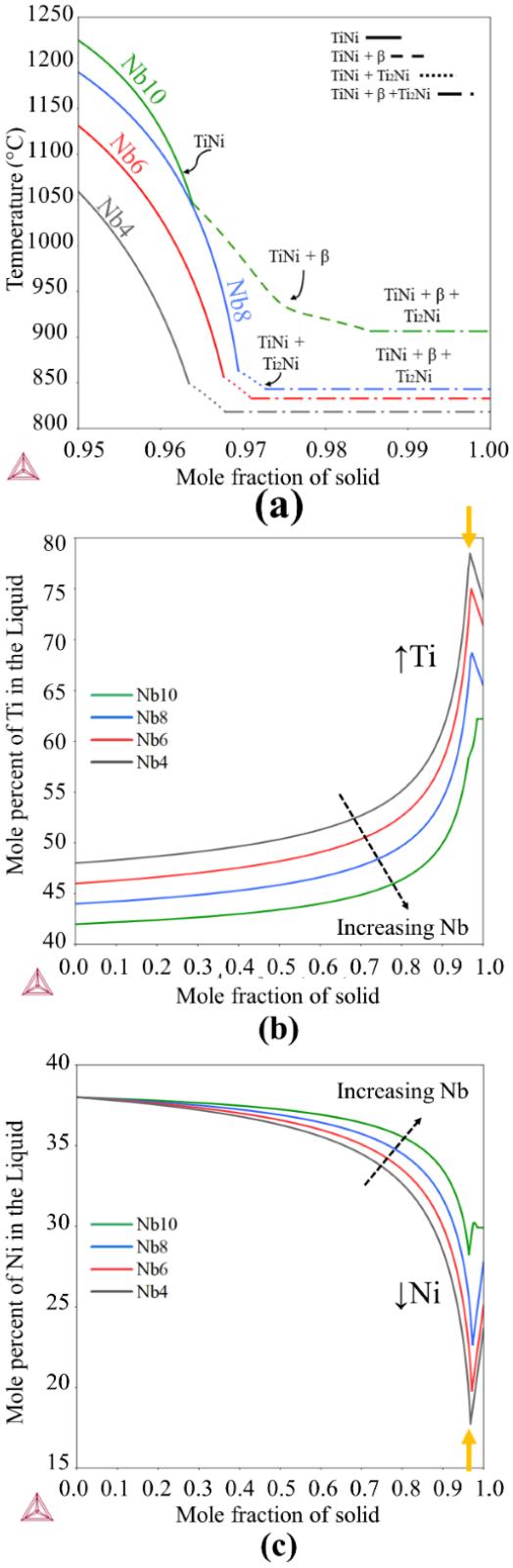

Figure 5-2 - (a) Solid-phases in equilibrium with the liquid as a function of temperature and mole fraction of solid, and variations of (b) Ni (c) Ti contents in the liquid as a function of mole fraction of solid obtained via Scheil calculator.

In Figure 5-3, pseudobinaries of the Ti-Ni phase diagram with fixed amounts of 4at% Nb and 10at% Nb are plotted. From Scheil calculations, solidification leads to chemical variations on the liquid as indicated by arrows in the region of excesses of Ti in relation to Ni. In the phase diagram with fixed 4at% Nb (Figure 5-3-a), a three-phase field containing TiNi, Ti_2Ni and liquid is observed after the two-phase liquid + TiNi field. The presence of the Ti-rich Ti_2Ni intermetallic in equilibrium with the liquid may be associated with its dendritic morphology in Nb4 alloy (II in the inset of Figure 5-3-a).

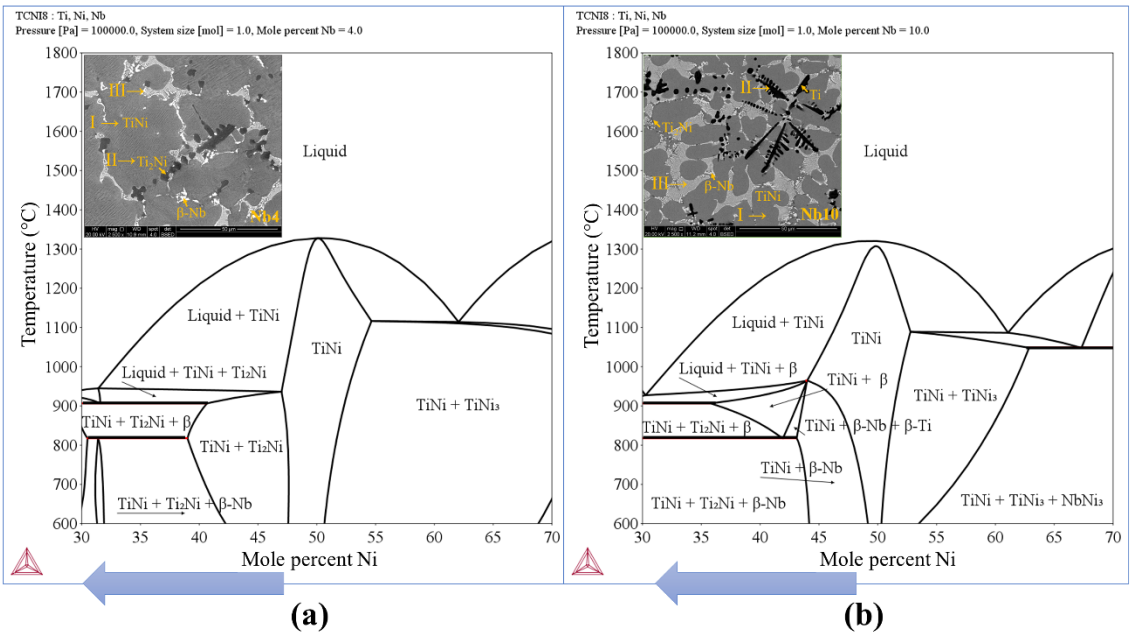

Figure 5-3 - TiNi pseudobinaries with fixed amounts of (a) 4 at% Nb and (b) 10 at% Nb.

In the 10at%Nb phase diagram (Figure 3-b), a TiNi, β and liquid region is observed instead. The β phase presents varying amounts of Ti and Nb, depending on the temperature and composition: Ti-rich solid solutions are favored at high temperatures and Ti enrichments. Hence, it appears that Nb decreases the stability region of Ti_2Ni, favoring the solidification of β-Ti dendrites in Nb10 (II in the inset of Figure 3-b).

In both diagrams (Figure 5-3), solidification finishes in a TiNi + β + Ti_2Ni field, leading to the simultaneous formation of these phases. At temperatures lower than 800°C, TiNi + β-Nb +

Ti_2Ni are in equilibrium within a large range of compositions, which could be responsible for their high stability during heat-treatments. In turn, β-Ti is only stable at high temperatures, which could explain the partial dissolution previously observed (15) during heat-treatment. In this manner, it can be noted that the solidification sequence and developed phases are intimately related to the TiNiNb system.

5.3.3. Solute distribution

The distribution of elements in the different alloys obtained by EDS mapping is presented in Figure 5-4. Semiquantitative results obtained by punctual analyses are presented in Figure 5-5. The presence of Ti can be highlighted in Ti_2Ni and β-Ti while lower fractions are observed in the β-Nb phase, as pointed out, respectively, by white and yellow arrows in Figure 5-4-b. Ni is mostly present in the TiNi matrix, where heterogeneities can be noted by the impoverishment of this element in regions adjacent to the β-Nb phase and the eutectic constituent, as pointed out in Figure 4-c. In turn, these same regions presented excesses of Cu (Figure 5-4-d). This element, which is always present as a solute, is mostly dissolved in the eutectic, preferably in the TiNi phase as evidenced in Figure 5-5-c. In turn, low solubility is observed in the Ti-rich second phases. Nb is mainly present as the β-Nb phase (Figure 5-4-e), where Ti was the main solid solution atom (Figure 5-5-a). The presence of the eutectic constituent with β-Nb phase and the concentration of Nb indicate an accumulation of Nb on the liquid in the final stages of solidification.

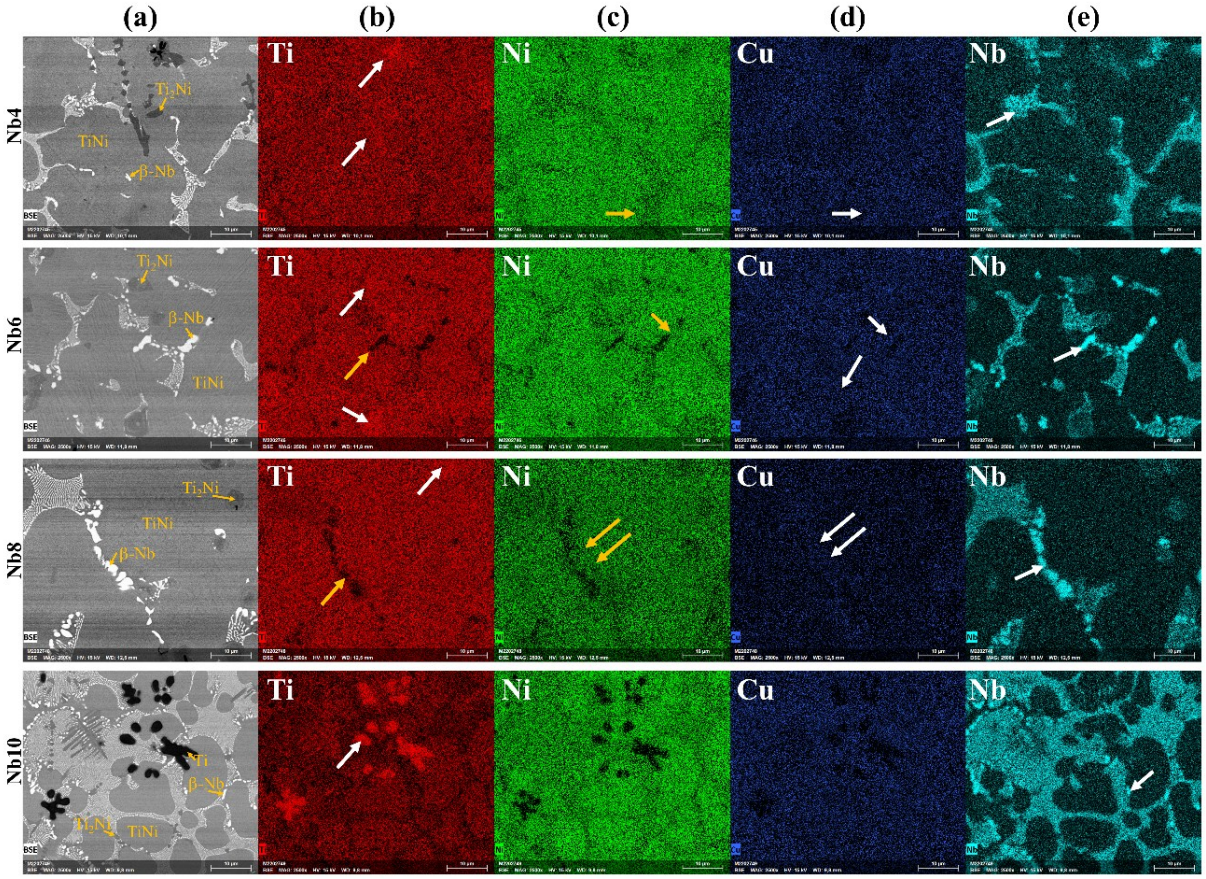

Figure 5-4 - EDS mapping in (a) Nb4, Nb6, Nb8 and Nb10 microstructures showing the distribution of (b) Ti, (c) Ni, (d) Cu and (e) Nb.

From the punctual analyses (Figure 5-5), it can be observed that TiNi, the primary phase formed during solidification, presented similar amounts of Ti (Figure 5-5-a) and Ni (Figure 5-5-b) in alloys with varying Nb contents. In the eutectic constituent, mean amounts of 27-31 at% of Ni and 40-43at% Ti were measured. The mean mole fraction of Nb (Figure 5-5-d) in this constituent varied from 16at% to 23at%, increasing with increasing Nb content in the alloy. Virtually equal amounts of Ni have been observed in the eutectic constituent and the Ti_2Ni phase, Figure 5-5-b, formed in the final steps of solidification. This may indicate that they form simultaneously when the Ni content in the liquid reaches a critical value. This agrees with Scheil calculation results, which shows the depletion on the Ni content of the liquid with an inflection point when second phases are formed.

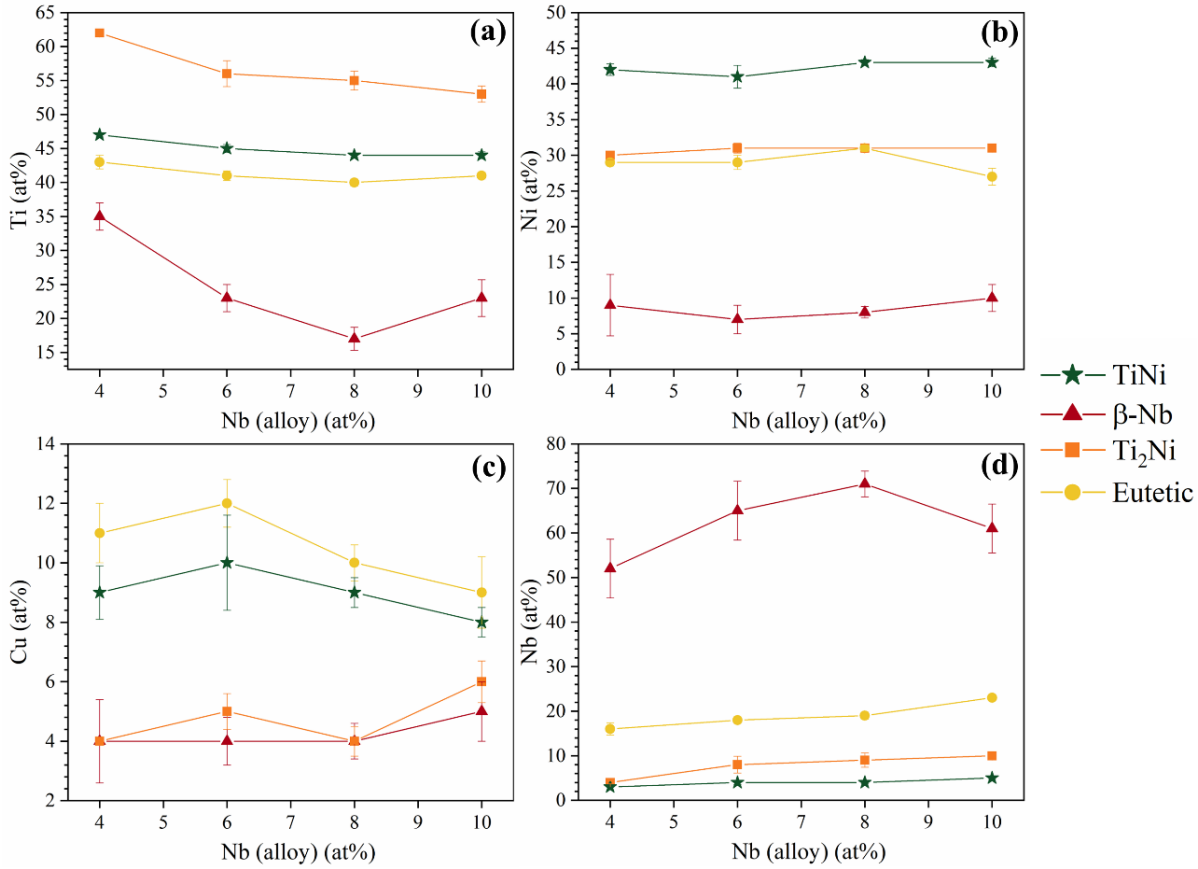

Figure 5-5 - Mean contents of (a) Ti, (b) Ni, (c) Cu, and (d) Nb in different phases and the eutectic as a function of Nb content of the alloy measured by semiquantitative EDS analysis.

In turn, measured Nb-contents in the eutectic constituent indicate that there is a Nb accumulation in the liquid. Hence, the relationship between diminishing Ni and increasing Nb was assessed by a Ni-Nb pseudobinary calculation with fixed amounts of Ti and Cu as the base alloy (52at% and 10at% respectively), plotted in Figure 5-6. It can be observed that the diminishing Ni content is sufficient for the formation of the eutectic involving β-Nb. When the Nb content of the alloy is higher, and, hence, a higher enrichment of Nb on liquid is expected, the eutectic reaction involving NiTi and β-Nb occurs at higher temperatures and the formation of β-Nb is favored. On the other hand, Ti_2Ni is only an equilibrium phase in poor Nb content regions. This means that they could either be formed at earlier stages of the studied alloys, as in alloys with low Nb additions such as Nb4, or through the partition of Ti and Nb in the final stages of solidification.

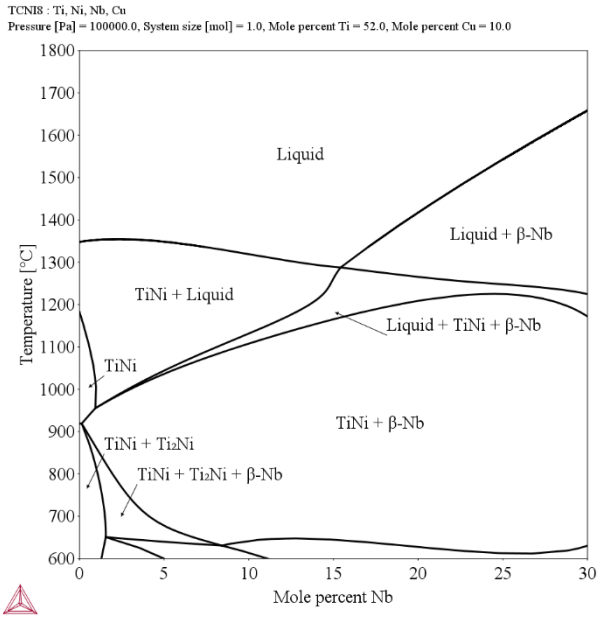

Figure 5-6 - Effect of increasing Nb and diminishing Ni in Ni-NbTi52Cu10 pseudobinary.

Ratios of mean elements contents in each intermetallic phase were assessed to evaluate stoichiometry fits. As it can be observed from Figure 5-7, coherent ratios are obtained in TiNi when Cu is considered a substitute for Ni, and Nb, for Ti. In Ti_2Ni, the calculated ratio fits the stoichiometry best when only Nb is considered a substitute for Ti. These results are endorsed by previous observations that Nb occupy Ti sites in Ni-Ti intermetallic phases on Ni-Ti-Nb ternary (16).

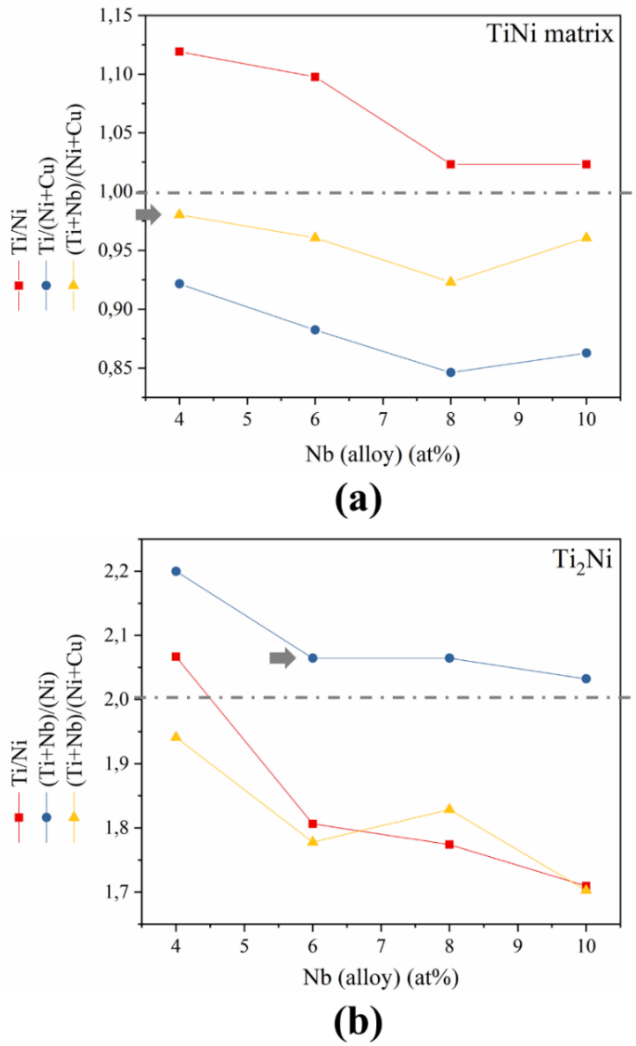

Figure 5-7 – Measured element ratios in (a) TiNi and (b) Ti_2Ni intermetallic.

5.3.4. Solidification of the cast alloys

Based on Scheil calculations, pseudobinary equilibrium extrapolations and EDS results discussed in the previous sections, it is proposed that solidification occurs as follows (Figure 5-8). The TiNi matrix phase is formed, and the calculated liquid composition as a function of the fraction of solid phase indicated enrichments on the Ti and decreases on the Ni contents (Figure 5-8-b). This leads to the formation of Ti-rich second-phases, Ti_2Ni and β-Ti (Figure 5-8-c). Increasing alloy's Nb-content jeopardizers the formation of Ti_2Ni and favors the formation of β-Ti at high temperatures, as the β-phase is stabilized from the liquid in Ti-rich regions of the TiNi-Nb pseudobinary phase diagram (Figure 5-3).

The decrease in the Ni content and accumulation of Nb in the liquid (Figure 5-6) are associated with the formation of the eutectic involving β-Nb (Figure 5-8-d). The simultaneous formation of TiNi, β-Nb and Ti_2Ni at the final stages of solidification appears to occur when a critical Ni content is reached (Figure 5-8-e). The other elements partition within the formed phases: Ti-rich regions become Ti_2Ni while Nb-rich regions turn into the eutectic, where Cu is preferably in TiNi's lamellae.

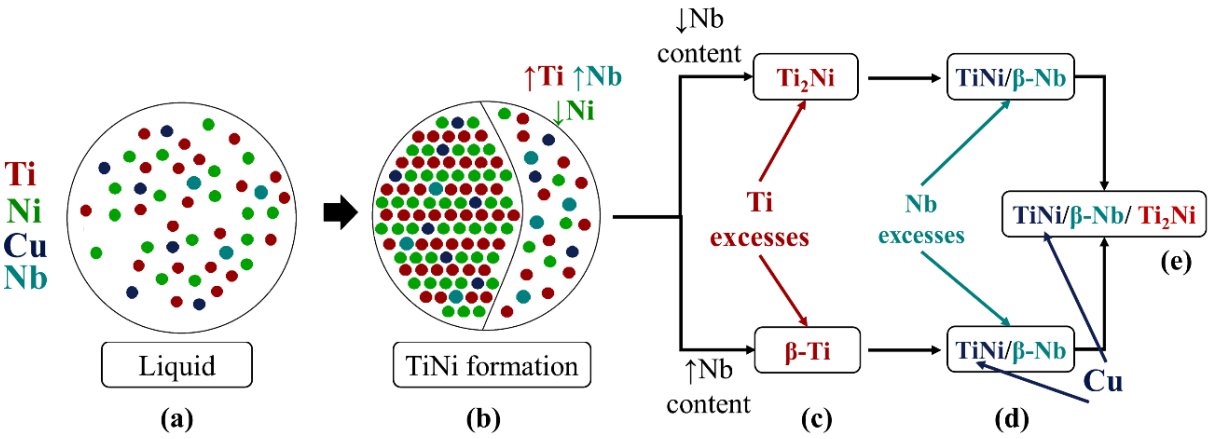

Figure 5-8 - Proposed solidification scheme of the produced TiNiCuNb alloys.

5.4. Conclusions

Solidification of TiNiCuNb alloys were evaluated from the perspective of thermodynamic simulations associated with experimental microstructural analyses. For that, TiNiCuNb alloys were produced by arc-melting and the resultant microstructure was evaluated by means of XRD and SEM/EDS. Thermodynamic simulations were performed using conventional equilibrium and Scheil calculators. TiNi, β-Nb and Ti_2Ni were observed in the as-cast microstructure and in the Scheil calculation for all the studied alloys.

It was proposed that solidification starts with the formation of TiNi, and excesses of Ti and Nb remain in the liquid while Ni is consumed. The amount of Ti and Ni in TiNi doesn't vary significatively within alloys of different Nb contents. The excess of Ti in the liquid is responsible for the formation of Ti_2Ni. Higher amounts of Nb, as observed in Nb10, hinder the formation of Ti_2Ni, favoring β-Ti at high temperatures. The decrease in Ni content and

accumulation of Nb are associated with the formation of the eutectic involving β-Nb. In the final stages of solidification, Ti_2Ni and the eutectic form simultaneously when the Ni content reaches a critical level. TiNi, β-Nb and Ti_2Ni are equilibrium phases in Ti-rich regions in TiNi – Nb pseudobinaries, which can be related to a high stability of these phases.

From element distribution analyses, it has been observed that coherent ratios are obtained in the intermetallic phases when Cu is considered a substitute for Ni, and Nb, for Ti. These results endorse that Nb occupy Ti sites. Cu is always present as a solute, preferably in the TiNi formed in the final stages of solidification while Nb precipitates as β-Nb.

6. THERMOMECHANICAL PROCESSING

6.1. Introduction

Binary TiNi alloys are easily worked in temperatures above 527°C, and the optimum temperature for hot-working is around 800°C (1). The addition of Cu to TiNi alloy was reported (108) to result in an increase in the critical stress during hot compression tests, which was attributed to the formation of high strength Cu containing precipitates and solid solution hardening of the matrix phase. In hot tensile tests, TiNi and TiNiCu alloys exhibited maximum hot ductility at the temperature ranges of 750°C-1000°C and 800-1000°C (171) respectively. This occurs when dynamic recrystallization is the dominant restoration mechanism (171,172).

At 1000°C, grain growth has been observed (108) while the formation of liquid phase was associated to a decline in ductility at temperatures above 1000°C (171). The extent of applied strain is also relevant in obtaining dynamic recrystallization at high temperature, as the strain of 0.7 was not sufficient to achieve complete dynamic recrystallization in a $Ti_{55.2}$ $Ni_{40.6}Cu_{4.1}$ alloy (173). Moreover, it was found that at temperatures lower than 750°C, diffusion assisted recovery mechanisms were not activated, leading to limited ductility in both TiNi and TiNiCu alloys (171).

Although the addition of Cu results in an alloy embrittlement (1), Nb has been previously added in TiNi-based SMAs to improve their cold-workability. In a TiNiHf SMA, a significant increase in the cold reduction ratio at room temperature was obtained, as it escalated from 20% in the alloy with no Nb to 60% in the alloy with 10at% Nb (134). A homogenized $(Ti_{50.1}Ni_{34.9}Hf_{15})_{85}Nb_{15}$ alloy containing β-Nb in a eutectic constituent and as semicoherent precipitates in a TiNiHf(Nb) matrix exhibited a cold rolling reduction ratio of 80% (174). In turn, the increase in the ductility of a TiNiCu alloy by the addition of Nb has been noted by Wang *et al.* (136).

In previous studies on TiNiCuNb alloys, the processing methodology, summarized in APPENDIX III – Manufacturing information on Ti-Ni-Cu-Nb, consisted of hot rolling followed by solution-treating (131,136,137) or hot-forging, hot-drawing and cold-drawing (135). In this chapter, as-cast $Ti_{52-x}Ni_{38}Cu_{10}Nb_x$ alloys were submitted to different processing routes and the development of their microstructure was assessed. The resultant microstructures were compared to the respective as-cast alloy. For mechanical characterization, hardness tests were

performed. Ultramicrohardness was used to evaluate the hardness distribution and DSC tests were performed to assess the martensitic transformation.

6.2. Experimental Procedure

6.2.1. Alloy casting

$Ti_{52-x}Ni_{38}Cu_{10}Nb_{x,\ x = 6,\ 8\ and\ 10\ at\%}$ were produced by arc-melting and named according to their respective Nb content as Nb6, Nb8 and Nb10. After selecting samples in the as-cast condition, the ingots were submitted to different rolling procedures. Nb6 was selected for hot rolling followed by solution treatment; Nb8, for cold rolling with intermediate heat-treatment at 800°C; and Nb10, for cold rolling. Nb6 samples in the as-cast, hot-rolled and solution-treated conditions will be hereafter referred as Nb6 - AC, Nb6 - HR and Nb6 - ST, respectively. Nb8 will be named Nb8–AC (as-cast Nb8), and Nb8-CR-IT (cold-rolled with intermediate heat treatments Nb8). Nb10 will be presented as Nb10-AC (as-cast Nb10) and Nb10-CR (cold-rolled Nb10). The identification of the samples and the processing steps which each of them was submitted to are summarized in Table Table 6.1. Descriptions of the thermomechanical processes and the characterization tests of the alloys will be presented in section 6.2.2 and 6.2.3.

Table 6.1 – Cast alloys and respective thermomechanical processing routes

Alloy ID	Chemical composition (at%)	Thermomechanical processing	ID
Nb6	$Ti_{46}Ni_{38}Cu_{10}Nb_6$	As-cast	Nb6 – AC
		Hot-rolled at 950°C	Nb6 – HR
		Solution treated at 950°C	Nb6 – ST
Nb8	$Ti_{44}Ni_{38}Cu_{10}Nb_8$	As-cast	Nb8 – AC
		Cold-rolled with intermediate heat-treatments at 800°C	Nb8 – CR - IT

Nb10	$Ti_{42}Ni_{38}Cu_{10}Nb_{10}$	As-cast	Nb10 – AC
		Cold-rolled	Nb10 - CR

6.2.2. Hot-rolling

Nb6 ingot was submitted to hot rolling at 950°C. ThermoCalc® software (v2018.b) was used for thermodynamic equilibrium calculations using TCNI8 – v8.1 database to assess the stable phases on the rolling temperature, estimate the alloy's melting temperature (T_m) and obtain equilibrium phase diagrams.

A low-carbon 15 mm thickness sheet was used as a support for the ingot to prevent heat losses during the hot-rolling process. For that, a cavity was machined in the central region of the sheet. Ingot and steel support set was heated in a muffle furnace at the rolling temperature (950°C) for 40 min before the initial deformation step. Then, re-heating was performed between each of the following rolling steps for 5-10 min. The procedure was interrupted when the high reduction on the steel-sheet caused a loss of efficiency and significant heat losses were visually noted during deformation.

Nb6–AC and Nb6-HR were prepared for metallographic analysis using backscattered electrons in a FEI - Inspect S50 SEM/EDS. Hardness measurements were performed in the transverse region of the samples in a FM-700 (Future-Tech) microhardness tester using Vickers indenter in Nb6-AC and Nb6-HR. 1000gf load with 10 seconds indentation time were used. Dynamic ultra-microhardness tests were performed in a DUH-W201S (Schimadzu) tester using 10gf (100mN) load, 10s holding time, 1.67 loading speed and a triangular pyramid Berkovich indenter with a ridge angle of 115°. DSC tests were performed in Nb6-AC and Nb6-ST samples in a Shimadzu DSC-60 to assess the martensitic transformation. Cooling/heating cycles consisted in heating the samples from -100°C to 100°C and, then, cooling it back to -100°C at ± 10°C/min.

6.2.3. Cold-rolling

2.5 mm and 1.8 mm thickness samples were machined, respectively, from the Nb8-AC and Nb-10-AC ingots. These samples were submitted to cold rolling at room temperature. Intermediate

heat-treatments were performed at 800°C for 60 min followed by air cooling during cold rolling of Nb8 alloy. Microstructural analyses using SEM and hardness measurements were performed as described for the Nb6 alloy. ThermoCalc® was used to calculate the alloy's melting temperatures.

6.3. Results

6.3.1. Hot-rolling of Nb6 alloy

The molar fraction of phases under equilibrium in Nb6 is plotted as a function of temperature in Figure 6-1-a. The calculated alloy's melting temperature is 1324.5 °C (1597.5 K), resulting in a homologous working temperature of 0.77 at the rolling temperature of 950°C (1223 K). At this temperature, TiNi is the only stable phase under equilibrium. During hot-rolling, the as-cast ingot's thickness of 8.3 mm was reduced to 3.4 mm on 12 steps, resulting in a total reduction of 59% and a true strain of -0.89.

Backscattered electron imagens (BSEI) of Nb6-AC and Nb6-HR are presented in Figure 6-1-b and c, respectively. Phases identified in Chapter 4, section 4.3.2, are pointed in Figure 6-1-b. As previously noted, the as-cast microstructure is constituted by a TiNi matrix embedded between TiNi/β-Nb eutectic islands and Ti_2Ni precipitates. Slots can be seen through the matrix phase, as indicated in the inset image in Figure 6-1-b. The microstructure of the processed alloy is characterized by the coalescence of second phase particles. Voids and cracks can be seen in Ti_2Ni coalesced precipitates, as pointed by arrows in the inset of Figure 6-1-c. Within the matrix phase, a fine precipitation, as circled in Figure 6-1-c, is observed while slots are no longer present. It can be seen through EDS mapping, Figure 6-2-b, that these precipitates are regions of Nb accumulation. In Nb6-AC (Figure 6-2-a), such chemical heterogeneities were not detected.

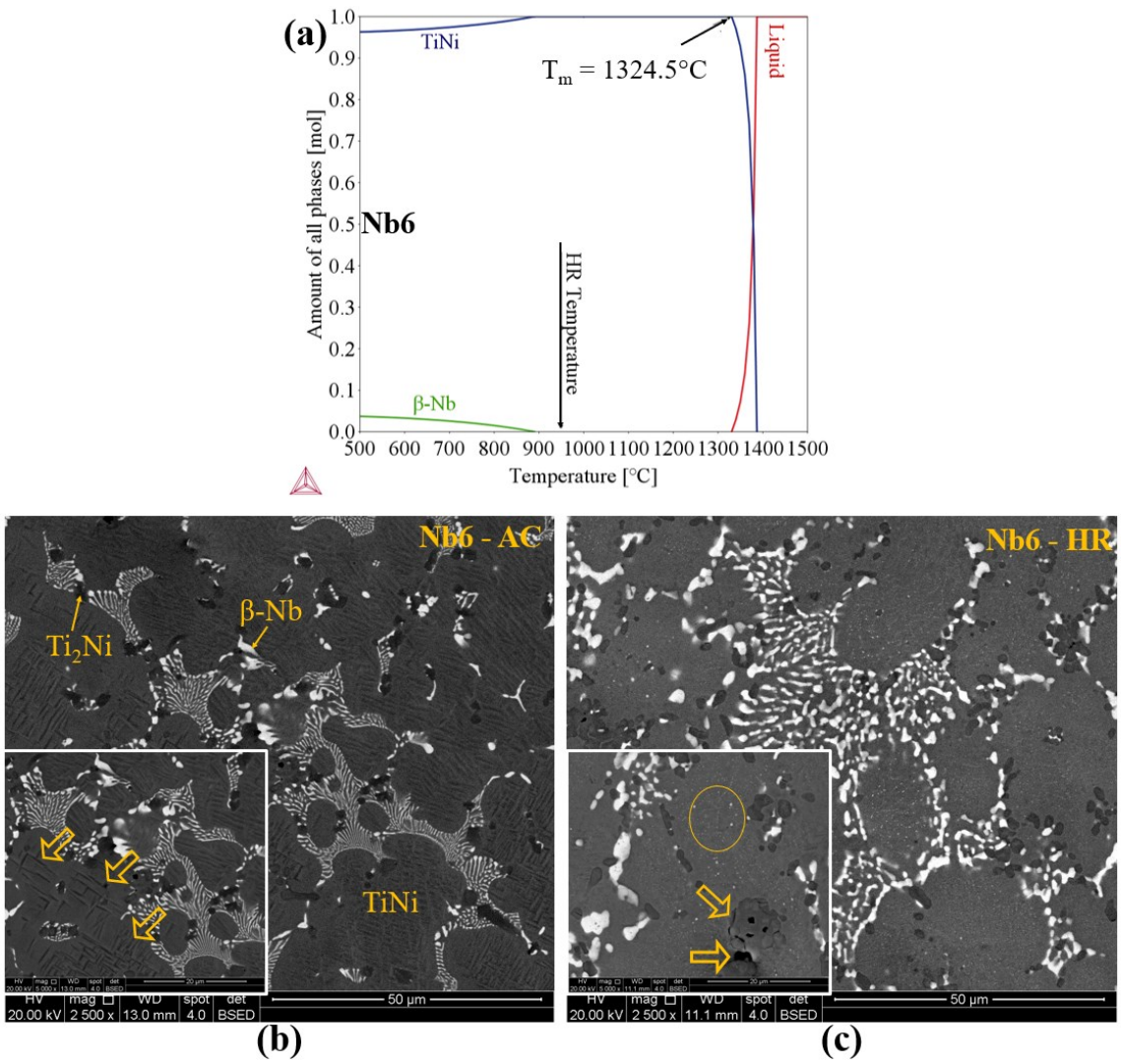

Figure 6-1 – (a) Amount of each phase as a function of temperature obtained from thermodynamic calculations; BSEI of the microstructure of (b) as-cast and (c) hot-rolled Nb6 alloy

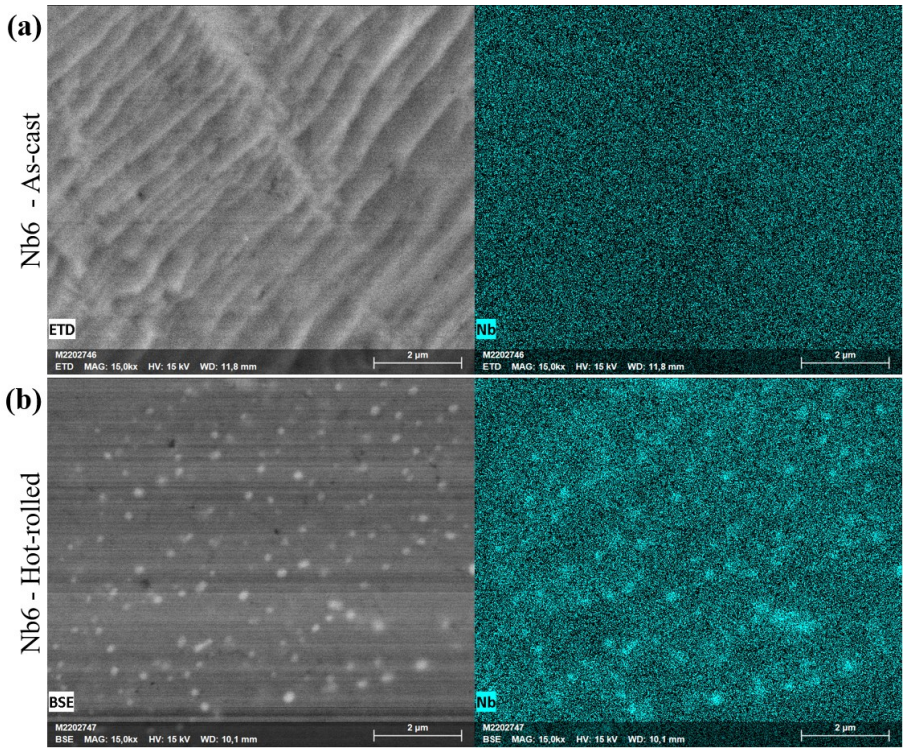

Figure 6-2 - EDS mapping of Nb in the TiNi matrix phase of (a) Nb6-AC and (b) Nb6 - HR

In the Vickers-microhardness test, mean values of 228 ± 6 HV and 207 ± 10 HV were obtained respectively for Nb6-AC and Nb6-HR. The population means are significantly different at the 0.05 level (ANOVA One-Way test), indicating modest softening of the hot-rolled sample. The applied force vs indentation depth curves obtained in the dynamic ultra-microhardness tests are plotted in Figure 6-3-a; the distribution of the dynamic hardness calculated from the maximum depth (DHT 115) is presented in Figure 6-3-b; the distribution of the elastic modulus by indentation obtained from the ultramicrohardness curves is presented in Figure 6-3-c.

Indentation depths at 100mN load varied from 0.6 to 1.2 μm in Nb6-AC and from 0.6 to 1.4 μm in Nb6-HR (Figure 6-3-a). Accordingly, the dynamic hardness measurements revealed a higher dispersion in Nb6-HR, reflected by a flatter distribution curve's profile (Figure 6-3-b). In respect to the elastic moduli (Figure 6-3-c), most measurements in Nb6-AC lie within the 75-100 GPa interval. In Nb6-HR, this interval shifts to 50-75 GPa, indicating a decrease in the overall elastic modulus, whereas a broader dispersion is also observed.

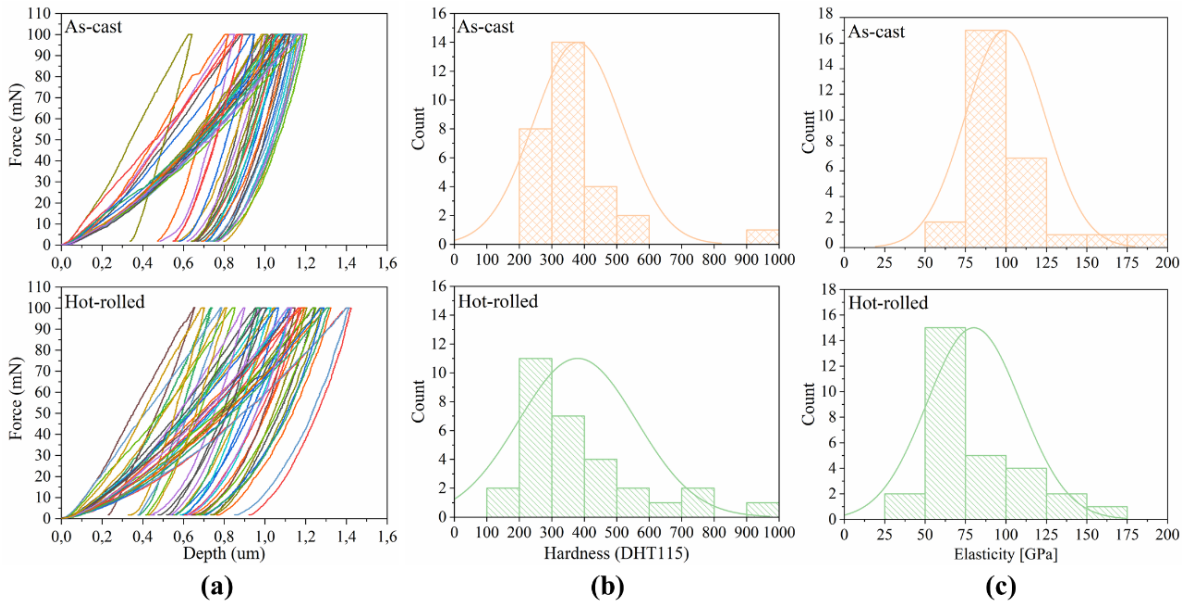

Figure 6-3 - (a) Applied force vs indentation depths, (b) dynamic hardness and (c) elastic modulus obtained by ultra-microhardness test

Heterogeneities on the hot-rolled alloy's properties can also be seen in the DSC charts, presented in Figure 6-4. While the reversible MT occurs in one step in a well-defined peak in Nb6-AC, a scattered transformation behavior is noted in Nb6-HR-ST. In this last sample, the presence of several peaks throughout a wide range of temperatures can be observed.

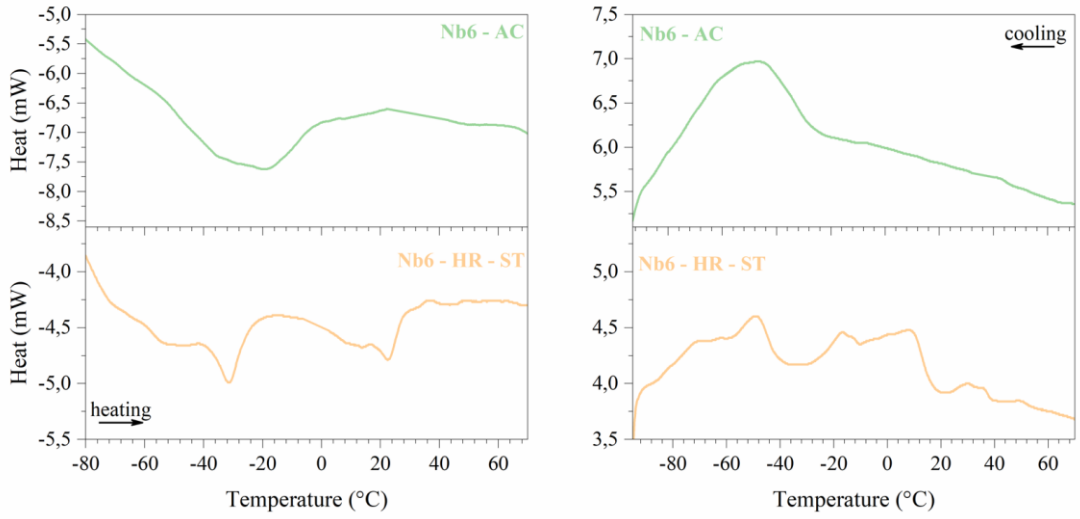

Figure 6-4 - DSC charts for as-cast and hot-rolled Nb6 alloy

6.3.2. Cold-rolling of Nb8 and Nb10 alloys

In Nb10, a total reduction of 25.5% and a true deformation of -0,29 were produced after 5 cold-rolling steps. Microhardness varied from 279 ± 9.1 in Nb10-AC to 360 ± 4.6 in Nb10-CR, exhibiting an increase of 29%. In Nb8, a reduction of 33% and a total deformation of -0,4 were promoted after 11 rolling steps. Intermediate heat-treatments in Nb8-CR-IT were performed after steps 7 and 10. The heat-treating temperature, 800°C, refers to a homologous temperature of 0.64 (calculated T_m= 1393.1 °C). Mean microhardness values of 261 ± 6.3 and 272 ± 11.4 in were obtained, respectively, in Nb8-AC and Nb8-CR-IT. This corresponds to a 4% increase.

Microstructural analyses of the cold-rolled alloys in comparison to the respective as-cast conditions are presented in Figure 6-5. For Nb10–AC, an image from the border was selected because it refers to the region which was submitted to cold-rolling. In both alloys, Ti_2Ni and Ti particles showed cracks, more notably in Nb10-CR, as pointed by arrows Figure 6-5Figure 6-5-b and -d and their insets. When intermediate heat-treatment is performed, a fine precipitation within the matrix phase was observed, as circled in the inset of Figure 6-5-b.

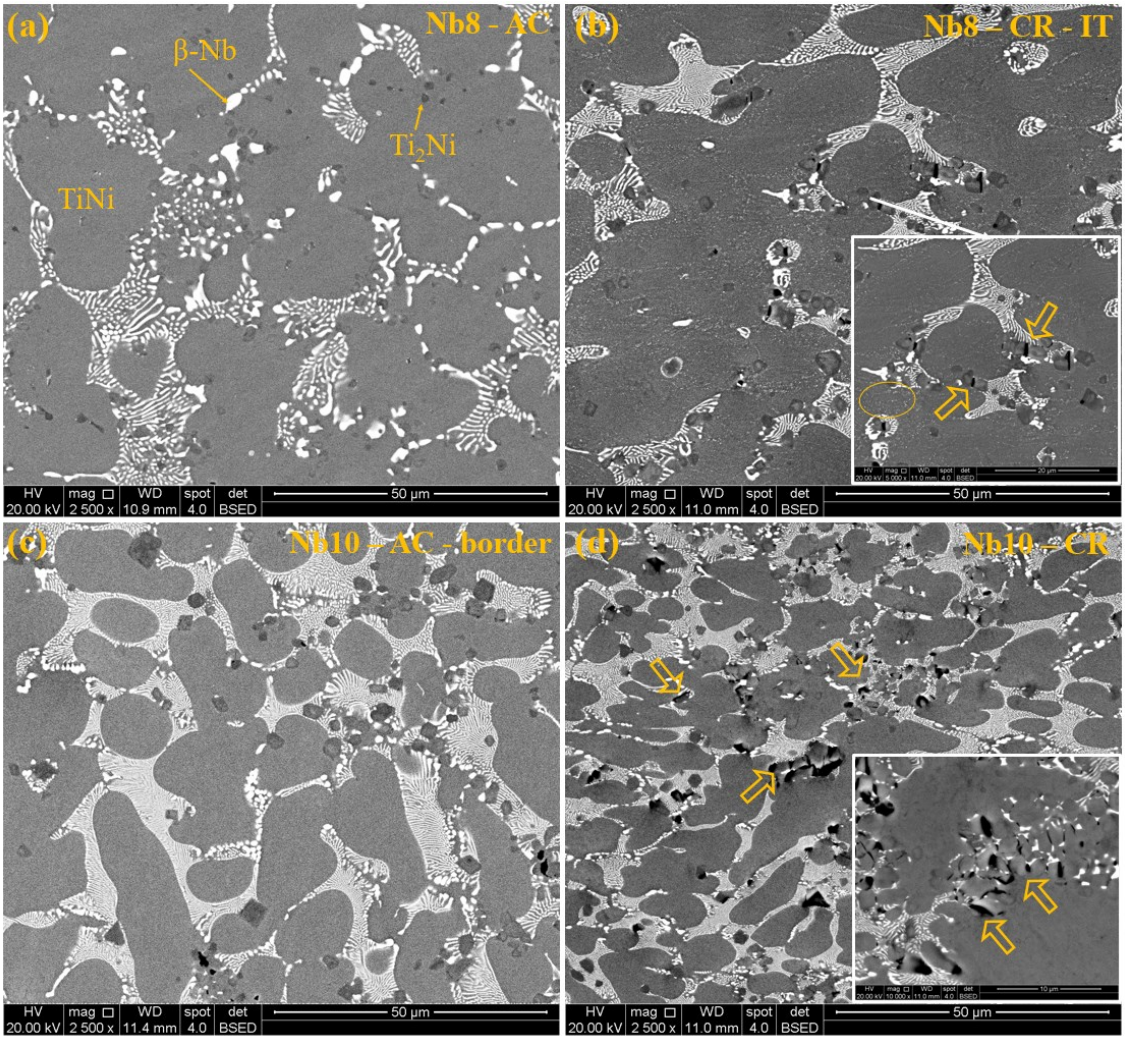

Figure 6-5 - BSEI of (a) as-cast Nb8, (b) cold-rolled Nb8, (c) as-cast Nb10 and (d) cold-rolled Nb10

6.4. Discussion

6.4.1. Microstructural evolution

In the as-cast alloys, TiNi, β-Nb and Ti_2Ni phases were previously identified, as presented in section 4.3.2. Slots were observed within TiNi grains in Nb6 - AC. Further studies are required to identify the origin of this rugosity. After hot rolling, this morphology was eliminated, and a fine precipitation was observed through the matrix phase. The precipitation of nearly pure β-Nb has been previously reported in thermally processed Ti-Ni-Nb alloys (163,175). The concentration of Nb in the precipitates in Nb6-HR's EDS mapping, Figure 6-2-b, is an

indication that these are β-Nb precipitates. Precipitation of fine β-Nb particles was also observed in Nb8-CR-IT, which was submitted to intermediate heat treatments. This precipitation presented different patterns in the hot- and cold-rolled alloys, as highlighted in Figure 6-6. Even though the presence of β-Nb in the eutectic is considerable, it appears that TiNi is supersaturated of Nb in the as-cast structure. This solute atom may be associated with dislocations during rolling, resulting in heterogenous distributions of the precipitated Nb-rich phase.

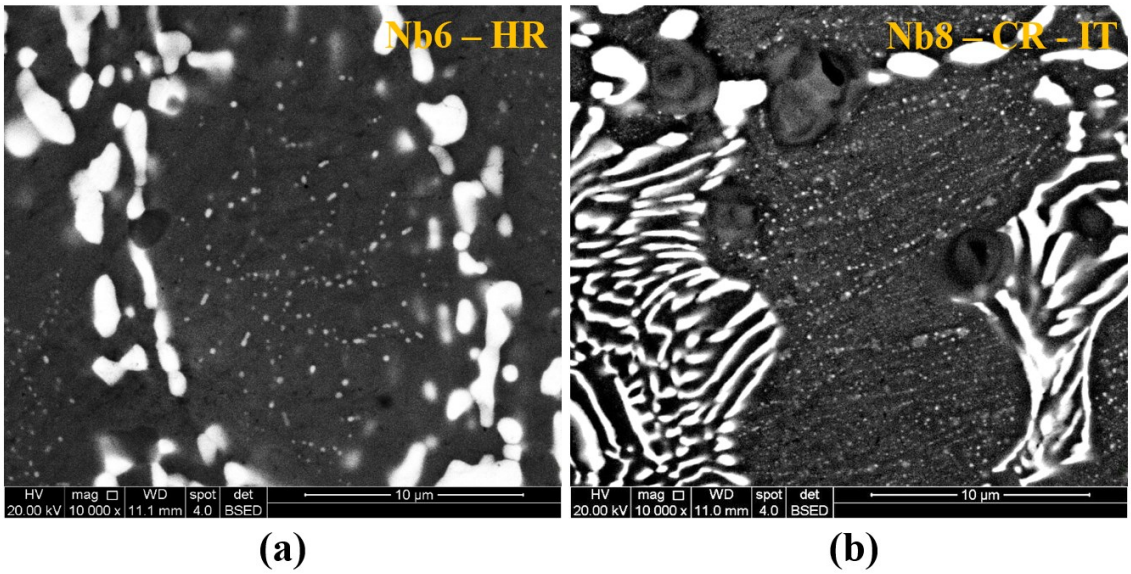

Figure 6-6 – Precipitation of Nb-rich phase in (a) hot-rolled Nb6 and (b) cold-rolled Nb8 with intermediate heat-treatments.

Moreover, second-phase coalescence is observed even though the procedure was performed in a single-phase TiNi equilibrium temperature. The presence of voids within the Ti_2Ni precipitates in Nb6-HR leads to the hypotheses that this phase melted during hot-rolling, which would result in localized solidification shrinkage and contraction cracks. According to the experimental EDS analysis (Table 4.1), a lack of Cu dissolved in Ti_2Ni precipitates is observed when compared to the Cu content of the alloy. For that reason, Ti-Ni-Nb pseudoternaries with fixed amounts of Cu of 5at% and 10at% were calculated at 950°C and are presented in Figure 6-7-a and -b. The liquid phase is observed in regions with low Cu and Nb contents in Figure 6-7-a, as limited by red lines. When the Cu content is 10at%, the liquid region at 950°C is much

decreased (Figure 6-7-b) but is still present. The liquid phase can be related to the Ti_2Ni stability region at lower temperatures, as illustrated in pseudoternaries at 900°C in Figure 6-7-c and -d. Thus, even though the calculated melting point of the Ti_2Ni phase based on the mean element contents obtained by EDS was 975°C, the liquid phase is thermodynamically stable considering chemical segregations within this intermetallic phase. In cold-rolling procedures, the brittle behavior of Ti_2Ni could be noted both in Nb10-CR and Nb8-CR-IT whereas β-Nb deformed with the TiNi matrix.

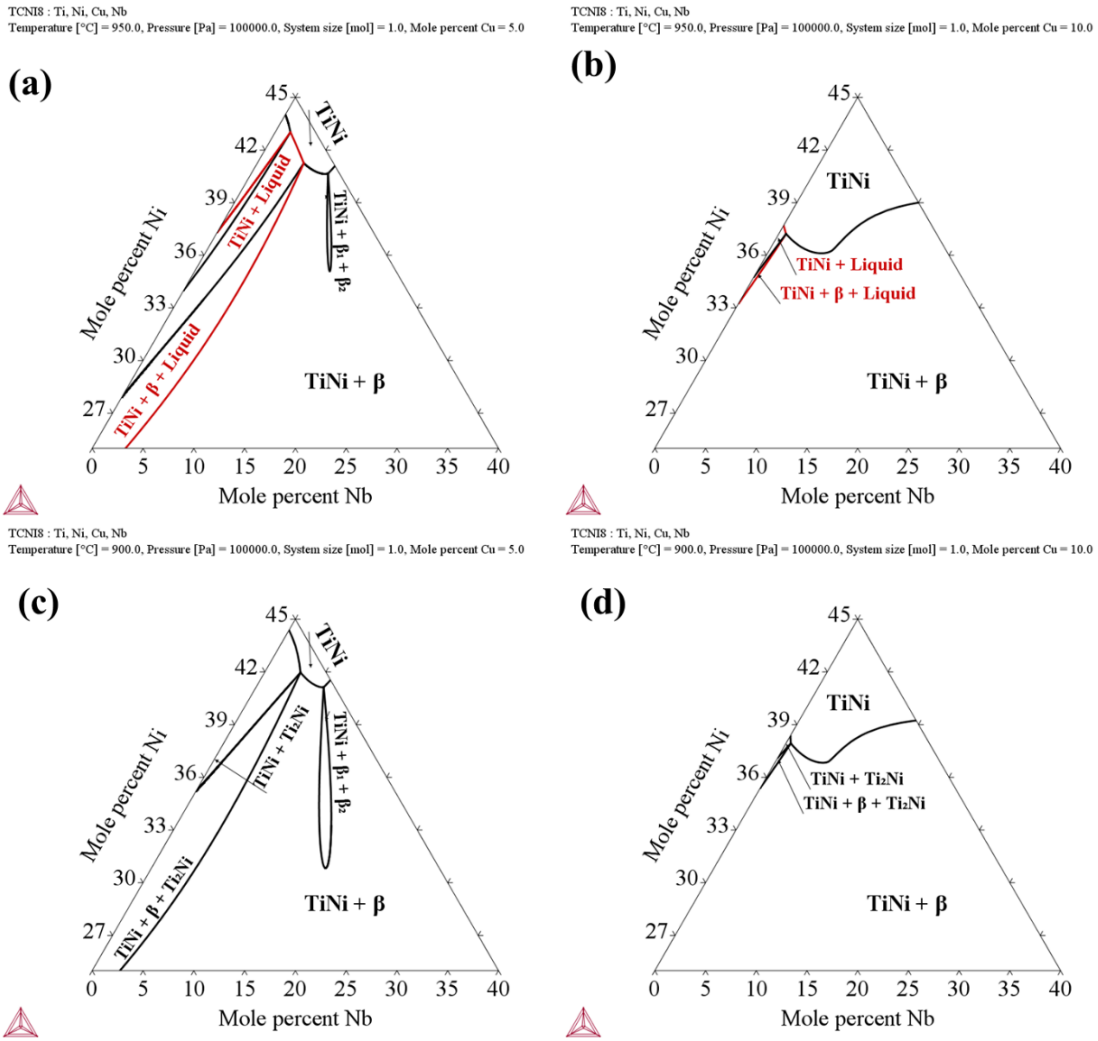

Figure 6-7 - TiNiNb pseudoternary phase diagrams at (a,b) 950°C and (c,d) 900°C with (a,c) 5 at% Cu and (b,d) 10 at% Cu

6.4.2. Characterization of the processed alloys

The overall hardness of Nb6-AC and Nb6-HR showed a small decrease in the alloy's mechanical resistance. In turn, the highest frequency of dynamic hardness in the ultramicrohardness test occurred between 300 and 400 DHT in Nb6-AC and between 200 and 300 DHT in Nb6-HR. These measurements might be related to the matrix phase condition, since this is the predominant phase, indicating the softening of the TiNi phase. Furthermore, no relevant elongation of the structure in the rolling direction was noted, as it can be observed in Figure 6-8. These results indicate the occurrence of dynamic restoring mechanisms.

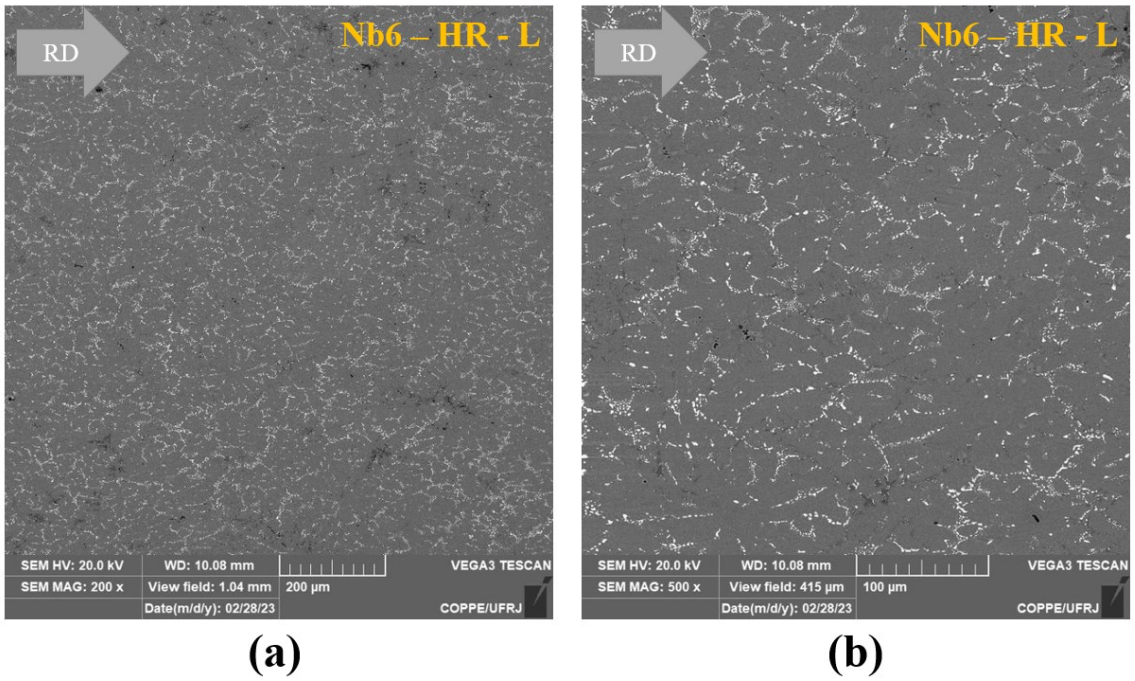

Figure 6-8 – BSEI of the longitudinal section of hot-rolled Nb6 alloy at (a) 200X and (b) 500X magnifications.

The hot-rolling process was not sufficient to achieve homogeneous mechanical properties and transformation behavior. The coalescence of second-phase particles makes the effect of Ti_2Ni and β-Nb phases more relevant, which may be responsible for the disperse dynamic hardness and elastic modulus distributions observed in the Nb6-HR. Furthermore, differences on the local chemical composition of the TiNi phase close to and far from coalesced second-phase particles and on the deformation and hardening/softening mechanisms occurring in the matrix

phase subjacent to phases that present distinct mechanical behavior may happen. As a result, the martensitic transformation can occur at different temperatures according to the region of the TiNi matrix.

In the cold rolled alloys, strain hardening of Nb10-CR was observed as a significant increase in the mean hardness, which was accompanied by a decrease in the standard deviation. In Nb8-CR-IT, the increase in the hardness level was much decreased. Hence, it appears that the intermediate heat-treatments were effective in recovering from hardening mechanisms taking place during cold-rolling.

6.5. Conclusions

In this chapter, the effect of different thermomechanical processes on the microstructure and hardness of cast TiNiCuNb alloys was evaluated, and some limitations and challenges have been noted. The following observations were made:

- Hot-rolling resulted in the coalescence of Ti_2Ni particles and β-Nb lamellae of the as-cast alloy. Voids were observed within coalesced Ti_2Ni particles, which was associated with the formation of liquid phase and solidification shrinkage.
- Fine Nb-rich precipitates were observed within the TiNi matrix of the alloys submitted to hot-rolling and intermediate heat-treatments during cold-rolling. This precipitation was related to a matrix phase supersaturated in Nb resultant from the casting procedure.
- A slight decrease of hardness was observed in the hot-rolled alloy, indicating the occurrence of restoring mechanisms. However, dynamic ultramicrohardness measurements showed increased heterogeneous properties in the processed material, which was related to the second phase coalescence. Heterogeneities were also observed in the reversible martensitic transformation promoted in DSC tests.
- During cold-rolling, Ti_2Ni particles present brittle behavior, as a significant number of cracks were observed in this phase.
- A true deformation of -0.29 is enough to cause strain hardening, by increasing 29% in the mean hardness in Nb10.
- Intermediate heat-treatment at a homologous temperate of 0.64 was effective to decrease the alloy's work hardening.

Thus, the Ti_2Ni coalescence, which leads to heterogeneous transformation and mechanical properties, and formation of liquid limits hot-working temperature of this alloy. During cold rolling, moderate strains are sufficient to produce work-hardening and intermediate heat-treatments can be used to control cold deformation.

7. EFFECT OF SUCTION CASTING AND EVALUATION OF POTENTIAL ELASTOCAROLIC USE OF A TiNiCuNb ALLOY

7.1. Introduction

Thermomechanical processing was not effective in optimizing the microstructure of the developed alloys, requiring further experimental testing. Alternatively, the focus in this chapter is to optimize the microstructure during alloy casting using a fast-cooling solidification process. Fort that, a $Ti_{48}Ni_{38}Cu_{10}Nb_4$ alloy was produced via arc melting followed by vacuum-suction casting. The microstructure and martensitic transformation behavior of the suction-cast alloy was compared with the conventional-cast alloy. The potential of the alloy produced via fast-cooling vacuum-suction casting (SC) for use as an elastocaloric material was evaluated.

7.2. Experimental procedure

A $Ti_{48}Ni_{38}Cu_{10}Nb_4$ ingot (30 g, composition in atomic percent) was produced via arc melting under a controlled argon atmosphere in a water-cooled copper mold. The ingot was remelted six times and flipped after each remelting step. A sample in the conventional casting (CC) condition was obtained for further microstructural characterization. The remaining ingot was remelted and solidified via vacuum-SC in a cylindrical water-cooled copper die with a cylindrical cavity, resulting in 5 mm diameter piece of 120 mm length which constituted the SC condition. Ingots in CC and SC conditions are illustrated in Figure 7-1. ThermoCalc (2018b) software with equilibrium and Scheil calculators and the TCNI8 v8.1 database was used to perform thermodynamic simulations.

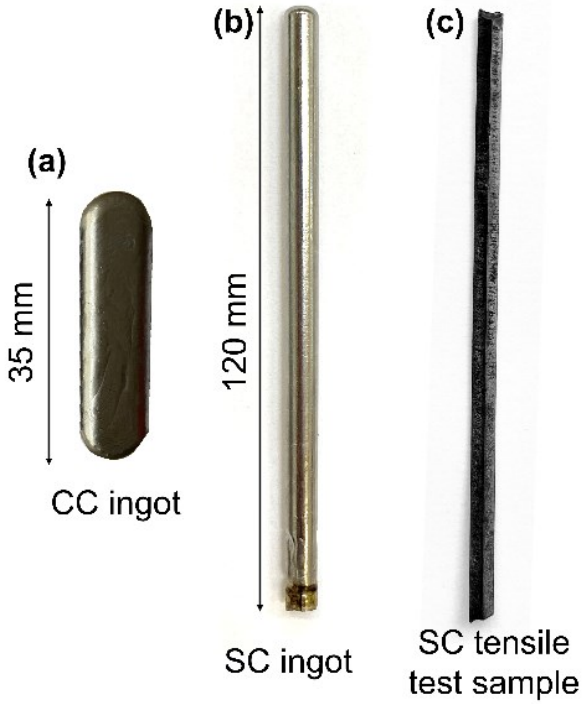

Figure 7-1 – Ingots in the (a) conventional-cast and (b) suction-cast conditions; (c) tensile test sample obtained from the suction-cast ingot.

Samples prepared by the CC and SC procedures were cut, mounted, ground, and polished for metallographic analyses using an FEI Inspect S50 scanning electron microscope (SEM) in the backscattered electron (BSE) mode. X-ray diffraction (XRD) was employed for phase identification. The XRD measurements were performed using a PANalytical PW1710 diffractometer with Cu-Kα radiation in the 2θ range from 30° to 110° and at a scan speed of 0.02°/s.

Differential scanning calorimetry (DSC; Shimadzu DSC60) was performed to evaluate the transformation temperatures and enthalpies. The thermal cycle consisted of heating and cooling the sample from -100 °C to 100 °C and 100 °C to -100 °C, respectively, at ± 10 °C/min. The direct and reverse martensitic transformation enthalpies were obtained from the integrated peak areas.

The functional behavior of the SC samples was examined by load/unload uniaxial tensile tests performed using an Instron 5582 universal testing machine. For that, the SC ingot was cut longitudinally by electrical discharge machining into four pieces of 90 mm length, as illustrated

in Figure 1-c. Samples with a gauge length of 30 mm were loaded to 1.5% strain and then unloaded to 7 MPa stress at two different strain rates. The first strain rate, 1.7×10^{-4} s^{-1}, is based on the crosshead speed limits for an isothermal test, as described in ASTM F2516 (176). The second strain rate, 2×10^{-3} s^{-1}, was used to perform consecutive load/unload cycles in a rapid manner and to obtain early information on the mechanical stability of the SC alloy. The integrated area of mechanical hysteresis was determined to evaluate the martensitic transformation work input. The effect of mechanical cycling on the reversible martensitic transformation of the SC alloy was evaluated by performing DSC tests on samples that were previously subjected to cyclic mechanical tests.

The potential of this alloy to be used as an elastocaloric component was assessed by calculating the ideal material coefficient of performance (COP_{mat}), which depends only on the alloy's martensitic transformation properties. This quantity is obtained according to the following equation (17,32):

$$\mathrm{COP_{mat}} = \frac{\rho \Delta \mathrm{H_{TM}}}{\mathrm{W_{TM}}} \qquad \text{Eq. 1}$$

The martensitic transformation enthalpy (ΔH_{TM}) was calculated from the average of the moduli of the direct (ΔH_d) and reverse (ΔH_r) transformation heats measured by DSC. The work input (W_{TM}) was acquired from the energy accumulated in the superelastic cycle, related to the mechanical hysteresis of the tensile test curve. The alloy density (ρ) was used for unit adjustment.

7.3. Results

7.3.1. Thermodynamic simulations

The volume fractions of the different phases obtained from the equilibrium calculation were plotted as a function of the temperature. As shown in Figure 7-2-a, TiNi is the predominant phase and up to 3 vol% of β-Nb is stable at temperatures lower than 800 °C. Considering the equilibrium composition variations in the solid phases formed at different temperatures during solidification, the phase stability as a function of the temperature and fraction of solid were obtained using the Scheil calculator. As shown in Figure 7-2-b, TiNi remains as the primary phase, whereas Ti_2Ni and β-Nb are also expected to form during solidification.

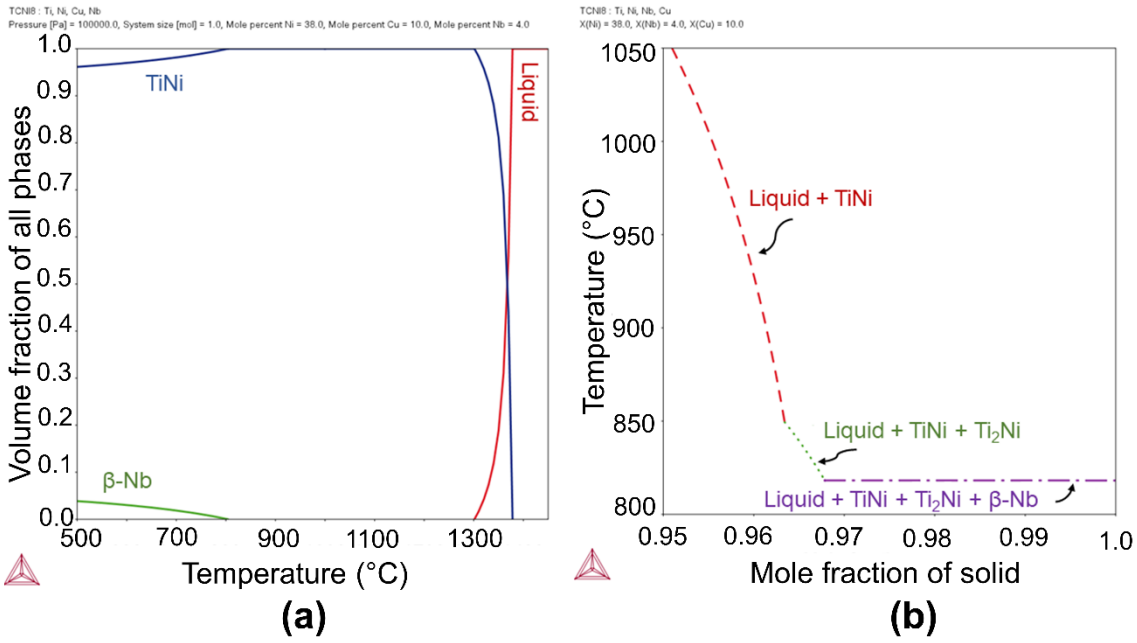

Figure 7-2 – Phase stability from the thermodynamic calculations obtained using the (a) equilibrium and (b) Scheil calculators.

7.3.2. Microstructural evaluation

B2 austenitic TiNi, β-Nb, and Ti_2Ni peaks were observed in the XRD patterns of both, the CC and SC, samples, whereas β-Ti was only found in the SC sample, Figure 7-3-a. The microstructures show a TiNi matrix and β-Nb appears as a eutectic constituent with TiNi phase, as pointed out in Figure 7-3-b and c. In the SC alloy, the two-phase constituent exhibits refined lamellae (Figure 7-3-e and -f). Ti_2Ni appears in the form of precipitates, which are frequently associated with the β-Nb phase in the CC sample (Figure 7-3b) and in the central region of the SC sample (Figure 7-3-d), where a smaller particle size and more uniform distribution are observed. β-Ti appears in the form of fine and dispersed precipitates in the SC alloy (Figure 7-3-c and -d), mainly in its border region, where Ti_2Ni particles are not present.

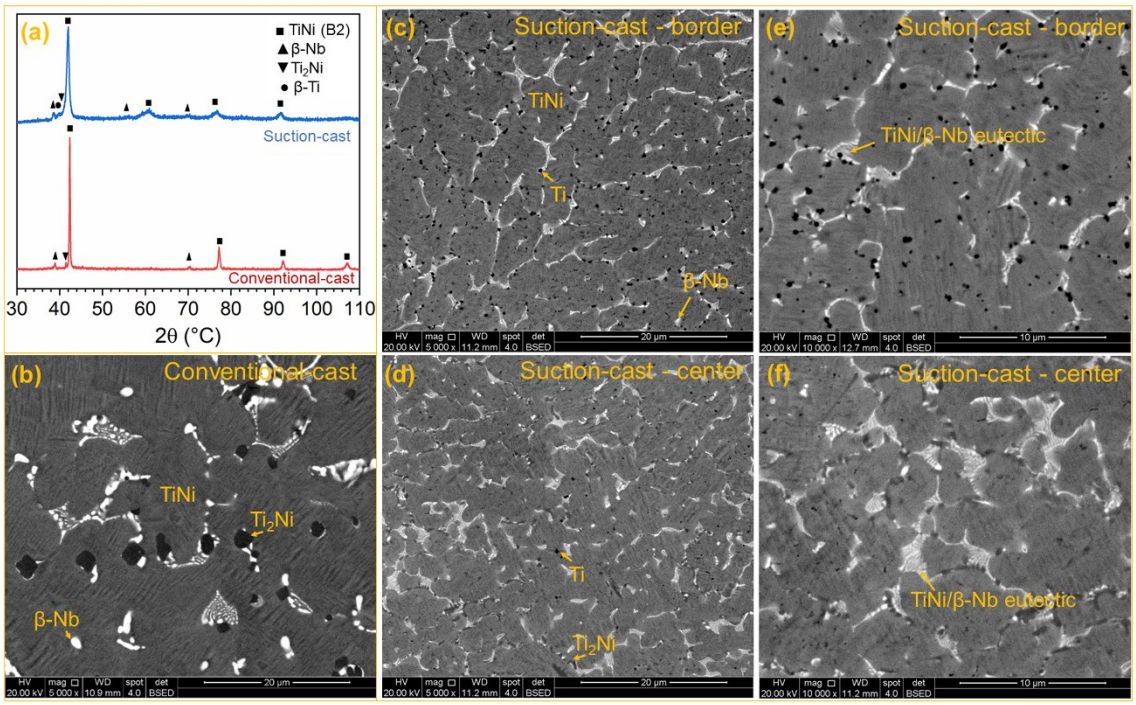

Figure 7-3 – (a) XRD patterns of the samples. BSE images of the (b) CC and (c) SC alloys in the border and (d) central regions of the ingots (5000×); details of the SC alloy in the (e) border and (f) central regions (10000×).

7.3.3. DSC analysis of the as-cast samples

The DSC thermograms of the CC and SC alloys are presented in Figure 7-4. In the CC sample (Figure 7-4-a), direct and reverse martensitic transformations occur within a wide range of temperatures and are characterized by the presence of two peaks. In the SC condition, single-step transformations and sharper peaks are observed (Figure 7-4-b). Meanwhile, the ΔH_{TM} of the CC alloy decreases from 7.4 to 5.8 J/g after SC.

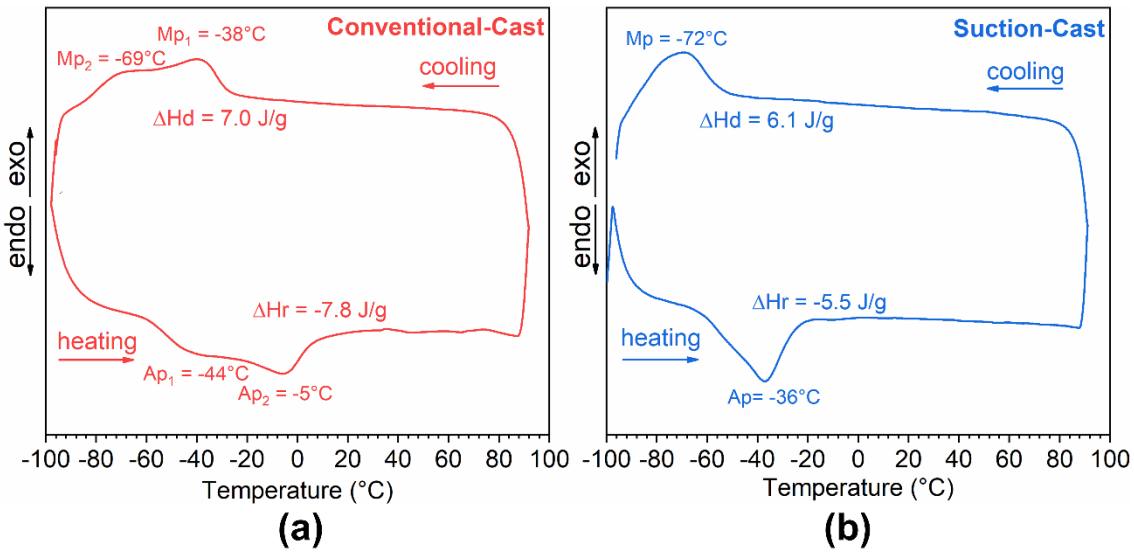

Figure 7-4 - DSC thermograms of the $Ti_{48}Ni_{38}Cu_{10}Nb_4$ alloys prepared under (a) CC and (b) SC conditions.

7.3.4. Loading/unloading tensile tests

In the isothermal loading/unloading tensile tests of the SC samples (Figure 7-5-a), superelastic behavior is observed, with a residual strain of 0.04% and work input, W_{TM}, of 886 kJ/m^3. The obtained W_{TM} is comparable to those previously achieved in SMAs cycled at low strains (49,177). In the cyclic test (Figure 7-5-b), performed subsequently, stable accumulated residual strains and decreases in W_{TM} were soon observed, as evidenced in Table 7.1. The difference between the work input on a mechanical cycle and the previous one diminishes rapidly with increasing number of cycles, leading to a significant convergence of this value as the results for the final few stress-strain curves overlap (inset of Figure 7-5-b). A W_{TM} of 144 kJ/m^3 was reached in the final mechanical cycle. Based on the calorimetric test results of the cycled sample (Figure 7-5-c), a transformation enthalpy of 5.3 J/g is obtained.

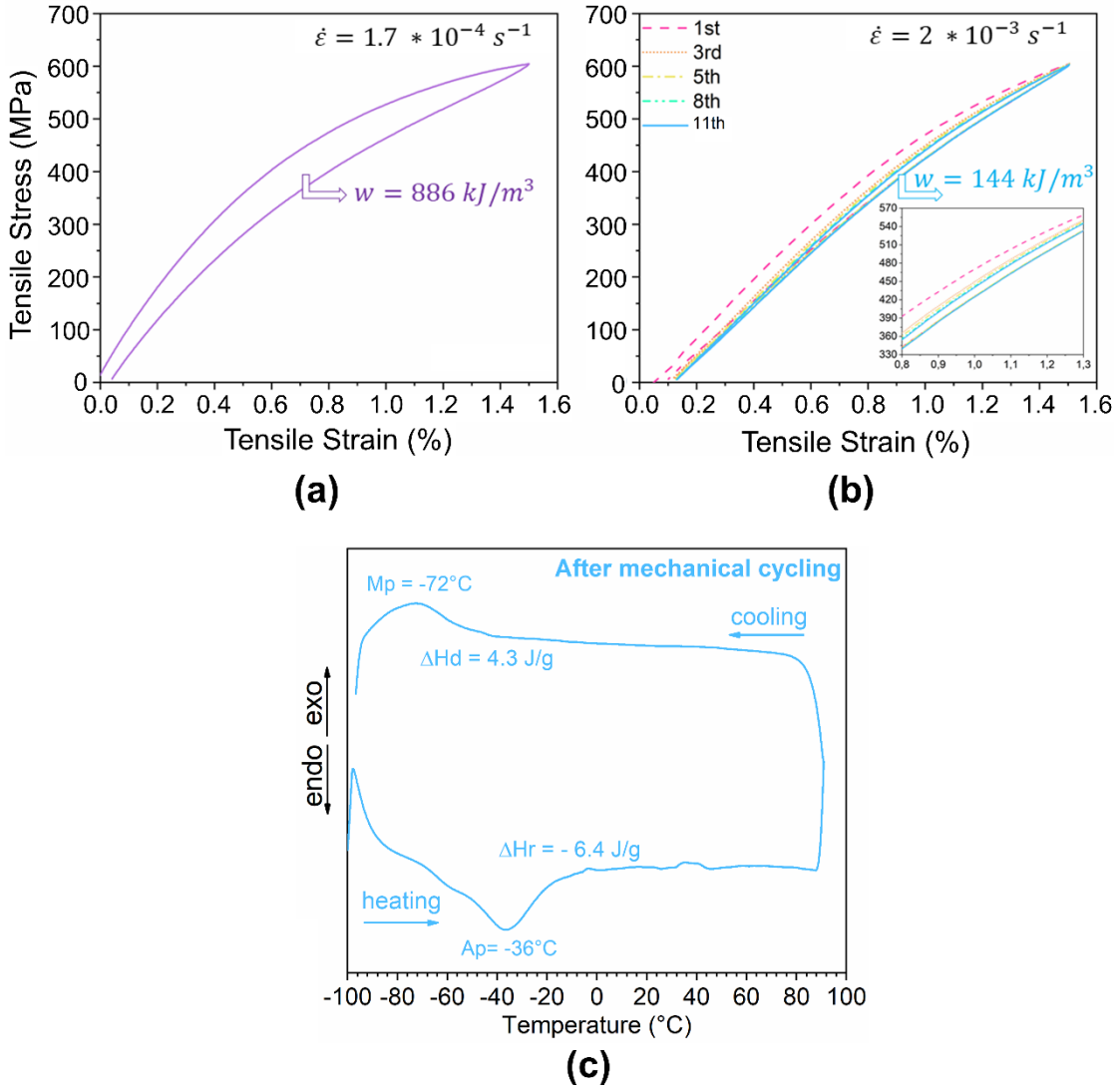

Figure 7-5 - Results of load/unload tensile tests performed on the SC samples at (a) 1.7 × 10^{-4} s^{-1} and (b) 2 × 10^{-3} s^{-1}; (c) DSC thermogram of the SC alloy after the mechanical cyclic load/unload tests.

Table 7.1. – Effect of mechanical cycling in the martensitic transformation work input

Cycle	W_{TM} (kJ/m³)	$\frac{W_{TM}^{n} - W_{TM}^{n-1}}{W_{TM}^{n}}$ (%)
Isothermal	886	
1	516	-41,8
2	284	-45,0

3	225	-20,8
4	198	-12,0
5	178	-10,1
6	168	-5,6
7	161	-4,2
8	156	-3,1
9	149	-4,5
10	146	-2,0
11	144	-1,4

7.4. Discussion

Different casting and additive manufacturing procedures have been applied to produce TiNi and TiNi-based alloys with refined and nanocrystalline structures (178–180). These structures have been associated with a decrease in thermal hysteresis (117), uniform martensitic transformation (180), longer fatigue life, better transformation stability, and higher COP (64,181). In this study, the effect of suction casting was evaluated in a $Ti_{48}Ni_{38}Cu_{10}Nb_4$ alloy for potential elastocaloric use.

The phase constitution of the CC sample (TiNi, β-Nb and Ti_2Ni) is qualitatively consistent with that from thermodynamic simulations obtained using the Scheil calculator, suggesting that the formation of second phase occurs from the liquid phase, as previously discussed in Ref. (182,183), chapters 4 and 5 . The β-Ti phase appears in the suction-cast alloy, mainly in its border region, where the partial suppression of Ti_2Ni was also observed. In comparison with the CC alloy, where the only Ti-rich phase identified was Ti_2Ni, it appears that high cooling rates, such as those in the SC material, inhibit the development of Ti_2Ni and the formation of β-Ti occurs instead. Finally, the vacuum-SC process produces a much finer and more uniform phase distribution because of the faster cooling conditions.

The transformation peak characteristics of the CC sample can be a result of chemical heterogeneities within the TiNi matrix phase resulting from the casting process. In contrast, the

sharper DSC peaks of the SC alloy suggest the existence of a homogeneous element distribution from this type of processing. In turn, the slight decrease in the ΔHTM after SC may be due to a lower amount of the TiNi phase in this structure. The TiNi phase fraction was qualitatively determined for a comparative analysis by integrating the areas under the XRD peaks of this phase and dividing them by the sum of all the integrated peak areas. This calculation yielded volume fractions of 88% and 82% in the CC and SC conditions, respectively, supporting the previous hypothesis.

In terms of the potential cooling efficiency, an ideal material COP_{mat} of 44.5 was obtained using Eq. 1, the work input from the isothermal characterization (1.7×10^{-4} s^{-1}), ΔH_{TM} for the as-suction-cast sample, and the calculated density (6.8 g/cm^3). Compared with the literature results (Table 7.2), the ideal COP_{mat} achieved in this study indicates that the development of TiNiCuNb alloys via a fast-cooling process is promising for elastocaloric applications. Using the work input obtained in the cycled condition and the corresponding ΔH_{TM}, a COP_{mat} of 253 is calculated. In this case, the loading/unloading superelastic cycles resulted in an increase in the COP_{mat} owing to the significantly lower transformation work input.

Table 7.2. – Comparison of the COP_{mat} values obtained from the literature with that in this work.

Alloy	**COP_{mat}**	**Ref**
Gradient-structured TiNi (ε = 1%)	36.0	(177)
Gradient-structured TiNi (ε = 4%)	10.0	(177)
Additive manufactured TiNi under compression	14.7	(184)
TiNi	7.7	(33)
TiNiCuCo	15.0	(33)
CuAlMn	13.3	(49)

TiNiCuNb	44.5	This work

Superelastic cycles have been previously reported (185–189) to result in the formation of dislocation substructures and residual stable martensite, to induce a preferable variant orientation and provide a more uniform behavior for reversible martensitic transformation. During cycling, higher transformation temperatures and lower transformation enthalpies have been observed with changes that occur more abruptly during the initial cycles and tend to stabilize in the subsequent ones (1,185–189). In this work, the observed convergence of the stress-strain superelastic curves and the transformation's work input, and the small difference observed in the transformation enthalpy can be attributed to the formation of only a few structural defects on the performed superelastic cycles. This could be a result of the predominance of the B2↔B19 transformation and the ease of interface movement associated.

7.5. Conclusions

Through vacuum-suction casting of a $Ti_{48}Ni_{38}Cu_{10}Nb_4$ shape memory alloy, a refined and uniform microstructure consisting of TiNi, β-Nb/TiNi eutectic, finely dispersed β-Ti, and Ti_2Ni phases was achieved. Based on the physical properties of the as-suction-cast alloy, an ideal COP_{mat} of 44.5 was obtained, indicating that this alloy is promising for use as an effective elastocaloric cooling material. A relevant convergence of the tensile stress-strain curves was obtained after few mechanical cycles, achieving a decreased work input of 144 kJ/m^3 and an increase in the coefficient of performance.

8. THERMOMECHANICAL PROCESSING OF SUCTION-CAST ALLOY

8.1. Introduction

In Chapter 7, the suction-casting (SC) process was used to optimize the casting procedure, obtaining a refined structure with promising COP_{mat} and superelastic stability. However, the stress required to induce the MT in the superelastic state depends on the work temperature in relation to Af according to Clausis-Clapeyron equation (4,10), presenting increasing values for higher temperatures. Thus, to obtain a smoother transformation behavior at room temperature, the low critical temperatures observed in Nb4-SC, 7.3.3, may be adjusted. In this chapter, the SC alloy was submitted to thermomechanical work for microstructural optimization, implemented according to the points discussed in Chapter 6. The use of a low-temperature heat-treatment after thermomechanical processing was assessed, aiming to tailor the MT temperatures and, additionally, increase transformation enthalpy, required for obtaining an enhanced COP.

8.1. Experimental Procedure

15g $Ti_{48}Ni_{38}Cu_{10}Nb_4$, at%, cylindrical ingots of 5mm diameter and ~20mm length ingots were prepared by SC. This alloy's melting temperature, calculated using single point equilibrium in ThermoCalc®, is 1378.3 °C. The thermomechanical process of the SC material consisted of hot-rolling into 2 mm thickness ribbons, cold-rolling to 1 mm thickness, and heat-treating. In the rolling steps, a 0.5 mm 304 austenitic stainless-steel sheet was used to envelope the samples.

Hot rolling was performed at 850°C, which was selected to avoid second-phase coalesce and localized melting, as pointed out in Chapter 6. This temperature corresponds to a homologous temperature, T_H, of 0.68. In this procedure, samples were heated for 10 min in a muffle furnace and submitted to 1 mm reduction in the first step and 0.5 mm in each following step with intermediate re-heating for 5 min. A total reduction of 3 mm was obtained, corresponding to 60% reduction and a true deformation of -0.92.

Hot-rolled (HR) samples were then submitted to cold rolling as follows. 3 steps of 0.2 mm reduction were performed with intermediate heat-treatments (HT) at 800°C ($T_H = 0.65$) for 10 min followed by air cooling. Then, 4 steps of 0.1 mm reduction were performed subsequently for strain hardening. The expected thickness of 1.4 mm after cold-rolling steps intercalated with

HR leads to a reduction of 30% and a total strain -0.36. The strain-hardening steps consisted of a reduction of 28.5% and a true strain of -0.34.

A cold-rolled (CR) sample was selected for microstructural analysis and then cut into 10 mm samples, which were submitted to HTs at different temperatures. Microstructural evaluation was performed by scanning electron microscopy (SEM) in a FEI Inspect S50 and a Versa FEG. The final low-temperature HTs were performed in a tubular furnace, with argon-controlled atmosphere at 450°C, 500°C, 550°C and 600°C for 30 min. Samples were water-cooled. From this moment forward, the as-suction cast condition will be referred to as SC; the laminated sample, HR and CR, will be named LAM; and, according to final HT temperature, samples will be called HT450C, HT500C, HT550 and HT600C.

XRD and DSC tests were performed for phase identification and martensitic transformation characterization, respectively. The XRD measurements were performed using a PANalytical PW1710 diffractometer with Cu-Kα radiation in the 2θ range from 30° to 90° at a scan speed of 0.02°/s. Relative integrated peak areas were used to qualitatively compare the phase fractions at different conditions. The thermal cycle in the DSC tests consisted of heating and cooling the sample from -100 °C to 100 °C and 100 °C to -100 °C, respectively, at ± 10 °C/min. Direct and reverse martensitic transformation enthalpies were obtained from the integrated peak area, temperature hysteresis was calculated by |Ap – Mp| and the reverse transformation ending temperature, Af, was obtained by the tangent line method.

The mechanical characterization of HT samples was assessed by microhardness measurements. These were made using Vickers indenter under 1000g load, with indentation time of 20s. ANOVA OneWay analysis was performed to obtain mean hardness and determine if these values are statistically different for samples with different HT temperatures.

8.2. Results

Backscattered electrons imagens (BSEI) for samples in the SC and LAM conditions are presented in Figure 8-1. As expected from previous results, Chapters 4 and 6, the present phases were maintained after thermomechanical processing, Figure 8-1-b', and the precipitation of fine β-Nb particles occurred within TiNi grains, as highlighted in the index image in Figure 8-1-b". In turn, it can be noted that the performed processing route was effective to produce deformation with no second-phase melting, coalescence or cracking.

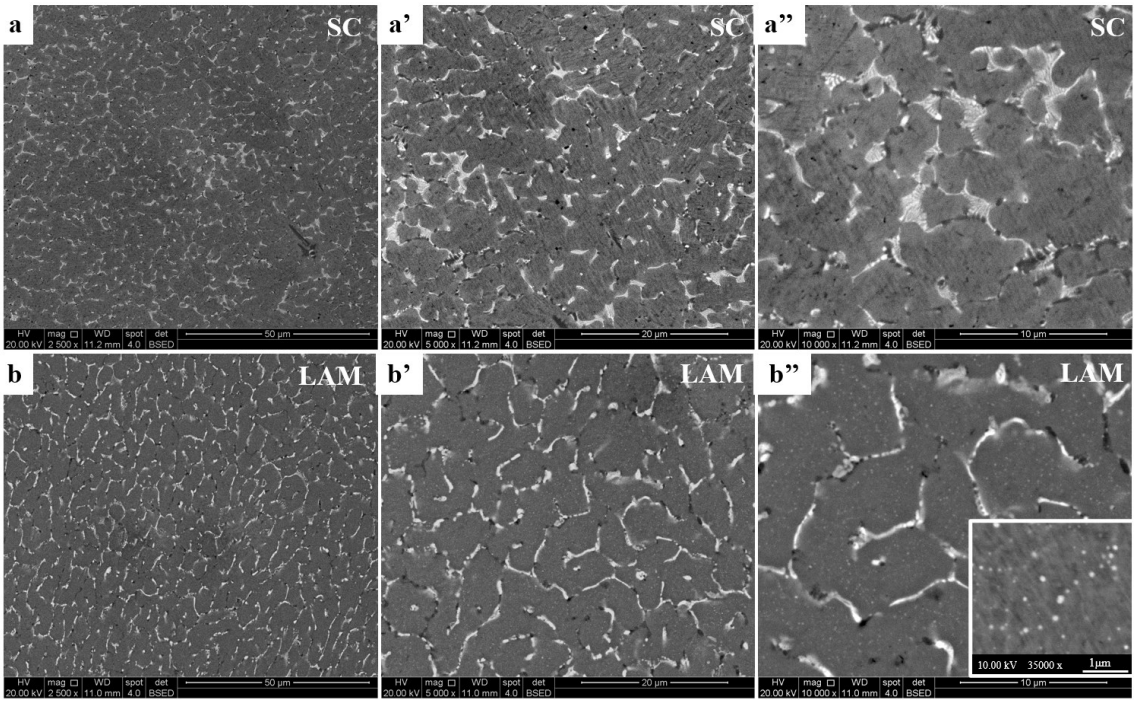

Figure 8-1 – BSEI of $Ti_{48}Ni_{38}Cu_{10}Nb_4$ alloy in the (a) SC and (b) thermomechanically processed (LAM) conditions.

The XRD patterns and DSC charts for samples in different processing steps are presented in Figure 8-2-a and -b, respectively. Because of the coincidence between the main peaks of B2 CsCl austenite and B19 orthorhombic martensite as well as the enlargement of the peaks' widths after thermomechanical processing, the dissociation of these two TiNi phases becomes difficult. Thus, indexation of XRD peaks was done by associating diffraction patterns to DSC charts, considering the stability of the TiNi structure at room temperature related to the MT temperatures. In SC, the B2 austenitic phase is identified, in accordance with its low MT temperatures. The main second phase present is β-Nb, which can be seen as the white phase in the BSEI (Figure 8-1).

From the calorimetric results, no events are observed in LAM while the performed low-temperature HTs were effective to regain the reversible MT. When assessing the measured Afs, plotted in Figure 8-3-c, a majorly austenitic structure at room temperature is expected in HT450C. In HT500C and HT550C, austenite and martensite are stable whereas HT600C is

basically constituted by B19 martensite. Furthermore, β-Nb's diffraction peaks are noted to become more pronounced after the final HTs are performed.

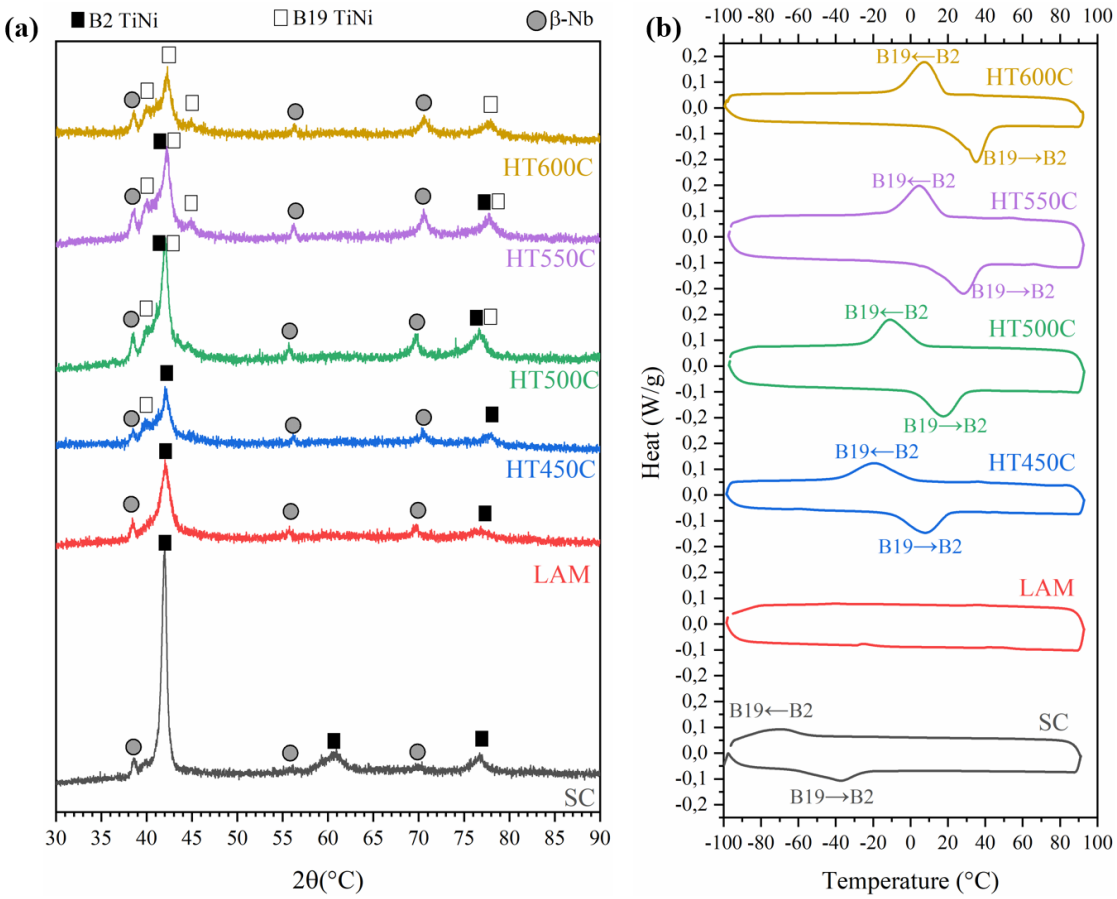

Figure 8-2 – (a) X-ray diffraction patterns and (b) DSC charts for $Ti_{48}Ni_{38}Cu_{10}Nb_4$ alloy in the SC, thermomechanically processed (LAM), and heat treated at different temperatures (HT450C, HT500C, HT550C, HT600C), conditions.

The effect of different HT temperatures on the MT peak temperatures (Ap, Mp), thermal hysteresis (|Ap-Mp|), Af, and enthalpy (ΔH_{TM}) is presented in Figure 8-3-a, -b, -c and -d, respectively. Compared to SC, which presented Ap of -36°C, Mp of -72°C, and a ΔH_{TM} of 5.8 J/g, as discussed in 7.3.3, increases in the MT critical temperatures and enthalpy were successfully achieved in the fully processed alloys. After different HTs, a linear increase in Af is observed with increasing HT temperature, Figure 8-3-c. ΔH_{TM} also increased, but a tendency to stabilization appears in HT600C whereas a random variation was observed in the transformation hysteresis.

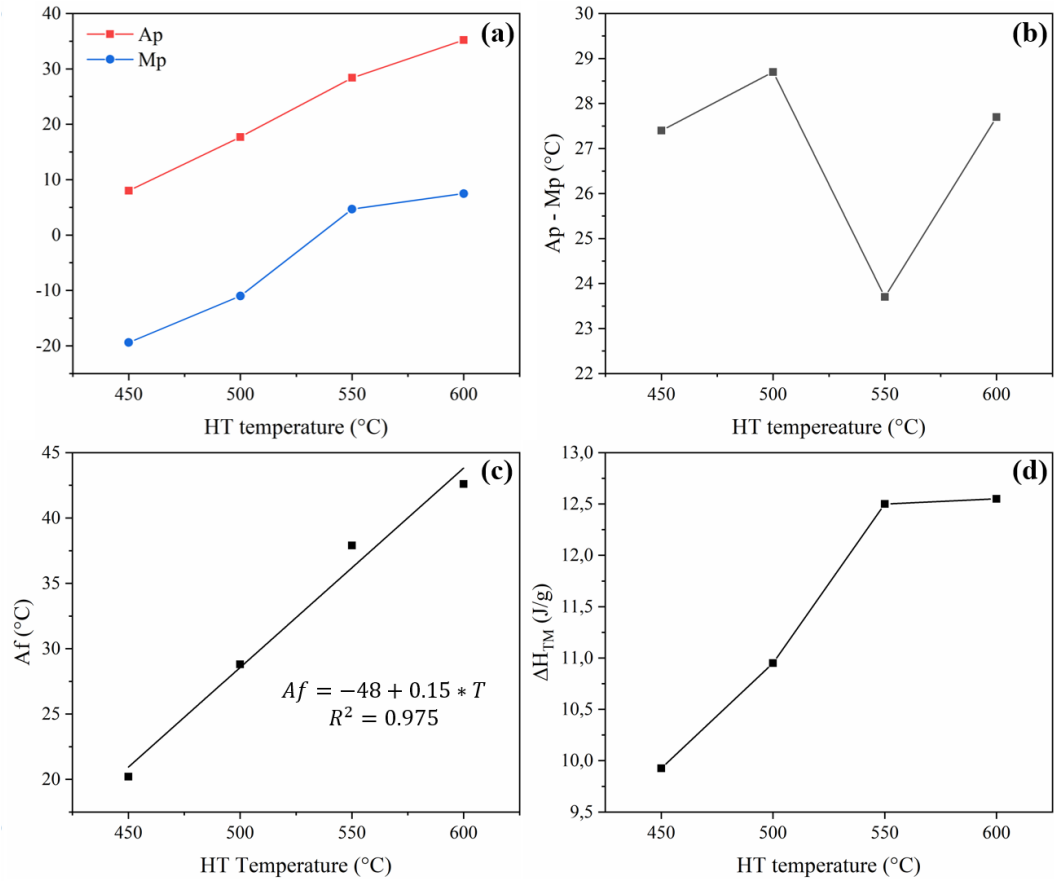

Figure 8-3 – (a) Direct (Mp) and reverse (Ap) martensitic transformation peak temperatures, (b) thermal hysteresis; (c) reverse transformation ending temperature (Af), and (d) transformation enthalpy as a function of HT temperature obtained by DSC tests.

The mean values obtained for the microhardness measurements in each HT condition are presented in Figure 8-4. These values are significantly different from each other at the 0.05 level according to the ANOVA Oneway analyses and a linear decrease of hardness was observed with increasing HT temperature.

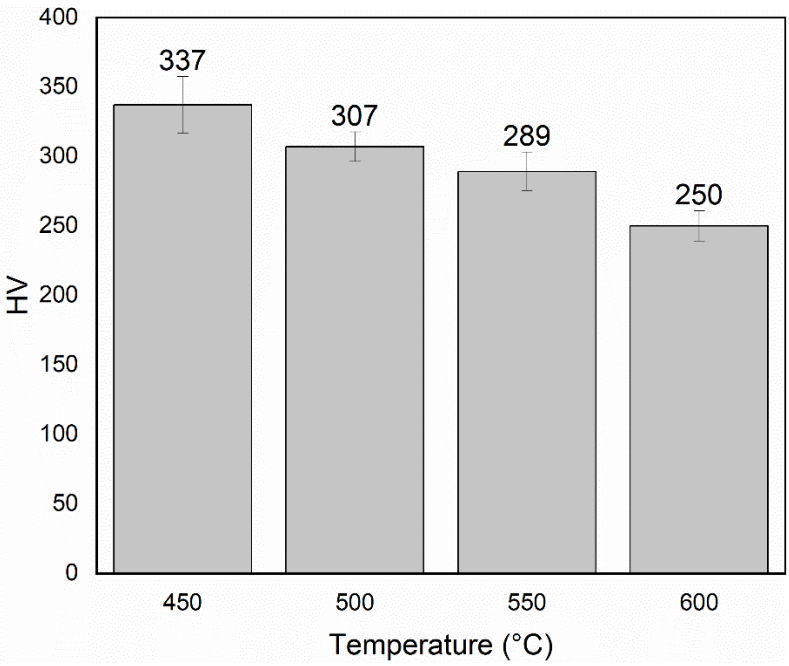

Figure 8-4 – Mean microhardness values as a function of HT temperature

8.3. Discussion

The fast-cooling solidification related to the SC process can lead to a high density of dislocations and supersaturation of Nb in the TiNi matrix. This microstructure presents a low-temperature MT. The thermomechanical processing route performed in the present chapter was effective to achieve a refined microstructure with optimized functional properties and a smoother MT. This may have been possible thanks to the use of proper processing conditions in association with the initial refined SC microstructure characteristics. During thermomechanical processing, Nb precipitated into fine β-Nb particles within the TiNi phase whereas changes in dislocation density and arrangements are expected.

On one hand, dislocations can affect the MT by acting as a resistance to the lattice distortion and the presence of tangled dislocations results in decreasing MT temperatures or even inhibit it, such as in the cold-rolled condition, LAM. When dislocation rearrangement takes place, forming cells or substructures around a low-density dislocation area, a smoother transformation behavior occurs. On the other hand, the chemical composition of the TiNi matrix phase also has strong impacts in the MT temperatures. This effect is well known in near-equiatomic TiNi with excesses of Ni (10). In the present study, the Nb dissolved in TiNi can also be responsible

for the delay in the MT's shearing mechanism in SC. Hence, these two contributions will be discussed from indirect evaluations of the HT alloys.

The final low-temperature HTs were performed to promote changes that resulted in lower hardness with increasing HT temperature and favored the MT, which was regained after this step. With increasing HT temperature, both decreases in the alloy's hardness and increases in the MT temperatures were observed, meaning that conditions of lower mechanical strength and smoother MT are obtained. This is an indication of the evolution of recovery/recrystallization mechanisms favored at higher temperature, leading to a gradual dislocation rearrangement and lower density.

In turn, the precipitation of β-Nb can be related to lower Nb contents in the TiNi matrix. A comparative analysis by the integrated XRD peak areas showed increases in the β-Nb fraction from 8% in SC to 11% in LAM. While the effect of withdrawing Nb from the matrix could not be seen before the final HT, when the effect of tangled dislocations in inhibiting the MT appears to be predominant, nanoprecipitation should not be discarded in the low-temperature HTs. A volume fraction of β-Nb of 16% was calculated in HT600C, where the highest Af was measured. This is a ductile phase which could also contribute to lower hardness with increasing HT temperatures.

The effect of Nb content in TiNi on Af was previously discussed in Topic 3.3.2.3, where a thermodynamic evaluation of the results obtained by Jiang *et al.*, 2015 (135) in heat-treatments at 400°C, 500°C, 600°C, 700°C and 800°C of a $(Ti_{50}Ni_{38}Cu_{12})_{93}Nb_7$ alloy was performed. The Nb content in the matrix phase depends on the Nb solubility in TiNi, which diminishes as temperature decreases, and the precipitation kinetics of β-Nb, favored at higher temperatures. In Ref. (135), an increase in Af from 400°C to 500°C was observed whereas decreases from 600°C to higher temperatures could be noted. Like the heat-treatments below 600°C by Jiang *et al.*, the kinetic factor seems to be predominant in HTs performed in this study, and precipitation might be relevant only at the higher used temperatures, while it is limited at lower temperatures. This would result in higher Nb contents in the TiNi matrix, and, subsequently, lower measured Ap and Mp, for lower HT temperatures.

In this manner, both the evolution of the recovery process with increasing HT temperature and the precipitation of β-Nb could contribute to how thermomechanical processing and variation

of HT temperature affects Ti-Ni-Cu-Nb alloys. Further studies are required to determine the mechanisms properly. However, it has been shown that these are heat-treatable alloys, which properties can be optimized and tailored by proper thermomechanical treatment, as the resulting behavior from the complete thermomechanical treatment was smoother MTs occurring at temperatures close to room temperature, with increased enthalpy.

8.4. Conclusions

Thermomechanical processing of the $Ti_{48}Ni_{38}Cu_{10}Nb_4$ suction-cast alloy was performed, considering the points listed in Chapter 6. The performed steps were effective to achieve deformation with no second-phase coalescence, melting or cracking. By hot-rolling, cold-rolling and heat-treating at low temperatures, it was possible to adjust the martensitic transformation peak temperatures.

Varying heat-treatments temperature altered MT critical temperatures and enthalpy, indicating that these are heat-treatable alloys. Both Af and ΔH_{TM} increased with increasing HT temperature. Alterations in these values due to thermomechanical processing and heat-treatments was discussed to be related to the effect of Nb dissolved in TiNi matrix, which appears to delay the occurrence of the reservable MT and lead to lower Afs, and the stage of recovery and recrystallization processes.

An Af smaller than, but close to, room temperature was achieved after heat-treating at 450°C for 30 min and water cooling, which can favor a smooth reversible martensitic transformation during superelastic cycling. An increase in the transformation's enthalpy from 5.8 J/g to 9.9 J/g was obtained after this heat-treatment, enabling higher COPs than those obtained in SC due to larger possible heat exchanges. From the perspective of electing a condition for further studies of an alloy that could present elastocaloric effect for room temperature applications, this should be the one selected.

9. FINAL CONSIDERATIONS

9.1. Summary of Results and Conclusions

In the present thesis, Ti-Ni-Cu-Nb alloys were designed, cast and explored, aiming to obtain an efficient and stable material for prospective use in solid state cooling. An extensive thermodynamic study using CALPHAD was used to assess different interactions within the Ti-Ni-Cu-Nb system. The $Ti_{52}Ni_{38}Cu_{10}$ base alloy was selected for adding Nb as a substitute for Ti because, in these alloys, thermodynamic calculation results showed the possibility of obtaining high fractions of TiNi phase with the precipitation of β-Nb. The TiNi phase undergoes reversible martensitic transformation, which is responsible for superelastic behavior and the elastocaloric effect. In turn, the β-Nb is expected to favor cold-formability and was associated with variations in the chemical composition of the matrix phase which might lead to an effective use of heat-treatments to adjust martensitic transformation temperatures.

The selected alloys were cast with varying Nb contents, exhibiting TiNi as the primary phase. β-Nb appeared in a eutectic constituent with the TiNi matrix whereas Ti-rich particles, Ti_2Ni and Ti, were also observed. The presence of these second phases was related to Ti and Nb enrichments of the liquid phase during solidification, while higher Nb contents jeopardizers the formation of Ti_2Ni and favors β-Ti's. This complex phase constitution presented high stability during homogenization treatment and thermomechanical processing. However, stability of the martensitic transformation critical temperatures was observed in a few thermal cycles performed in the DSC tests.

A solidification study based on CALPHAD associated with experimental results led to the hypothesis that solidification starts with the formation of TiNi, when the liquid becomes enriched in Ti and Nb and impoverished in Ni. Excesses of Ti precipitate as Ti_2Ni and/or β-Ti, depending on the Nb content. The depletion of Ni and accumulation of Nb were related to the formation of the two-phase β-Nb/TiNi eutectic constituent and solidification ends with the occurrence of a three-phase β-Nb/Ti_2Ni/TiNi eutectic.

Thermomechanical processing by hot rolling at T_h = 0.77 was not effective to produce a homogeneous microstructure. Instead, coalescence of β-Nb and Ti_2Ni particles was observed, resulting in heterogeneous ultramicrohardness distribution and martensitic transformation behavior. This procedure was also limited by partial melting of the Ti_2Ni phase. During cold

working, Ti_2Ni particles presented brittle behavior while β-Nb deformed alongside the TiNi matrix. The need to use heat-treatments in between rolling steps was pointed out, as moderate strains are sufficient to produce work-hardening.

The suction casting process was then tested, aiming to optimize the as-cast microstructure. A refined and uniform phase distribution was achieved when compared to that of the alloy resultant from conventional arc-melting. Single-step reversible martensitic transformation appearing as sharp peaks, in contrast to the two-peak reversible transformation occurring within wide temperature intervals in the conventional cast material, was obtained. Superelastic cycles exhibited early convergence, indicating that a stable functional behavior can also be expected.

Considering the terms previously pointed out, thermomechanical processing of the suction-cast alloy was used to optimize the microstructure. As a result, latent heat can be increased, and martensitic transformation temperatures can be tailored with varying final low-temperature heat-treatments. Hypotheses that relate the effect of thermomechanical treatment to the Nb content in TiNi matrix and recovery/recrystallization mechanism have been proposed.

Hence, the TiNiCuNb system was investigated from the thermodynamic, phase stability and solidification aspects. The evolution of the cast microstructure during thermomechanical processing was evaluated and limitations were pointed out. A processing route involving suction casting was an alternative to obtain a refined and uniform solidification structure, resulting in relevant transformation enthalpy and superelastic stability. In this condition, deformation was achieved by hot and cold rolling steps with no second-phase coalescence, melting or cracking. Low-temperature heat-treatments were then successfully used to tailor martensitic transformation critical temperatures and enthalpy.

9.2. Original Contributions and Results Relevance

The Ti-Ni-Cu-Nb system is a promising Ti-Ni-Cu-based system to obtain SMAs with high thermal, functional and mechanical stability while maintaining relevant transformation enthalpy that has not been vastly explored. This thesis presents an early investigation on SMAs in this quaternary system, providing basic information on thermodynamics, phase stability and microstructural evolution during thermomechanical processing of TiNiCuNb shape memory alloys. Limitations encountered during thermomechanical processing were controlled by modifying the casting process to achieve microstructural refinement and suiting rolling

parameters. Promising transformation enthalpy and superelastic stability have been achieved and heat-treatments were shown to be effective for adjusting martensitic transformation enthalpy and temperatures.

9.3. Suggestions for Future Work

- Study alternative processing routes, exploring fast-cooling solidification methods and different metalworking processes, such as rotary forging followed by drawing, to achieve microstructural homogenization and optimization.
- Perform a refined study on the nanostructure of Ti-Ni-Cu-Nb alloys using transmission electron microscopy, TEM, to assess the effect of nanoprecipitation of β-Nb and dislocation substructures on the martensitic transformation at different heat-treatments. Evaluate the mechanical and functional behaviors of alloys heat-treated at different temperatures.
- Use synchrotron x-ray diffraction to explore the martensitic transformation, performing tests at varying temperatures.
- Evaluate elastocaloric properties at various maximum deformations, strain rates, and temperatures, to determine the adiabatic condition, optimum strain for superelasticity and the work temperature window for solid-state cooling applicability.
- Measure mechanical, functional and elastocaloric stability during superelastic cycles to contemplate the alloys' properties degradation.
- Evaluate the fatigue resistance of fully austenitic alloys. Determine how the presence of martensite in the working temperature affects the cyclic behavior and fatigue resistance.

CONSIDERAÇÕES FINAIS

Resumo dos Resultados e Conclusões

Na presente tese, ligas Ti-Ni-Cu-Nb foram desenvolvidas, fundidas e exploradas com o objetivo de se obter um material eficiente e estável para um possível uso em refrigeração no estado sólido. Simulações termodinâmicas pelo método de cálculo de diagramas de fases foram utilizadas para avaliar diferentes interações dentro deste sistema. A liga base $Ti_{52}Ni_{38}Cu_{10}$ foi selecionada para adição de pequenas quantidades de Nb no lugar do Ti uma vez que os cálculos termodinâmicos mostraram a possibilidade de se obter frações significativas de TiNi e precipitação de β-Nb. O TiNi é a fase que passa por transformação martensítica reversível, sendo responsável pelo comportamento superelástico e efeito elastocalórico. Por outro lado, espera-se que o β-Nb contribua para a formabilidade a frio ao mesmo tempo que variações em sua fração volumétrica e composição química refletem em variações na composição química da matriz, podendo levar ao ajuste das temperaturas de transformação martensítica por meio de tratamentos térmicos adequados.

Nas ligas fundidas, o TiNi foi de fato a fase primária. O β-Nb apareceu em um constituinte eutético com a matriz TiNi enquanto a precipitação de partículas ricas em Ti, Ti_2Ni e Ti, também foi observada. A presença dessas segundas fases foi relacionada a um enriquecimento de Ti e Nb no líquido durante a solidificação das ligas. Essa complexa constituição de fases apresentou alta estabilidade durante tratamento térmico de homogeneização e processamento termomecânico. Entretanto, observou-se a estabilidade das temperaturas críticas de transformação em ciclos realizados nos ensaios por calorimetria diferencial de varredura.

Um estudo de solidificação baseado no método de cálculo de diagramas de fases associado à resultados experimentais levou à hipótese que a solidificação das ligas fundidas tem início com a formação de TiNi, quando o líquido se torna enriquecido em Ti e Nb e empobrecido em Nb. Excessos de Ti precipitam como Ti_2Ni e/ou β-Ti, a depender do teor de Nb. O empobrecimento de Ni e acúmulo de Nb foram associados à formação de um constituinte eutético β-Nb/TiNi e a solidificação tem fim com a ocorrência de um eutético de três fases, β-Nb/TiNi/Ti_2Ni.

O processamento termomecânico por laminação a quente a uma temperatura homóloga de 0.77 não foi efetivo para produzir uma microestrutura homogênea. Ao invés disso, o coalescimento das lamelas de β-Nb e das partículas de Ti_2Ni foi observado, levando a uma distribuição de

ultramicrodureza e comportamento de transformação martensítica heterogêneos. Este procedimento foi limitado pelo coalescimento e fusão parcial de Ti_2Ni. Durante o trabalho a frio, os precipitados de Ti_2Ni apresentaram comportamento frágil enquanto o β-Nb se deformou junto à matriz TiNi. A necessidade de tratamentos térmicos entre cada passo de laminação a frio foi apontada, uma vez que deformações moderadas são suficientes para produzir encruamento.

A fusão seguida por solidificação por sucção à vácuo foi testada, visando-se obter uma otimização da microestrutura como-fundida. Uma distribuição refinada e homogênea de fases foi atingida em relação à liga fundida convencionalmente em forno elétrico à arco. Transformação martensítica reversível foi observada em um passo, aparecendo como picos agudos quando comparados aos presentes na liga convencional, caracterizada pela presença de dois picos em um amplo intervalo de temperatura. Um coeficiente de performance ideal do material promissor foi calculado pelo quociente da entalpia de transformação pelo trabalho de transformação medido pela área da histerese mecânica enquanto ciclos superelásticos convergiram rapidamente, indicando que um comportamento funcional estável também pode ser esperado.

Levando-se em consideração as limitações apontadas anteriormente, o processamento termomecânico da liga solidificada por sucção à vácuo foi realizado para otimização microestrutural. Como resultado, a entalpia de transformação pôde ser aumentada e as temperaturas de transformação martensítica foram ajustadas por meio de tratamentos térmicos finais de baixa temperatura. Foram propostas hipóteses que o efeito do tratamento termomecânico está associado ao teor de Nb na matrix TiNi e ao estágio de mecanismos de recuperação/recristalização.

Desta forma, o sistema Ti-Ni-Cu-Nb foi investigado das perspectivas de termodinâmica, estabilidade de fases e solidificação. A evolução microestrutura das ligas fundidas durante processamento termomecânico foi avaliada e uma rota envolvendo a solidificação por sucção à vácuo foi destacada para a obtenção de uma condição refinada e uniforme, resultando em uma entalpia de transformaçãol e estabilidade no comportamento superelástico promissores. Nesta condição, a deformação da liga foi obtida por laminação a quente e a frio, sem o coalescimento, fusão parcial ou trincamento de segundas fases. Tratamentos térmicos de baixa temperatura foram efetivos no ajuste das temperaturas críticas e entalpia de transformação. Entretanto,

foram encontradas dificuldades para reproduzir as condições de fusão e processamento termomecânico, que influenciam fortemente a transformação martensítica reversível. Da perspectiva do uso como material elastocalórico, uma vez que esses desafios forem superados, caracterização elastocalórica e testes de fadiga são necessários.

Contribuições Originais e Relevância dos Resultados

O sistema Ti-Ni-Cu-Nb é um sistema promissor baseado em Ti-Ni-Cu para se obter LMFs de alta estabilidade térmica, funcional e mecânica mantendo uma entalpia de transformação relevante que não foi amplamente explorado. Esta tese apresentou uma investigação inicial de LMFs deste sistema quaternário, fornecendo informações básicas a respeito do equilíbrio termodinâmico, estabilidade de fases e evolução da microestrutura durante processamento termomecânico. Limitações encontradas durante processamento termomecânico foram controladas por modificações promovidas na solidificação da liga, visando-se a obtenção de refinamento microestrutural, e nos parâmetros de laminação. Entalpia de transformação martensítica e estabilidade superelástica promissoras foram observadas enquanto tratamentos térmicos se mostraram efetivos no ajuste das temperaturas e entalpia de transformação martensítica.

Sugestões para Trabalho Futuro

- Estudar rotas de processamento alternativas, explorando métodos de solidificação com resfriamento rápido e diferentes processos de conformação mecânica, como forjamento rotativo seguido de trefilação, visando-se obter uma otimização e refinamento microestrutural.
- Realizar estudo de aprofundamento da nanoestrutura das ligas Ti-Ni-Cu-Nb por meio de microscopia eletrônica de transmissão, com o objetivo de avaliar o efeito de nanoprecipitação de β-Nb e subestruturas de deslocações em diferentes temperaturas de tratamento térmico final. Avaliar o comportamento mecânico e funcional de ligas tratadas em diferentes temperaturas.
- Utilizar difratometria de raios-x sincrotron para explorar a transformação martensítica, realizando medidas em diferentes temperaturas.

- Avaliar as propriedades elastocalóricas em diferentes deformações máximas, taxas de deformação e temperaturas visando a determinação da condição de deformação adiabática com superelasticidade completa e da janela de temperatura de trabalho.
- Medir a estabilidade mecânica, funcional e elastocalórica durante ciclagem superelásticas para avaliação da degradação de propriedades da liga.
- Avaliar a resistência à fadiga de ligas superelásticas austeníticas. Estudar como a presença de martensita na temperatura de deformação afeta o comportamento durante ciclagem mecânica e a resistência à fadiga.

10. REFERENCES

1. Otsuka K, Wayman CM. Shape Memory Materials. Cambridge. Cambridge University Press; 1998. 284 p.

2. Christian JW. Characteristics of Martensitic Transformations. In: Pergamon, editor. The Theory of Transformations in Metals and Alloys. Segunda. 2002. p. 961–91.

3. Roytburd AL. Principal Concepts of Martensitic Theory. Le Journal de Physique IV. 1995;05(C8):C8-21-C8-30.

4. Otsuka K, Ren X. Martensitic transformations in nonferrous shape memory alloys. Materials Science and Engineering A. 1999;273–275:89–105.

5. Wollants P, Roos JR, Delaey L. Thermally and stress-induced thermoelastic martensitic transformations in the reference frame of equilibrium thermodynamics. Prog Mater Sci. 1993;37:227–88.

6. Christian JW. Knetics of Martensitic Transformation. In: The Theory of Transformations in Metals and Alloys. 2002. p. 1062–75.

7. Feninat F El, Laroche G, Fiset M, Mantovani D. Shape Memory Materials for Biomedical Applications. Adv Eng Mater. 2002;4(3):91–104.

8. Olson GB, Cohen M. Thermoelastic Behavior in Martensitic Transformations. Scripta Metallurgica. 1975;9:1247–54.

9. Olson GB, Cohen M. Dislocation Theory of Martensitic Transformations. Nabarro FRN, editor. Cambridge, MA: Elsevier Science Publishers B.V.; 1986. 117 p.

10. Otsuka K, Ren X. Physical metallurgy of Ti–Ni-based shape memory alloys. Prog Mater Sci. 2005;50:511–678.

11. Buehler WJ, Gilfrich J V., Wiley RC. Effect of Low-Temperature Phase Changes on the Mechanical Properties of Alloys near Composition TiNi. J Appl Phys. 1963;34(5):1475–7.

12. Silva JD, Martins SC, Lopes NI de A, Resende PD, Santos LA, Buono VTL. Effects of aging treatments on the fatigue resistance of superelastic NiTi wires. Materials Science and Engineering A. 2019 May 22;756:54–60.

13. Otsuka K, Shimizu K. On the Crystallographic Reversibility of Martensitic Transformations. Scripta Metallurgica. 1977;11:757–60.

14. Goetzler W, Ashrae M, Zogg R, Ashrae M, Young JIM, Ashrae AM, et al. Alternatives to Vapor-Compression HVAC Technology. ASHRAE J. 2014;(October).

15. Kitanovski A, Plaznik U, Tomc U, Poredos A. Present and future caloric refrigeration and heat-pump technologies. International Journal of Refrigeration. 2015;7(57):288–98.

16. Pérez-Lombard L, Ortiz J, Pout C. A review on buildings energy consumption information. Energy Build. 2008;40(3):394–8.

17. OECD/IEA. The Future of Cooling - Opportunities for energy-efficient air conditioning [Internet]. 2018. p. 92. Available from: www.iea.org/t&c/

18. IEA. World Energy Outlook 2019 [Internet]. International Energy Agency. 2019. Available from: https://www.eia.gov/outlooks/aeo/pdf/aeo2019.pdf

19. Goetzler W, Zogg R, Young J, Johnson C. Energy Savings Potential and RD & D Opportunities for Non-Vapor-Compression HVAC Technologies [Internet]. US Department of Energy. 2014. p. 3673. Available from: http://www.osti.gov/home/

20. Fähler S, Röbler UK, Kastner O, Eckert J, Eggeler G, Emmerich H, et al. Caloric Effects in Ferroic Materials: New Concepts for Cooling. Adv Eng Mater. 2012;14(12):10–9.

21. Carmo JP, Silva MF, Ribeiro JF, Wolffenbuttel RF, Alpuim P, Rocha JG, et al. Digitally-controlled array of solid-state microcoolers for use in surgery. Microsystem Technologies. 2011;17(8):1283–91.

22. Mañosa L, Planes A, Bonnot E, Vives E, Romero R. The Use of Shape-Memory Alloys for Mechanical Refrigeration. Functional Materials Letters. 2009;2(2):73–8.

23. Tušek J, Engelbrecht K, Millán-solsona R, Mañosa L, Vives E, Mikkelsen LP, et al. The Elastocaloric Effect: A Way to Cool Efficiently. Adv Energy Mater. 2015;5:1–5.

24. Quarini J, Prince A. Solid state refrigeration: cooling and refrigeration using crystalline phase changes in metal alloys. Proc Inst Mech Eng C J Mech Eng Sci. 2004;218(10):1175–9.

25. Moya X, Mathur ND. Caloric materials near ferroic phase transitions. Nat Mater [Internet]. 2014;13(5):439–50. Available from: http://dx.doi.org/10.1038/nmat3951

26. Bonnot E, Romero R, Mañosa L, Vives E, Planes A. Elastocaloric Effect Associated with the Martensitic Transition in Shape-Memory Alloys. Phys Rev B Condens Matter Mater Phys. 2008;125901(March):1–4.

27. Tušek J, Pryds N. Cooling with a Squeeze. Physics (College Park Md). 2019;12(June).

28. Bechtold C, Chluba C, Miranda RL De, Quandt E, Bechtold C, Chluba C, et al. High cyclic stability of the elastocaloric effect in sputtered TiNiCu shape memory film. Appl Phys Lett. 2012;091903(101).

29. Planes A, Stern-Taulats E, Castán T, Vives E, Mañosa L, Saxena A. Caloric and Multicaloric Effects in Shape Memory Alloys. Mater Today Proc [Internet]. 2015;2:S477–84. Available from: http://dx.doi.org/10.1016/j.matpr.2015.07.332

30. Ossmer H, Chluba C, Krevet B, Quandt E, Rohde M, Kohl M. Elastocaloric cooling using shape memory alloy films. J Phys Conf Ser. 2015;012138(476):1–6.

31. Goetzler W, Shandross R, Young J, Petritchenko O, Ringo D, McClive S. Energy Savings Potential and RD&D Opportunities for Commercial Building HVAC Systems [Internet]. U.S department of Energy. 2017. Available from: http://www.osti.gov/servlets/purl/1419622/

32. Kirsch S marie, Welsch F, Michaelis N, Schmidt M, Seelecke S. NiTi-Based Elastocaloric Cooling on the Macroscale: From Basic Concepts to Realization. Energy Technology. 2018;6:1567–87.

33. Bruederlin F, Ossmer H, Wendler F, Miyazaki S, Kohl M. SMA foil-based elastocaloric cooling: From material behavior to device engineering. J Phys D Appl Phys. 2017;50(42).

34. Cui J, Takeuchi I. Compact thermoelastic cooling system. Vol. 2. 2019.

35. Engelbrecht K, Tu J, Eriksen D, Lei T. A regenerative elastocaloric device: experimental results. J Phys D Appl Phys. 2017;50.

36. Kabirifar P, Žerovnik A, Ahčin Ž, Porenta L, Brojan M, Tušek J. Elastocaloric Cooling: State-of-the-art and Future Challenges in Designing Regenerative Elastocaloric Devices. Journal of Mechanical Engineering [Internet]. 2019;65:615–30. Available from: https://www.sv-jme.eu/article/elastocaloric-cooling-state-of-the-art-and-future-challenges-in-designing-regenerative-elastocaloric-devices/

37. Kirsch, Schmidt M, Welsch F, Michaelis N, Schütze A, Seelecke S. Development of a shape memory based air conditioning system. 59th Ilmenau Scientific Colloquium [Internet]. 2017;(September):11–5. Available from: urn:nbn:de:gbv:ilm1-2017iwk-046:4

38. Radermacher R, Takeuchi I, Hwang Y, Wu Y, Qian S, Ling J. Solid-state heating or cooling systems, devices and methods. Vol. 2. 2018.

39. Qian S, Geng Y, Wang Y, Ling J, Hwang Y, Radermacher R, et al. A review of elastocaloric cooling: Materials, cycles and system integrations. International Journal of Refrigeration [Internet]. 2016;64:1–19. Available from: http://dx.doi.org/10.1016/j.ijrefrig.2015.12.001

40. Zemansky MW, Dittman RH. Heat and Thermodynamics. 7a ed. McGraw-Hill Book Company; 1997. 510 p.

41. Schmidt M, Kirsch S marie, Seelecke S, Schütze A, Schmidt M, Kirsch S marie, et al. Elastocaloric cooling: From fundamental thermodynamics to solid state air conditioning. Sci Technol Built Environ. 2016;22:474–88.

42. Sehitoglu H, Wu Y, Ertekin E. Elastocaloric effects in the extreme. Scr Mater. 2018;148:122–6.

43. Wu Y, Ertekin E, Sehitoglu H. Elastocaloric cooling capacity of shape memory alloys - Role of deformation temperatures, mechanical cycling, stress hysteresis and inhomogeneity of transformation. Acta Mater. 2017;135:158–76.

44. Nikitin SA, Myalikgulyev G, Annaorazov MP, Tyurin AL, Myndyev RW, Akopyan SA. Giant elastocaloric effect in FeRh alloy. Phys Lett A. 1992;171(3–4):234–6.

45. Annaorazov MP, Nikitin SA, Tyurin AL, Asatryan KA, Dovletov AK. Anomalously high entropy change in FeRh alloy. J Appl Phys. 1996;79(3):1689–95.

46. Annaorazov MP, Nikitin SA, Tyurin AL, Akopyan SA, Myndyev RW. Cooling scheme based on the AF-F transition in Fe-Rh alloys induced by tensile stress. Physica Status Solidi A Appl Res. 2002;194(1):304–14.

47. Cui J, Wu Y, Muehlbauer J, Hwang Y, Radermacher R, Fackler S, et al. Demonstration of high efficiency elastocaloric cooling with large ΔT using NiTi wires. Appl Phys Lett. 2012;073904(2012):27–31.

48. Gràcia-Condal A, Stern-Taulats E, Planes A, Vives E, Mañosa L. The Giant Elastocaloric Effect in a Cu–Zn–Al Shape-Memory Alloy: a Calorimetric Study. Phys Status Solidi B Basic Res. 2018;255(2):1–7.

49. Qian S, Geng Y, Wang Y, Pillsbury TE, Hada Y, Yamaguchi Y, et al. Elastocaloric effect in CuAlZn and CuAlMn shape memory alloys under compression. Philosophical Transactions of the Royal Society A: Mathematical, Physical and Engineering Sciences. 2016;374(2074).

50. Vives E, Burrows S, Edwards RS, Dixon S, Maosa L, Planes A, et al. Temperature contour maps at the strain-induced martensitic transition of a Cu-Zn-Al shape-memory single crystal. Appl Phys Lett. 2011;98(1).

51. Mañosa L, Jarque-Farnos S, Vives E, Planes A. Large temperature span and giant refrigerant capacity in elastocaloric Cu-Zn-Al shape memory alloys. Appl Phys Lett. 2013;211904(2013).

52. Xu S, Huang HY, Xie J, Takekawa S, Xu X, Omori T, et al. Giant elastocaloric effect covering wide temperature range in columnar-grained Cu71.5Al17.5Mn11 shape memory alloy. APL Mater [Internet]. 2016;4(10). Available from: http://dx.doi.org/10.1063/1.4964621

53. Yuan B, Zhu X, Zhang X, Qian M. Elastocaloric effect with small hysteresis in bamboo-grained Cu–Al–Mn microwires. J Mater Sci [Internet]. 2019; Available from: https://doi.org/10.1007/s10853-019-03592-8

54. Ossmer H, Lambrecht F, Gültig M, Chluba C, Quandt E, Kohl M. Evolution of temperature profiles in TiNi films for elastocaloric cooling. Acta Mater. 2014;81:9–20.

55. Pataky GJ, Ertekin E, Sehitoglu H. Elastocaloric cooling potential of NiTi, Ni2FeGa, and CoNiAl. Acta Mater [Internet]. 2015;96:420–7. Available from: http://dx.doi.org/10.1016/j.actamat.2015.06.011

56. Zhou M, Li Y, Zhang C, Li S, Wu E, Li W. The elastocaloric effect of Ni50.8Ti49.2 shape memory alloys. J Phys D Appl Phys. 2018;

57. Ossmer H, Chluba C, Gueltig M, Quandt E, Kohl M. Local Evolution of the Elastocaloric Effect in TiNi-Based Films. Shape Memory and Superelasticity. 2015;1(2):142–52.

58. Ding L, Zhou Y, Xu Y, Dang P, Ding X, Sun J, et al. Learning from superelasticity data to search for Ti-Ni alloys with large elastocaloric effect. Acta Mater. 2021 Oct 1;218.

59. Aaltio I, Fukuda T, Kakeshita T. A Perspective on Elastocaloric Effect in Ti – Ni-Based Shape Memory Alloys. Shape Memory and Superelasticity [Internet]. 2019;5(3):230–4. Available from: https://doi.org/10.1007/s40830-019-00229-2

60. Gall K, Maier HJ. Cyclic deformation mechanisms in precipitated NiTi shape memory alloys. Acta Mater. 2002;50:4643–57.

61. Zhang Y, Kang G, Miao H, Yu C. Cyclic degeneration of elastocaloric effect for NiTi shape memory alloy: Experimental observation and constitutive model. Int J Solids Struct. 2022 Jul 1;248.

62. Tušek J, Engelbrecht K, Mikkelsen LP, Pryds N, Tu J. Elastocaloric effect of Ni-Ti wire for application in a cooling device. J Appl Phys. 2015;124901(117).

63. Chen P, Cai X, Liu Y, Wang Z, Jin M, Jin X. Combined effects of grain size and training on fatigue resistance of nanocrystalline NiTi shape memory alloy wires. Int J Fatigue. 2023 Mar 1;168.

64. Liang D, Wang Q, Chu K, Chen J, Hua P, Ren F, et al. Ultrahigh cycle fatigue of nanocrystalline NiTi tubes for elastocaloric cooling. Appl Mater Today [Internet]. 2022;26:101377. Available from: https://doi.org/10.1016/j.apmt.2022.101377

65. Chen J, Lei L, Fang G, Wang D. Achieving great comprehensive elastocaloric cooling performances of superelastic NiTi by grain size engineering. Mater Today Nano. 2023 Mar 1;21.

66. Lin H, Hua P, Sun Q. Effects of grain size and partial amorphization on elastocaloric cooling performance of nanostructured NiTi. Scr Mater. 2022 Mar 1;209.

67. Deng Z, Huang K, Yin H, Sun Q. Temperature-dependent mechanical properties and elastocaloric effects of multiphase nanocrystalline NiTi alloys. J Alloys Compd. 2023 Mar 25;938.

68. Dang P, Pang J, Zhou Y, Ding L, Zhang L, Ding X, et al. Improved stability of superelasticity and elastocaloric effect in Ti-Ni alloys by suppressing Lüders-like deformation under tensile load. J Mater Sci Technol. 2023 May 20;146:154–67.

69. Chen J, Lei L, Fang G. Grain-size effects on the temperature-dependent elastocaloric cooling performance of polycrystalline NiTi alloy. J Alloys Compd. 2022 Dec 15;927.

70. Xu B, Xiong J, Yu C, Wang C, Wang Q, Kang G. Improved elastocaloric effect of NiTi shape memory alloys via microstructure engineering: A phase field simulation. Int J Mech Sci. 2022 May 15;222.

71. Xu B, Wang C, Wang Q, Yu C, Kan Q, Kang G. Enhancing elastocaloric effect of NiTi alloy by concentration-gradient engineering. Int J Mech Sci. 2023 May 15;246.

72. Cheng S, Xiao Y, Li X, Lin H, Hua P, Sheng L, et al. Elastocaloric effect characterization of a NiTi tube to be applied in a compressive cooler. AIP Adv. 2022 Dec 1;12(12).

73. Zhang J, Zhu Y, Yao S, Sun Q. Highly efficient grooved NiTi tube refrigerants for compressive elastocaloric cooling. Appl Therm Eng. 2023 Jun 25;228.

74. Zhu X, Zhang X, Qian M, Zhong S, Muhammad I, Geng L. Enhanced elastocaloric stability in NiTi alloys under shear stress. Materials Science and Engineering: A. 2022 Mar 24;838.

75. Wieczorek A, Frenzel J, Schmidt M, Seelecke S, Eggeler G, Maaß B, et al. Optimizing Ni – Ti-based shape memory alloys for ferroic cooling. Functional Materials Letters. 2017;10(1):1–8.

76. Frenzel J, Wieczorek A, Opahle I, Maaß B, Drautz R, Eggeler G. On the effect of alloy composition on martensite start temperatures and latent heats in Ni – Ti-based shape memory alloys. Acta Mater [Internet]. 2015;90:213–31. Available from: http://dx.doi.org/10.1016/j.actamat.2015.02.029

77. Chen X, Srivastava V, Dabade V, James RD. Study of the cofactor conditions: Conditions of supercompatibility between phases. J Mech Phys Solids [Internet]. 2013;61(12):2566–87. Available from: http://dx.doi.org/10.1016/j.jmps.2013.08.004

78. Zhang Z, James RD, Muller S. Energy barriers and hysteresis in martensitic phase transformations. Acta Mater. 2009;57(147):4332–52.

79. Bruederlin F, Bumke L, Chluba C, Ossmer H, Quandt E, Kohl M. Elastocaloric Cooling on the Miniature Scale: A Review on Materials and Device Engineering. Energy Technology. 2018;1588–604.

80. Xiao F, Fukuda T, Kakeshita T, Jin X. Elastocaloric effect by a weak first-order transformation associated with lattice softening in an Fe-31.2Pd (at.%) alloy. Acta Mater [Internet]. 2015;87:8–14. Available from: http://dx.doi.org/10.1016/j.actamat.2015.01.004

81. Xiao F, Fukuda T, Kakeshita T. Significant elastocaloric effect in a Fe-31.2Pd (at. %) single crystal. Appl Phys Lett. 2013;161914(May):1–5.

82. Xiao F, Bucsek A, Jin X, Porta M, Planes A. Giant elastic response and ultra-stable elastocaloric effect in tweed textured Fe-Pd single crystals. Acta Mater. 2022 Jan 15;223.

83. Shen Q, Zhao D, Sun W, Wei Z, liu J. Microstructure, martensitic transformation and elastocaloric effect in Pd-In-Fe polycrystalline shape memory alloys. Intermetallics

(Barking) [Internet]. 2018;100(May):27–31. Available from: https://doi.org/10.1016/j.intermet.2018.05.018

84. Soto-Parra DE, Vives E, González-Alonso D, Manosa L, Planes A, Romero R, et al. Stress- and magnetic field-induced entropy changes in Fe-doped Ni-Mn-Ga shape-memory alloys. Appl Phys Lett. 2010;96(7).

85. Castillo-Villa PO, Soto-Parra DE, Matutes-Aquino JA, Ochoa-Gamboa RA, Planes A, Mañosa L, et al. Caloric effects induced by magnetic and mechanical fields in a Ni 50Mn25-xGa25Cox magnetic shape memory alloy. Phys Rev B Condens Matter Mater Phys. 2011;83(17):1–6.

86. Xiao F, Jin M, Liu J, Jin X. Elastocaloric effect in Ni50Fe19Ga27Co4 single crystals. Acta Mater [Internet]. 2015;96:292–300. Available from: http://dx.doi.org/10.1016/j.actamat.2015.05.054

87. Li D, Li Z, Zhang X, Yang B, Wang D, Zhao X, et al. Enhanced cyclability of elastocaloric effect in a directionally solidified Ni55Mn18Ga26Ti1 alloy with low hysteresis. Scr Mater [Internet]. 2020;189:78–83. Available from: https://doi.org/10.1016/j.scriptamat.2020.08.010

88. Lu B, Zhang P, Xu Y, Sun W, Liu J. Elastocaloric effect in Ni45Mn36.4In13.6Co5 metamagnetic shape memory alloys under mechanical cycling. Mater Lett [Internet]. 2015;148:110–3. Available from: http://dx.doi.org/10.1016/j.matlet.2015.02.076

89. Yang Z, Cong DY, Sun XM, Nie ZH, Wang YD. Enhanced cyclability of elastocaloric effect in boron-microalloyed Ni-Mn-In magnetic shape memory alloys. Acta Mater [Internet]. 2017;127:33–42. Available from: http://dx.doi.org/10.1016/j.actamat.2017.01.025

90. Shen Q, Zhao D, Sun W, Li Y, Liu J. The effect of Tb on elastocaloric and mechanical properties of Ni-Mn-In-Tb alloys. J Alloys Compd [Internet]. 2017;696:538–42. Available from: http://dx.doi.org/10.1016/j.jallcom.2016.11.290

91. Shen A, Sun W, Zhao D, Liu J. Influence of Cr on microstructure and elastocaloric effect in Ni–Mn–In–Co–Cr polycrystalline alloys. Physics Letters, Section A: General, Atomic

and Solid State Physics [Internet]. 2018;382(39):2876–9. Available from: https://doi.org/10.1016/j.physleta.2018.06.022

92. Xu Y, Lu B, Sun W, Yan A, Liu J. Large and reversible elastocaloric effect in dual-phase Ni54Fe19Ga27 superelastic alloys. Appl Phys Lett [Internet]. 2015;106(20). Available from: http://dx.doi.org/10.1063/1.4921531

93. Li Y, Zhao D, Liu J. Giant and reversible room- temperature elastocaloric effect in a single-crystalline Ni-Fe-Ga magnetic shape memory alloy. Sci Rep. 2016;(January):1–11.

94. Álvarez-Alonso P, Aguilar-Ortiz CO, Villa E, Nespoli A, Flores-Zúñiga H, Chernenko VA. Conventional and inverse elastocaloric effect in Ni-Fe-Ga and Ni-Mn-Sn ribbons. Scr Mater [Internet]. 2017;128:36–40. Available from: http://dx.doi.org/10.1016/j.scriptamat.2016.09.033

95. Eftifeeva A, Panchenko E, Yanushonite E, Kurlevskaya I, Timofeeva E, Tokhmetova A, et al. Superelasticity and elastocaloric cooling capacity in stress-induced martensite aged [001]A-oriented Ni54Fe19Ga27 single crystals. Materials Science and Engineering: A. 2022 Oct 10;855.

96. Panchenko EY, Yanushonite EI, Eftifeeva AS, Tokhmetova AB, Kurlevskaya ID, Tagiltsev AI, et al. Elastocaloric Effect in Aged Single Crystals of Ni54Fe19Ga27 Ferromagnetic Shape Memory Alloy. Metals (Basel). 2022 Aug 1;12(8).

97. Masdeu F, Pons J, Torrens-Serra J, Chumlyakov Y, Cesari E. Superelastic behavior and elastocaloric effect in a Ni51.5Fe21.5Ga27.0 ferromagnetic shape memory single crystal under compression. Materials Science and Engineering: A. 2022 Jan 26;833.

98. Yang Z, Cong DY, Huang L, Nie ZH, Sun XM, Zhang QH, et al. Large elastocaloric effect in a Ni-Co-Mn-Sn magnetic shape memory alloy. Mater Des [Internet]. 2016;92:932–6. Available from: http://dx.doi.org/10.1016/j.matdes.2015.12.118

99. Sun W, Liu J, Lu B, Li Y, Yan A. Large elastocaloric effect at small transformation strain in Ni45Mn44Sn11 metamagnetic shape memory alloys. Scr Mater [Internet]. 2016;114:1–4. Available from: http://dx.doi.org/10.1016/j.scriptamat.2015.11.021

100. Li Y, Sun W, Zhao D, Xu H, Liu J. An 8 K elastocaloric temperature change induced by 1.3% transformation strain in Ni44Mn45 xSn11Cux alloys. Scr Mater [Internet]. 2017;130:278–82. Available from: http://dx.doi.org/10.1016/j.scriptamat.2016.12.014

101. Zhu Y, Xuan H, Su J, Chen F, Zhang K, Han P, et al. Large elastocaloric effect in as-cast Ni-Mn-Sn-Fe ferromagnetic shape memory alloys. Physics Letters, Section A: General, Atomic and Solid State Physics. 2022 Nov 5;451.

102. Khan M, Wang Y, Wang C, Liao X, Yang S, Song X, et al. Combination of conventional elastocaloric and magnetocaloric effects in a Co37Ni35Al28 ferromagnetic shape memory alloy. Scr Mater [Internet]. 2018;146:182–6. Available from: https://doi.org/10.1016/j.scriptamat.2017.11.041

103. Zhang X, Chen H, Li S, Niu Y, Yin T, Song C, et al. Enhanced cyclability of superelasticity and elastocaloric effect in Cu and B co-doped Co-Ni-Ga shape memory alloys. J Alloys Compd. 2022 Oct 15;918.

104. Lisenkov S, Ponomareva I. Giant elastocaloric effect in ferroelectric Ba 0.5Sr 0.5TiO 3 alloys from first-principle. Phys Rev B Condens Matter Mater Phys. 2012;86(10):6–9.

105. Lisenkov S, Mani BK, Chang CM, Almand J, Ponomareva I. Multicaloric effect in ferroelectric PbTiO3 from first principles. Phys Rev B Condens Matter Mater Phys. 2013;87(22):1–4.

106. Wei ZG, Sandstroröm R, Miyazaki S. Shape-memory meterials and hybrid composites for smart systems. J Mater Sci. 1998;33(15):3743–62.

107. Singh N, Talapatra A, Junkaew A, Duong T, Gibbons S, Li S, et al. Effect of ternary additions to structural properties of NiTi alloys. Comput Mater Sci [Internet]. 2016;112:347–55. Available from: http://dx.doi.org/10.1016/j.commatsci.2015.10.029

108. Morakabati M, Kheirandish S, Aboutalebi M, Taheri AK, Abbasi SM. The effect of Cu addition on the hot deformation behavior of NiTi shape memory alloys. J Alloys Compd [Internet]. 2010;499(1):57–62. Available from: http://dx.doi.org/10.1016/j.jallcom.2010.01.124

109. Fu B, Feng K, Li Z. Study on the effect of Cu addition on the microstructure and properties of NiTi alloy fabricated by laser cladding. Mater Lett. 2018;220:148–51.

110. Yang C, Cheng QR, Liu LH, Li YH, Li YY. Effect of minor Cu content on microstructure and mechanical property of NiTiCu bulk alloys fabricated by crystallization of metallic glass powder. Intermetallics (Barking). 2015;56:37–43.

111. Furuya Y, Matsumoto M, Kimura HS, Masumoto T. Thermoelastic phase transformation of melt-spun Ti50Ni50-xCux (x=0-20at.%) ribbons. Materials Science and Engineering A [Internet]. 1991;147(1):7–11. Available from: http://www.scopus.com/inward/record.url?eid=2-s2.0-0026241089&partnerID=tZOtx3y1

112. Nam TH, Saburi T, Shimizu K. Cu-Content Dependence of Shape Memory Characteristics in Ti-Ni-Cu Alloys. Materials Transactions, JIM. 1990;31(11).

113. Nespoli A, Villa E, Besseghini S. Characterization of the martensitic transformation in Ni 50-xTi50Cux alloys through pure thermal measurements. J Alloys Compd [Internet]. 2011;509(3):644–7. Available from: http://dx.doi.org/10.1016/j.jallcom.2010.09.145

114. Ohba T, Taniwaki T, Miyamoto H, Otsuka K, Kato K. In situ observations of martensitic transformations in Ti50Ni34Cu16 alloy by synchrotron radiation. Materials Science and Engineering A. 2006;438–440(SPEC. ISS.):480–4.

115. Miyamoto H, Taniwaki T, Ohba T, Otsuka K, Nishigori S, Kato K. Two-stage B2-B19-B19′ martensitic transformation in a Ti 50Ni30Cu20 alloy observed by synchrotron radiation. Scr Mater. 2005;53(2):171–5.

116. Jones NG, Dye D. Influence of applied stress on the transformation behaviour and martensite evolution of a Ti-Ni-Cu shape memory alloy. Intermetallics (Barking) [Internet]. 2013;32:239–49. Available from: http://dx.doi.org/10.1016/j.intermet.2012.07.020

117. Ghadimi M, Vanda M, Ali Sourani M. Nanocrystalline Ti-Ni-Cu shape memory alloys: Metallurgical, mechanical and thermal properties. Mater Lett [Internet]. 2015;139:359–63. Available from: http://dx.doi.org/10.1016/j.matlet.2014.10.116

118. Zhang H, He Y, Yang F, Liu H, Jin Z. Thermodynamic assessment of Cu-Ni-Ti ternary system assisted with key measurements. Thermochim Acta [Internet]. 2013;574:121–32. Available from: http://dx.doi.org/10.1016/j.tca.2013.08.012

119. Zhu WJ, Duarte LI, Leinenbach C. Experimental study and thermodynamic assessment of the Cu-Ni-Ti system. CALPHAD [Internet]. 2014;47:9–22. Available from: http://dx.doi.org/10.1016/j.calphad.2014.06.002

120. Uchil J, Mahesh KK, Ganesh Kumara K. Dilatometric study of martensitic transformation in NiTiCu and NiTi shape memory alloys. J Mater Sci. 2001;36(24):5823–7.

121. Dang P, Zhou Y, Pang J, Ding X, Sun J, Lookman T, et al. Achieving stable actuation response and elastocaloric effect in a nanocrystalline Ti50Ni40Cu10 alloy. Scr Mater. 2023 Mar 15;226.

122. Dang P, Zhou Y, Ding X, Sun J, Lookman T, Xue D. Tailoring Grain Size and Precipitation via Aging for Improved Elastocaloric Stability in a Cold-Rolled (Ni,Cu)-Rich Ti–Ni–Cu Alloy. Shape Memory and Superelasticity. 2023 Jun 1;9(2):334–44.

123. Dang P, Ye F, Zhou Y, Ding L, Pang J, Zhang L, et al. Low-fatigue and large room-temperature elastocaloric effect in a bulk Ti49.2Ni40.8Cu10 alloy. Acta Mater. 2022 May 1;229.

124. Chluba C, Ge W, Miranda RL De, Strobel J, Kienle L, Quandt E, et al. Ultralow-fatigue shape memory alloy films. Science (1979). 2015;348(6238):1004–8.

125. Chluba C, Ossmer H, Zamponi C, Kohl M, Quandt E. Ultra-Low Fatigue Quaternary TiNi-Based Films for Elastocaloric Cooling. Shape Memory and Superelasticity. 2016;2(1):95–103.

126. Ahadi A, Ghorabaei AS, Shirazi H, Nili-Ahmadabadi M. Bulk NiTiCuCo shape memory alloys with ultra-high thermal and superelastic cyclic stability. Scr Mater. 2021 Jul 15;200.

127. Zhang H, Liu J, Ma Z, Ren Y, Jiang D, Cui L, et al. Small stress-hysteresis in a nanocrystalline TiNiCuFe alloy for elastocaloric applications over wide temperature window. J Alloys Compd. 2022 Dec 20;928.

128. Xue D, Li Z, Pan Y, Zhang G. Low hysteresis and high cyclic stability in a Ti50Ni45.2Cu1Fe3.8 shape memory alloy. J Alloys Compd. 2023 Sep 10;955.

129. Meng XL, Li H, Cai W, Hao SJ, Cui LS. Thermal cycling stability mechanism of Ti50.5Ni33.5Cu11.5Pd4.5 shape memory alloy with near-zero hysteresis. Scr Mater. 2015;103:30–3.

130. Li H, Meng X, Cai W. Shape memory behaviors in a Ti50Ni33.5Cu12.5Pd4 alloy with near-zero thermal hysteresis. J Alloys Compd [Internet]. 2018;765:166–70. Available from: https://doi.org/10.1016/j.jallcom.2018.06.205

131. Tong Y, Gu H, James RD, Qi W, Shuitcev A V, Li L. Novel TiNiCuNb shape memory alloys with excellent thermal cycling stability. J Alloys Compd. 2019;782:343–7.

132. Zhou X, Huang Z, Chen F, Tian B, Li L, Tong Y. Two-way shape memory effect with excellent cycling stability in TiNiCuNb alloy. Mater Lett. 2022;308(November 2021):2021–3.

133. Louzguine D V, Kato H, Inoue A. High strength and ductile bulk Ti-Ni-Cu-Nb alloy with submicron-size structure units obtained by arc-melting. J Alloys Compd. 2004;375(2004):171–4.

134. Kim HY, Jinguu T, Nam T hyun, Miyazaki S. Cold workability and shape memory properties of novel Ti-Ni-Hf-Nb high-temperature shape memory alloys. Scr Mater [Internet]. 2011;65(9):846–9. Available from: http://dx.doi.org/10.1016/j.scriptamat.2011.07.049

135. Jiang D, Liu Y, Liu W, Song L, Jiang X, Yanh H, et al. Microstructure, transformation behavior and mechanical properties of a (Ti50Ni38Cu12)93Nb7 alloy. Materials Science & Engineering A [Internet]. 2015;627:348–50. Available from: http://dx.doi.org/10.1016/j.msea.2015.01.028

136. Wang GC, Hu KP, Tong YX, Tian B, Chen F, Li L, et al. Influence of Nb content on martensitic transformation and mechanical properties of TiNiCuNb shape memory alloys. Intermetallics (Barking). 2016;72:30–5.

137. Liu MY, Qi WY, Tong YX, Tian B, Chen F, Li L. Study of martensitic transformation in TiNiCuNb shape memory alloys using dynamic mechanical analysis. Vacuum. 2018;155(April):358–60.

138. Zhu WJ, Duarte LI, Leinenbach C. Experimental study and thermodynamic assessment of the Cu-Ni-Ti system. CALPHAD. 2014;47:9–22.

139. Matsumoto S, Tokunaga T, Ohtani H, Hasebe M. Thermodynamic analysis of the phase equilibria of the Nb-Ni-Ti system. Mater Trans. 2005;46(12):2920–30.

140. Gupta KP. The Nb-Ni-Ti (Niobium-Nickel-Titanium) System—Update. J Phase Equilibria Diffus. 2008;29(2):194–7.

141. Santhy K, Hari Kumar KC. Thermodynamic reassessment of Nb-Ni-Ti system with order-disorder model. J Alloys Compd [Internet]. 2015;619:733–47. Available from: http://dx.doi.org/10.1016/j.jallcom.2014.08.200

142. Yang G, Hao S. Study on the phase equilibria of the Ti–Ni–Nb ternary system at 900. J Alloys Compd. 2000;297:226–30.

143. Shim J hyeon, Kim J hyun, Lim J hwan, Kim JG, Oh JS, Lee T, et al. Improvement in the superelasticity of a Ti–35.5Ni–15Cu (at.%) alloy using Ti(Ni,Cu)2 phase. Materials Science and Engineering A. 2022;847(May).

144. Roy A, S. N. Impact of variation in wire electro discharge machining responses of homologous TiNiCu shape memory alloys for smart applications : An experimental investigation. Mater Res Express. 2018;29(27).

145. Villa F, Nespoli A, Passaretti F, Villa E. Microstructural and thermo-mechanical characterization of cast niticu20 shape memory alloy. Materials. 2021;14(14).

146. Zheng HX, Mentz J, Bram M, Buchkremer HP, Stöver D. Powder metallurgical production of TiNiNb and TiNiCu shape memory alloys by combination of pre-alloyed and elemental powders. J Alloys Compd. 2008;463(1–2):250–6.

147. Pan G, Balagna C, Martino L, Pan J, Spriano S. Microstructure and transformation temperatures in rapid solidified Ni – Ti alloys. Part II : The effect of copper addition. J Alloys Compd [Internet]. 2014;589:633–42. Available from: http://dx.doi.org/10.1016/j.jallcom.2013.09.212

148. Nam TH, Saburi T, Nakata Y, Shimizu K. Shape Memory Characteristics and Lattice Deformation in Ti-Ni-Cu Alloys. Materials Transactions, JIM. 1990;31(12):1050–6.

149. Li J, Wang H, Liu J, Ruan J. Effects of Nb addition on microstructure and mechanical properties of TiNiNb alloys fabricated by elemental powder sintering. Materials Science & Engineering A [Internet]. 2014;609:235–40. Available from: http://dx.doi.org/10.1016/j.msea.2014.05.007

150. Lukas HL, Fries SG, Sundman B. Computational Thermodynamics : The Calphad Method. 2006;

151. Andersson JO, Helander T, Hdghmd L, Shi P, Sundman B. THERMO-CALC & DICTRA, Computational Tools For Materials Science. Calphad. 2002;26(2):273–312.

152. Fahrmann MG, Smith GD. Capitalizing on computational tools in industrial alloy development. Applied Technology - Modeling High Temperature Materials. 2002;

153. Valberg HS. Applied Metal Forming - Including FEM Analysis. Cambrige University Press; 2010. 477 p.

154. Zienkiewicz OC, Taylor RL, Zhu JZ. The Finite Elemento Method - Its basis and fundamentals. 7th ed. Vol. 7, Elseiver. Oxford: Butterworth-Heinemann; 2015. 37–72 p.

155. Rao SS. The Finite Element Method in Engineering. 6th ed. Oxford: Butterworth-Heinemann; 2011. 754 p.

156. Murray JL. The Cu-Ti (Copper-Titanium) System. Bulletin of Alloy Phase Diagrams. 1983;4(1):81–95.

157. Hamalainen M, Jaaskelainen K, Luoma R, Nuotio M, Taskinen P, Teppo O. A Thermodynamic Analysis of the Binary Alloy Systems Cu-Cr, Cu-Nb, Cu-V. CALPHAD. 1990;14(2):125–37.

158. Gupta KP. The Cu-Ni-Ti (Copper-Nickel-Titanium) System. Journal of Phase Equilibria(Cu,. 2002;23(6):541–7.

159. Kejun Z, Xianzhang Z, Zhanpeng J. A thermodynamic calculation of the Ni-Nb phase diagram. J Alloys Compd. 1992;179(1–2):177–85.

160. Bolcavage A, Kattner UR. A reassessment of the calculated Ni-Nb phase diagram. Journal of Phase Equilibria. 1996;17(2):92–100.

161. Murray JL. The Nb-Ti (Niobium-Titanium) System. Bulletin of Alloy Phase Diagrams. 1981;2(1):55–61.

162. Fan QC, Zhang Y, Zhang YH, Wang YY, Yan EH, Huang SK, et al. Influence of Ni/Ti ratio and Nb addition on martensite transformation behavior of NiTiNb alloys. J Alloys Compd [Internet]. 2019;790:1167–76. Available from: https://doi.org/10.1016/j.jallcom.2019.02.330

163. Fan QC, Sun MY, Zhang YH, Wang YY, Zhang Y, Peng HB, et al. Influence of precipitation on phase transformation and mechanical properties of Ni-rich NiTiNb alloys. Mater Charact [Internet]. 2019;154(March):148–60. Available from: https://doi.org/10.1016/j.matchar.2019.05.013

164. Lukas HL, Fries SG, Sundman B. Computational thermodynamics: The Calphad method. Vol. 9780521868, Computational Thermodynamics: The Calphad Method. 2007. 1–313 p.

165. Chen Q, Sundman B. Computation of partial equilibrium solidification with complete interstitial and negligible substitutional solute back diffusion. Mater Trans. 2002;43(3):551–9.

166. Schaffnit P, Stallybrass C, Konrad J, Stein F, Weinberg M. A Scheil-Gulliver model dedicated to the solidification of steel. CALPHAD [Internet]. 2015;48:184–8. Available from: http://dx.doi.org/10.1016/j.calphad.2015.01.002

167. Samal S, Biswas K, Phanikumar G. Solidification Behavior in Newly Designed Ni-Rich Ni-Ti-Based Alloys. Metall Mater Trans A Phys Metall Mater Sci. 2016;47(12):6214–23.

168. Zhang Y, Hu B, Zeng G, Liu S, Du Y, Yin H. Experimental investigation, thermodynamic modeling and solidified microstructure of the Cu–Ti–Nb ternary system. CALPHAD [Internet]. 2022;76(October 2021):102395. Available from: https://doi.org/10.1016/j.calphad.2022.102395

169. Chen SL, Yang Y, Chen SW, Lu XG, Chang YA. Solidification simulation using scheil model in multicomponent systems. J Phase Equilibria Diffus. 2009;30(5):429–34.

170. Chang K, Liu S, Zhao D, Du Y, Zhou L, Chen L. Thermodynamic description of the Al-Cu-Mg-Mn-Si quinary system and its application to solidification simulation. Thermochim Acta [Internet]. 2011;512(1–2):258–67. Available from: http://dx.doi.org/10.1016/j.tca.2010.11.009

171. Morakabati M, Aboutalebi M, Kheirandish S, Taheri AK, Abbasi SM. Hot tensile properties and microstructural evolution of as cast NiTi and NiTiCu shape memory alloys. Mater Des [Internet]. 2011;32(1):406–13. Available from: http://dx.doi.org/10.1016/j.matdes.2010.05.048

172. Etaati A, Dehghani K. A study on hot deformation behavior of Ni-42.5Ti-7.5Cu alloy. Mater Chem Phys [Internet]. 2013;140(1):208–15. Available from: http://dx.doi.org/10.1016/j.matchemphys.2013.03.022

173. Nayan N, Singh G, Murty SVSN, Narayan PR, Mohan M, Venkitakrishnan P V., et al. Effect of ternary additions of Cu and Fe on the hot deformation behavior of NiTi shape memory alloy - A study using processing maps. Intermetallics (Barking) [Internet]. 2021;131(February):107084. Available from: https://doi.org/10.1016/j.intermet.2021.107084

174. Chen J, Zhang S, Zhang Y, Zhang J, Wen Y, Yang Q, et al. A study on the cold workability and shape memory effect of NiTiHf-Nb eutectic high-temperature shape memory alloy. Intermetallics (Barking) [Internet]. 2020;127(June):106982. Available from: https://doi.org/10.1016/j.intermet.2020.106982

175. Shi H, Pourbabak S, Humbeeck J Van, Schryvers D. Electron microscopy study of Nb-rich nanoprecipitates in Ni – Ti – Nb and their influence on the martensitic transformation. Scr Mater [Internet]. 2012;67:939–42. Available from: http://dx.doi.org/10.1016/j.scriptamat.2012.08.020

176. ASTM. Standard test method for tension testing of nickel-titanium superelastic materials. ASTM - F2516. 2015. p. 1–6.

177. Chen J, Xing L, Fang G, Lei L, Liu W. Improved elastocaloric cooling performance in gradient-structured NiTi alloy processed by localized laser surface annealing. Acta Mater [Internet]. 2021;208:116741. Available from: https://doi.org/10.1016/j.actamat.2021.116741

178. Ribeiro RM, Lemus LF, Dos Santos DS. Hydrogen absorption study of Ti-based alloys performed by melt-spinning. Materials Research. 2013;16(3):679–82.

179. Ghadimi M, Vanda M, Ali Sourani M. Nanocrystalline Ti-Ni-Cu shape memory alloys: Metallurgical, mechanical and thermal properties. Mater Lett. 2015;139:359–63.

180. Jiang H, Cao S, Ke C, Ma X, Zhang X. Fine-grained bulk NiTi shape memory alloy fabricated by rapid solidification process and its mechanical properties and damping performance. J Mater Sci Technol [Internet]. 2013;29(9):855–62. Available from: http://dx.doi.org/10.1016/j.jmst.2013.05.007

181. Tyc O, Molnárová O, Šittner P. Effect of microstructure on fatigue of superelastic NiTi wires. Int J Fatigue. 2021;152(July).

182. Silva JD, Macieira GF, Santos DS, Santos L de A, Buono VTLB. Role of Nb on the phase stability and morphology of Ti-Ni-Cu-Nb alloys. Journal of Materials Research and Technology [Internet]. 2022;20:1428–36. Available from: https://doi.org/10.1016/j.jmrt.2022.07.146

183. Silva JD, Santos DS, Santos LA, Buono VTL. Effect of Nb Addition on the Thermodynamic of Solidification in a Ti-Ni-Cu Alloy. Materials Research. 2023;26:1–7.

184. Hou H, Simsek E, Stasak D, Hasan N Al, Qian S, Ott R, et al. Elastocaloric cooling of additive manufactured shape memory alloys with large latent heat. J Phys D Appl Phys. 2017;50(40).

185. Gu X, Zhang Y, You Y, Ju X, Zhu J, Moumni Z, et al. Evolution of transformation characteristics of shape memory alloys during cyclic loading: Transformation temperature hysteresis and residual martensite. Smart Mater Struct. 2020;29(9).

186. Kato H, Yasuda Y, Sasaki K. Thermodynamic assessment of the stabilization effect in deformed shape memory alloy martensite. Acta Mater [Internet]. 2011;59(10):3955–64. Available from: http://dx.doi.org/10.1016/j.actamat.2011.03.021

187. Polatidis E, Šmíd M, Kuběna I, Hsu WN, Laplanche G, Van Swygenhoven H. Deformation mechanisms in a superelastic NiTi alloy: An in-situ high resolution digital image correlation study. Mater Des. 2020;191:1–10.

188. Polatidis E, Zotov N, Bischoff E, Mittemeijer EJ. The effect of cyclic tensile loading on the stress-induced transformation mechanism in superelastic NiTi alloys: An in-situ X-ray diffraction study. Scr Mater [Internet]. 2015;100:59–62. Available from: http://dx.doi.org/10.1016/j.scriptamat.2014.12.013

189. Mendes Rodrigues MC, Corrêa Soares G, Lopes Buono VT, de Arruda Santos L. Effects of Pseudoelastic Cycling under Different Temperatures on Physical and Mechanical Properties of a NiTi Alloy. Advances in Science and Technology. 2016;97:134–40.

190. Soto-Parra D, Vives E, Mañosa L, Matutes-Aquino JA, Flores-Zúñiga H, Planes A. Elastocaloric effect in Ti-Ni shape-memory wires associated with the B2 ↔ B19’ and B2 ↔ R structural transitions. Appl Phys Lett [Internet]. 2016;071902(February):2–7. Available from: http://dx.doi.org/10.1063/1.4942009

191. Sharar DJ, Donovan BF, Warzoha RJ, Wilson AA, Leff AC, Hanrahan BM. Solid-state thermal energy storage using reversible martensitic transformations. Appl Phys Lett. 2019;114(14).

192. Chang PC, Ko ML, Ramachandran B, Kuo YK, Chien C, Wu SK. Comparative study of R-phase martensitic transformations in TiNi- based shape memory alloys induced by point defects and precipitates. Intermetallics (Barking). 2017;84:130–5.

193. Ossmer H, Chluba C, Quandt E, Kohl M. TiNi-based films for elastocaloric microcooling — Fatigue life and device performance. APL Mater [Internet]. 2016;064102(April). Available from: http://dx.doi.org/10.1063/1.4948271

194. Chen H, Xiao F, Liang X, Li Z, Li Z, Jin X, et al. Improvement of the stability of superelasticity and elastocaloric effect of a Ni-rich Ti-Ni alloy by precipitation and grain refinement. Scr Mater [Internet]. 2019;162:230–4. Available from: https://doi.org/10.1016/j.scriptamat.2018.11.024

195. Tusek J, Zerovnik A, Brojan M, Zuzek B, Engelbrecht K, Cadelli A. Elastocaloric effect vs fatigue life: Exploring the durability limits of Ni-Ti plates under pre-strain conditions for elastocaloric cooling. Acta Mater. 2018;150:295–307.

196. Aaltio I, Fukuda T, Kakeshita T. Elastocaloric cooling and heating using R-phase transformation in hot rolled Ni-Ti-Fe shape memory alloys with 2 and 4 at % Fe content. J Alloys Compd [Internet]. 2019;780:930–6. Available from: https://doi.org/10.1016/j.jallcom.2018.11.406

197. Kim Y, Jo MG, Park JW, Park HK, Han HN. Elastocaloric effect in polycrystalline Ni50Ti45.3V4.7 shape memory alloy. Scr Mater. 2018;144:48–51.

198. Mercier O, Melton KN, Effect S. Kinetics and thermodynamics of the shapememory effect in martensitic NiTi and (Ni1−x Cu x)Ti alloys. J Appl Phys. 1979;5747(1979).

199. Chang SH, Hsiao SH. Inherent internal friction of Ti50Ni50-xCux shape memory alloys measured under isothermal conditions. J Alloys Compd [Internet]. 2014;586:69–73. Available from: http://dx.doi.org/10.1016/j.jallcom.2013.10.026

200. Valeanu M, Lucaci M, Crisan AD, Sofronie M, Leonat L, Kuncser V. Martensitic transformation of Ti50Ni30Cu20 alloy prepared by powder metallurgy. J Alloys Compd [Internet]. 2011;509(13):4495–8. Available from: http://dx.doi.org/10.1016/j.jallcom.2011.01.154

201. Wei ZG, Miyazaki S, Tang W, Sandstro R. Experimental Investigation and Thermodynamic Calculation of the Ti-Ni-Cu Shape Memory Alloys. Metallurgical and Materials Transactions A. 2000;31(October):2423–30.

202. Ullrich FWJ, Schmidt HOM, Chluba MKC, Schütze EQA. Numerical simulation and experimental investigation of the elastocaloric cooling effect in sputter-deposited TiNiCuCo. Continuum Mechanics and Thermodynamics. 2017;

203. Schmidt M, Ullrich J, Wieczorek A, Frenzel J, Schutze A, Eggeler G, et al. Thermal Stabilization of NiTiCuV Shape Memory Alloys: Observations During Elastocaloric Training platform that allows observation of temperature profiles. Shape Memory and Superelasticity. 2015;1:132–41.

204. Nespoli A, Besseghini S. A complete thermo-mechanical study of a NiTiCu shape memory alloy wire. J Therm Anal Calorim. 2011;103(3):821–6.

205. Aghamiri SMS, Ahmadabadi MN, Raygan S. Combined effects of different heat treatments and Cu element on transformation behavior of NiTi orthodontic wires. J Mech Behav Biomed Mater [Internet]. 2011;4(3):298–302. Available from: http://dx.doi.org/10.1016/j.jmbbm.2010.10.008

APPENDIX I – Energy saving potential of elastocaloric-based HVAC technology.

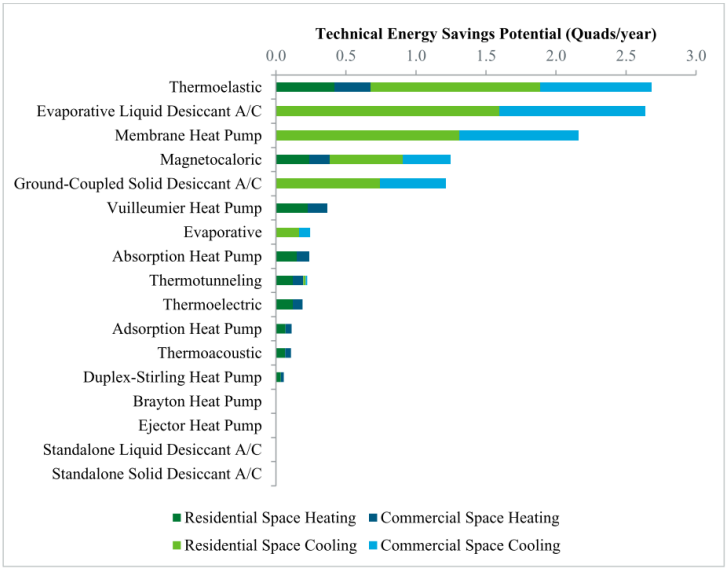

Figure ES-1-1: Comparison of technical energy savings potential (Quads/year)

Figure I-1 – Comparison of technical energy savings potential (19)

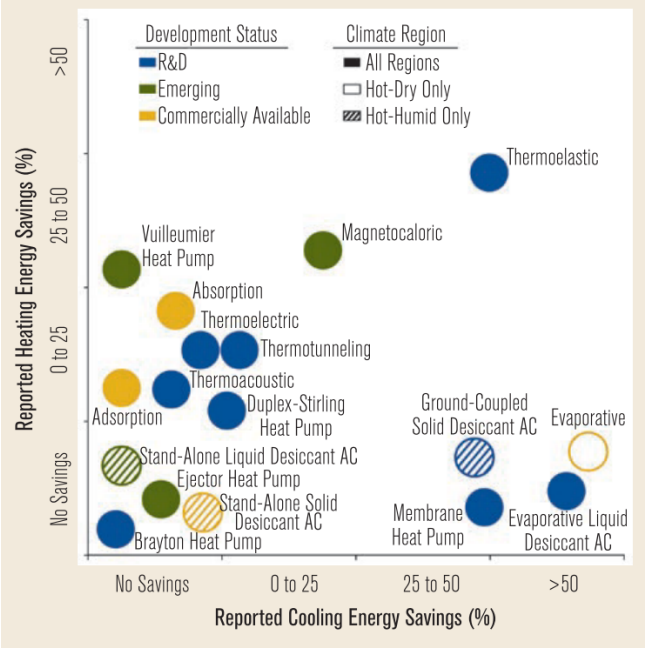

Figure I-2 – Reported energy savings of different alternatives to vapor compression(14)

APPENDIX II – Thermodynamic properties and COP measurements of TiNi and TiNiCu-based alloys

Table II.1 - Thermodynamic properties obtained from literature for other TiNi- based alloys

Alloy Composition	ΔHt (J/g)	ΔSt (J/Kg.K)	Cp (J/Kg.K)	Af (°C)	ΔTad (K)	COP	Ref
NiTi	12		550		17	3	(47)
$Ni_{45}Ti_{55}$	20.9		550	105.4	7.5	14.7	(184)
$Ni_{47.4}Ti_{52.6}^{B2-B19'}$		79.4		57			(190)
$Ni_{47.4}Ti_{52.6}^{B19'-R-B2}$		34.7		48			(190)
$Ni_{47.8}Ti_{52.2}^{B2}$	13.5			51	5-10		(191)
$Ni_{47.8}Ti_{52.2}^{R-phase}$	4.5			40	5-10		(191)
$Ti_{48.7}Ni_{51.3}^{R-phase}$	7.1	50					(192)
$Ni_{48.9}Ti_{51.1}$			450	22	20		(62)
$Ni_{50.1}Ti_{49.9}$		45			28		(25)
$Ni_{50.2}Ti_{49.8}$		74			40		(25)
$Ni_{50.37}Ti_{49.63}$	12.51	51	590	0	14		(55)
$Ni_{50.4}Ti_{49.6}$	7.2		450	20	16	7.7	(54)
$Ni_{50.4}Ti_{49.6}$	18.9		400	20	15		(57)
$Ni_{50.4}Ti_{49.6}$	18.9			20	15	2.9	(193)
$Ni_{50.7}Ti_{49.3}$	5.24		291	20.7	11	12.6	(24)
$Ni_{50.7}Ti_{49.3}$		8.5			11		(25)
$Ni_{50.8}Ti_{49.2}$	12.7	51.7	590	0	18.2		(43)
$Ni_{50.8}Ti_{49.2}$		37	424	0	11	4.5	(56)
$Ni_{50.8}Ti_{49.2}^{HT1123}$	0.8		3R	-9	8.2		(194)
$Ni_{50.8}Ti_{49.2}^{HT773}$	0.7		3R	31	24.3		(194)
$Ni_{50.8}Ti_{49.2}^{HT673}$	0.5		3R	57	26.4		(194)
$Ni_{50.8}Ti_{49.2}^{HT673'}$	0.5		3R	47	24.0		(194)

$Ni_{50.9}Ti_{49.1}$				-3	16		(195)
$Ni_{51.1}Ti_{48.9}$	14.6			4.0		5.8	(75)
$Ni_{56}Ti_{44}$			430	-9		17.6	(35)
$Ni_{50.5}Ti_{49.1}Fe_{0.4}$	8			5	15	10	(33)
$Ni_{50}Ti_{49.75}Fe_{0.25}$	24.7			96.0			(75)
$Ni_{50}Ti_{49}Fe_{1}$	26.7			70.1			(75)
$Ni_{50}Ti_{48}Fe_{2}$	24.1			39.8			(75)
$Ni_{50}Ti_{47.5}Fe_{2.5}$	20.7			26.0			(75)
$Ni_{50}Ti_{47}Fe_{3}$	16.5			15.1			(75)
$Ni_{48}Ti_{50}Fe_{2}^{R\text{-}B2}$	6	20.8	480	21	12.4		(196)
$Ni_{46}Ti_{50}Fe_{4}^{R\text{-}B2}$	4.3	17.7	590	-47	8.7		(196)
$Ni_{46}Ti_{50}Fe_{4}^{R\text{-}phase}$	6.1	26.3					(192)
$Ni_{50}Ti_{49.5}Co_{0.5}$	28.6			103.5			(75)
$Ni_{50}Ti_{49}Co_{1}$	24.9			91.5			(75)
$Ni_{50}Ti_{46}Co_{4}$	25.8			50.5			(75)
$Ni_{50}Ti_{44.5}Co_{5.5}$	22.5			23.3			(75)
$Ni_{50}Ti_{44}Co_{6}$	20.2			18.1			(75)
$Ni_{50}Ti_{43}Co_{7}$	15.4			5.0			(75)
$Ni_{50}Ti_{42.5}Co_{7.5}$	14.1			-0.8			(75)
$Ni_{50}Ti_{44}V_{6}$	10.3			-1.5		14.7	(75)
$Ni_{50}Ti_{45.3}V_{4.7}$	9.0	32	510	14.7	19.4	22.5	(197)
$Ni_{50.5}Ti_{36.2}Hf_{13}$	15.9	60	570	31.5	6.95		(43)

Table II.2 – Thermodynamic properties obtained from literature for TiNiCu alloys

Alloy Composition	ΔHt (J/g)	ΔSt (J/Kg.K)	Cp (J/Kg.K)	Af (°C)	ΔTad (K)	COP	Ref
$Ni_{41.5}Ti_{49.5}Cu_{9.1}$	11.3	37.8	560	31	15.2		(43)
$Ni_{49}Ti_{46}Cu_{5}$	21.7		468				(198)
$Ni_{50}Ti_{45}Cu_{5}$	23		468				(198)
$Ti_{50}Ni_{45}Cu_{5}$	22.1			55			(199)
$Ti_{50}Ni_{40}Cu_{10}$	17			51			(199)
$Ti_{50}Ni_{30}Cu_{20}$	13.6			61.6			(199)
$Ti_{50}Ni_{30}Cu_{20}$	12.3			82			(200)
$Ni_{39}Ti_{46}Cu_{15}$	12.9		468				(198)
$Ni_{47}Ti_{50}Cu_{3}$	25.3			77			(201)
$Ni_{45}Ti_{50}Cu_{5}$	26.2			69			(201)
$Ni_{43}Ti_{50}Cu_{7}$	24			62			(201)
$Ni_{42}Ti_{50}Cu_{8}$	19.2			61			(201)
$Ni_{41}Ti_{50}Cu_{9}$	17.7			64			(201)
$Ni_{40}Ti_{50}Cu_{10}$	17.9			62			(201)
$Ni_{37}Ti_{50}Cu_{13}$	16.9			65			(201)
$(Ni_{33}Ti_{55}Cu_{12})_{99.3}Fe_{0.7}$	8.8			35			(125)
$(Ni_{33}Ti_{55}Cu_{12})_{98.7}Fe_{1.3}$	7.5			6			(125)
$(Ni_{33}Ti_{55}Cu_{12})_{98.4}Fe_{1.6}$	5.9			-6			(125)
$(Ni_{33}Ti_{55}Cu_{12})_{98.7}Co_{1.3}$	9.0			40			(125)
$(Ni_{33}Ti_{55}Cu_{12})_{97.6}Co_{2.4}$	7.9			8			(125)
$(Ni_{33}Ti_{55}Cu_{12})_{96.4}Co_{3.6}$	6.1			-13			(125)
$(Ni_{33}Ti_{55}Cu_{12})_{95.7}Co_{5.3}$	2.8			-50			(125)

$Ni_{30.7}Ti_{54.7}Cu_{12.3}Co_{2.3}$	4.3	420	8	10.2	10	(125)
$Ni_{30.7}Ti_{54.7}Cu_{12.3}Co_{2.3}$	13.7	420	14	12		(57)
$Ni_{29.6}Ti_{55}Cu_{12.6}Co_{2.8}$	13.7		14	12	2.9	(193)
$Ni_{29.3}Ti_{55.2}Cu_{12.7}Co_{2.8}$	5	420				(202)
$Ni_{45}Ti_{47.25}Cu_{5}V_{2.75}$	9.2		5.2		20	(75)
$Ni_{45}Ti_{47.25}Cu_{5}V_{2.75}$	12.3		-3	21	5.97	(203)
$Ni_{43.49}Ti_{51.20}Cu_{5.31}$	25					(204)
$Ni_{45}Ti_{50}Cu_{5}Cr_{0.3}$	15.8		34			(205)

APPENDIX III – Manufacturing information on Ti-Ni-Cu-Nb alloys

Table III.1- Summary on the manufacturing route and obtained phases obtained from the literature

Alloy	Casting	Forming	Heat-treatment	Phases	Ref
$(Ti_{54}Ni_{34}Nu_{12})_{100-x}Nb_x$ (x = 0, 6, 10 at.%)	Arc-melting, argon Re-melted > 10x	Hot-rolled into plates of 1mm thickness	Solution-treated at 850°C for 120min in vacuum, water quenched	Nb6 – B19, β-Nb Nb10 – B19, β-Nb, $Ti_2(Ni,Cu)$	(131)
$(Ti_{50}Ni_{38}Cu_{12})_{100-x}Nb_x$ (x=0, 5, 10, 15at.%)	Arc-melting, argon	Hot-rolled into plates of 1.2mm thickness	Solution-treated at 900°C for 20min, water quenched	B2/B19, β-Nb, $Ti_2(Ni,Cu)$	(137)
$(Ti_{50}Ni_{40}Cu_{10})_{100-x}Nb_x$ (x=0, 5, 10, 15at.%)	Arc-melting, argon Re-melted > 6x	Hot-rolled into plates of 1.2mm thickness	Solution-treated at 900°C for 20min	Nb5 – B2, β-Nb, $Ti_2(Ni,Cu)$ Nb10 - B2, β-Nb	(136)
$(Ti_{50}Ni_{38}Cu_{12})_{93}Nb_7$	Arc-melting (0.5Kg ingot)	Hot-forged at 800ºC, hot-drawn at 500ºC into 2mm	Intermediate annealing at 630°C; annealing at different temperatures	B2, β-Nb, $Ti_2(Ni,Cu)$	(135)

	diameter wires, cold-drawn into a 0.5mm diameter wire	for 20 min, air cooling